Microplastics analyzed by Femtosecond Stimulated Raman Microscopy (FSRM)

Inaugural thesis
presented to the Faculty of Mathematics and Natural Sciences
of Heinrich Heine University Düsseldorf
for the degree of
Doctor of Natural Sciences

by

Carolin Borbeck
from Dortmund

Düsseldorf, March 2026

From the institute of Physical Chemistry II
of Heinrich Heine University Düsseldorf

Printed by permission of the Faculty of Mathematics and Natural Sciences of
Heinrich Heine University Düsseldorf

Examiners:
1. Prof. Dr. Peter Gilch
2. Prof. Dr. Michael Schmitt

Date of the oral defence: 26.01.2026

Acknowledgments

I would like to begin this work by expressing my sincere thanks to the many people whose support has been invaluable throughout the preparation of this thesis.

First and foremost, I am grateful to my supervisor, **Prof. Dr. Peter Gilch**, for accepting my proposal of a research topic of my own interest without hesitation. His trust allowed me the freedom to explore a subject that truly inspired me. His constructive feedback and insightful discussions have helped me grow far beyond the valuable knowledge I gained, and his guidance has played a crucial role in my development.

I would also like to thank **Prof. Michael Schmitt** for kindly agreeing to co-review this thesis.

Special thanks go to everyone who is or was part of the team of the femtosecond spectroscopy group. The bachelor students I had the pleasure of supervising: **Julian Ringling**, **Lena Lüllmann**, and **Leonard Röhrken** helped immensely in the initial phase of starting a new project; **Lars Fuxen** always remained optimistic even in frustrating situations and somehow made fixing a broken amplifier feel like a shared adventure or at least a fun story; **Roman Bernst** immensely supported the measurement and evaluation of microfiber samples and, beyond that, the published publication on the topic. Thanks to my colleagues, **Veronika Mendorf, Bárbara Elza Nogueira de Faria, Michelle Rademacher, Theresa Ott, Mabobeh Morshedi, David Klaverkamp, Simon Zimmermann,** and **Matthias Jantz** for conversations about scientific topics and beyond, coffee breaks and time spent together after work. They have created an enjoyable and light atmosphere every day. Thank you to **Franziska Bergstein** for quick help with both large and small matters and, most of all, for always having an open ear. Thank you to **Jennifer Kremper** for many coffees shared. I owe particular thanks to **Francisco van Riel Neto**, who was not only my office colleague but also a travel buddy at conferences and an ally in taming the beast that is FSRM. His support has helped me push through even the most challenging times.

Last but certainly not least, my heartfelt thanks go out to everyone else in my life who has always supported me: to my **friends and family** who have shaped me into who I am and will always stand by me; especially to my mother, **Karin Borbeck**, who has believed in me and supported me every step of my way. I am most grateful to my husband, **Anil Deger**, for his love and wholehearted support of all of my decisions.

Publications & Active Participation in Conferences

Publications in Peer-Reviewed Journals

- Borbeck, C., van Riel Neto, F., Bernst, R., and Gilch, P., Microfiber analysis *via* femtosecond stimulated Raman microscopy (FSRM). In: *Microplastics & Nanoplastics* **5**, 14 (2025). DOI: 10.1186/s43591-025-00113-0
- van Riel Neto, F., Borbeck, C., Saatkamp, T., Kenny, M., Schmidt, S., and Gilch, P., Polymer, Water, and Salt Partitioning in Complex Coacervates Characterized by Femtosecond Stimulated Raman Microscopy. In: *Chemistry—Methods*, 2500005 (2025) DOI: 10.1002/cmtd.202500005

Conference Participation: Oral Presentations

- Analysis of Microplastics in Consumer Goods via Femtosecond Stimulated Raman Microscopy, XXVII International Conference on Raman Spectroscopy (ICORS), Long Beach, California, USA, August 2022.
- A Fast Broadband Approach to the Analysis of Microplastics: Femtosecond Stimulated Raman Microscopy, 9th International Conference on Advanced Applied Raman Spectroscopy (RamanFest2022), Paris, France, September 2022.
- Analysis of Microplastics with Femtosecond Stimulated Raman Microscopy – Merits and Pitfalls, Focus on Microscopy (FOM2023), Porto, Portugal, April 2023.
- Advancing Microfiber Analysis using Femtosecond Stimulated Raman Microscopy (FSRM), XXVIII International Conference on Raman Spectroscopy (ICORS), Rome, Italy, August 2024.

Abstract

Microplastics have emerged as a pressing global concern and have attracted attention in society, politics, and scientific research. Small synthetic particles are reported in a broad range of contexts, from the environment and animals to food and even human specimens. They have become ubiquitous and their effects on ecosystems and human health are hard to assess. Monitoring microplastics is an important aspect of mitigating their pathways into the environment and, eventually, uptake by humans. Existing techniques for the identification of microplastics often lack a reliable characterization of chemical characteristics and/or are time consuming.

This thesis introduces a novel approach to microplastic analytics: femtosecond stimulated Raman microscopy (FSRM). This fast and broadband method for the characterization of microplastic particles enables both qualitative chemical evaluation of a sample's components, as well as quantitative measures of the particles observed, i.e. their shape, size, and number. Acquisition times in FSRM are much faster than those for spontaneous Raman micro-spectroscopy, an established method in the research of microplastics. Furthermore, spectra in FSRM, which are similar to those achieved with conventional Raman techniques, are not distorted by fluorescence of the sample material potentially induced by the laser applied. FSRM further offers the same advantages as conventional Raman, such as high spatial resolution potentially down to 1 µm and being almost indifferent to water, both of which are drawbacks of another commonly applied technique, IR microscopy.

First, the comparability of FSRM Raman spectra with those acquired with a spontaneous Raman spectrometer is shown for selected solvents. All spectra were corrected for their dependence on the frequency of the exciting laser light. Spontaneous Raman spectra are more strongly affected than FSRM spectra, rendering this correction necessary, especially as lasers with different wavelengths are often applied in spontaneous Raman spectroscopy. The broadening of Raman lines due to experimental effects in FSRM were also accounted for. Experimental results of FSRM spectra were in line with the converted spectra for acetonitrile, benzonitrile, and toluene. Deviations were observed in the case of alcohols methanol, ethanol, and 2-propanol. Possible causes for the deviations will be discussed in this thesis.

A sample preparation mimicking environmental samples contaminated by microplastics was developed and first showcased for the example of commercially available standards: polymer beads of poly(methyl methacrylate) (PMMA) and polystyrene (PS). This approach was also employed to analyze primary microplastics found in consumer

products. FSRM measurements of two facial scrubs containing different microplastic components as abrasive ingredients will be shown here.

Finally, a focused analysis was conducted on a type of microplastics frequently found in the environment: microfibers. Common samples of both natural and synthetic fabrics were dissected into small microparticles and prepared for evaluation with FSRM with the same protocol developed to simulate aqueous environmental samples as first shown for primary microplastics. Different statistical methods for evaluation of the acquired data were compared: fuzzy c-means clustering and principal component analysis. The capability to distinguish natural and synthetic fibers, one key factor in microplastics identification, was further demonstrated by an everyday sample of a denim fabric, consisting of natural cotton fibers as well as synthetic polyester fibers.

Zusammenfassung

Mikroplastik-Partikel haben sich zu einem ernstzunehmenden globalen Problem entwickelt, welches große Aufmerksamkeit in Gesellschaft, Politik und wissenschaftlicher Forschung erfährt. Kleine synthetische Partikel werden in unterschiedlichsten Kontexten nachgewiesen, von der Umwelt über Tiere bis hin zu Lebensmitteln und sogar in menschlichen Proben. Sie sind allgegenwärtig, ihre Auswirkungen auf verschiedene Ökosysteme und die menschliche Gesundheit jedoch schwer einzuschätzen. Die Überwachung von Verunreinigungen durch Mikroplastik stellt einen wichtigen Aspekt dar, um ihre Eintragswege in die Umwelt und letztlich die Aufnahme durch den Menschen zu minimieren. Bestehende Techniken zur Identifizierung von Mikroplastik sind häufig fehleranfällig in der chemischen Charakterisierung der Partikel oder erfordern zeitaufwändige Messungen.

In dieser Dissertation wird ein neuartiger Ansatz für die Mikroplastik-Analytik vorgestellt: Femtosekunden-stimulierte Ramanmikroskopie (FSRM). Diese schnelle und breitbandige Methode zur Charakterisierung von Mikroplastikpartikeln ermöglicht sowohl eine qualitative chemische Bewertung der Bestandteile einer Probe als auch zeitgleiche quantitative Aussagen über Form, Größe und Anzahl der nachgewiesenen Partikel. Die Messzeiten mittels FSRM sind deutlich kürzer als bei der spontanen Raman-Mikrospektroskopie, einer etablierten Methode in der Mikroplastikforschung. Zudem sind die mittels FSRM gewonnenen Spektren, welche denen konventioneller Raman-Techniken ähneln, nicht durch Fluoreszenz der Proben gestört. FSRM bietet darüber hinaus dieselben Vorteile wie konventionelle Raman-Techniken, darunter eine hohe räumliche Auflösung bis zu 1 µm sowie eine weitgehende Unempfindlichkeit gegenüber Wasser. Letztere sind beides Nachteile der ebenfalls häufig verwendeten IR-Mikroskopie.

Zunächst wird in dieser Arbeit die Vergleichbarkeit von FSRM-Raman-Spektren mit denen eines spontanen Raman-Spektrometers anhand ausgewählter Lösemittel demonstriert. Alle aufgenommenen Spektren wurden hinsichtlich ihrer Abhängigkeit von der Frequenz des anregenden Lasers korrigiert. Spontane Raman-Spektren sind stärker abhängig von der anregenden Frequenz als FSRM-Spektren. Dies zeigt die Notwendigkeit einer Korrektur, insbesondere da in der spontanen Raman-Spektroskopie häufig verschiedene Wellenlängen eingesetzt werden. Darüber hinaus wurden experimentelle Einflüsse auf die Linienbreiten der Raman-Banden bei FSRM berücksichtigt. Die mittels FSRM gemessenen Spektren von Acetonitril, Benzonitril und Toluol stimmten mit den Erwartungen größtenteils überein. Für die alkoholischen Lösemittel Methanol, Ethanol und 2-Propanol wurden jedoch Abweichungen beobachtet, deren mögliche Ursachen in

dieser Arbeit diskutiert werden.

Ein Verfahren zur Probenvorbereitung, welches diejenige von Umweltproben mit Mikroplastikkontamination imitiert, wurde entwickelt und hier zunächst anhand kommerziell erhältlicher Standards vorgestellt: Polymerkugeln aus Polymethylmethacrylat (PMMA) und Polystyrol (PS). Diese Methode wurde anschließend zur Analyse primärer Mikroplastikpartikel in Konsumgütern eingesetzt. FSRM-Messungen zweier Gesichtspeelings, die unterschiedliche Mikroplastik-Komponenten enthalten, wurden durchgeführt und hier dargestellt.

Abschließend erfolgte eine gezielte Analyse eines häufig in der Umwelt vorkommenden Mikroplastiktyps: Mikrofasern. Beispiele häufig verwendeter Natur- und Synthetikstoffe wurden in kleine Mikropartikel zerteilt und gemäß des entwickelten Protokolls, welches wässrige Umweltproben simuliert, für die FSRM-Messung vorbereitet. Verschiedene statistische Verfahren zur Datenauswertung wurden angewandt und verglichen: fuzzy c-means clustering und Hauptkomponentenanalyse. Die Fähigkeit zur Unterscheidung zwischen natürlichen und synthetischen Fasern, welche ein entscheidender Aspekt in der Identifikation von Mikroplastik ist, wurde zusätzlich anhand eines Alltagsbeispiels demonstriert: eines Jeans-Stoffs, bestehend aus natürlichen Baumwollfasern sowie synthetischen Polyesterfasern.

Contents

1 Microplastics Analytics: An Urgent Matter

In 1907, Leo H. Baekeland patented a product he called Bakelite [1], the world's first fully synthetic plastic [2]. Plastics have since made positive impacts on our lives. For instance, they can reduce the energy consumption in transport when used for packaging, as they are more resistant and lightweight than other materials [3]. Plastics are cheap to produce and adjustable to almost all needs; therefore, they have become a part in most aspects of our lives, and their usage remains increasing [4]. Without global policy changes reducing plastics use, current reports estimate it to triple until the year 2060 compared to 2019 [5].

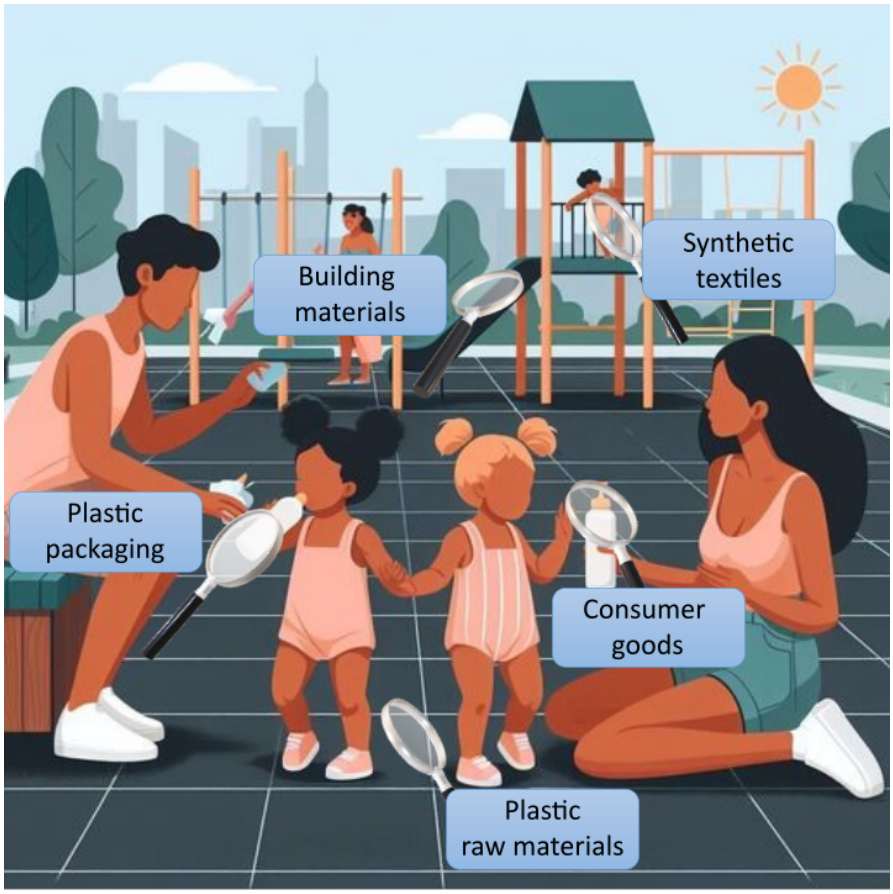

Figure 1.1: Examples for plastics use in daily lives. Plastic materials can be found in many products. These products can be for single use, e.g. as packaging materials, or long-term use, e.g. in construction, consumer products or textiles. (Playground image generated using Microsoft Designer Image Creator based on DALL-E 3 model).

Plastics are now ubiquitous in daily live, with some examples portrayed in Fig. 1.1. The major uses of plastics worldwide are packaging, which accounts for almost one third of plastics use, construction, transportation, consumer products, and textiles, each accounting for roughly 10 % of global plastics use [6]. Different polymers are

used depending on the requirements of the application. As visualized in Fig. 1.2, the polymer produced most is polyethylene, which can be differentiated in the main categories low density (LDPE), linear low-density (LLDPE), medium-density (MDPE), and high-density polyethylene (HDPE). LDPE is often used for food packaging or reusable films, whereas HDPE can be found in toys or shampoo bottles. Polypropylene (PP) is the polymer with the second highest production volume, used for example for food packaging and automotive parts [6, 7].

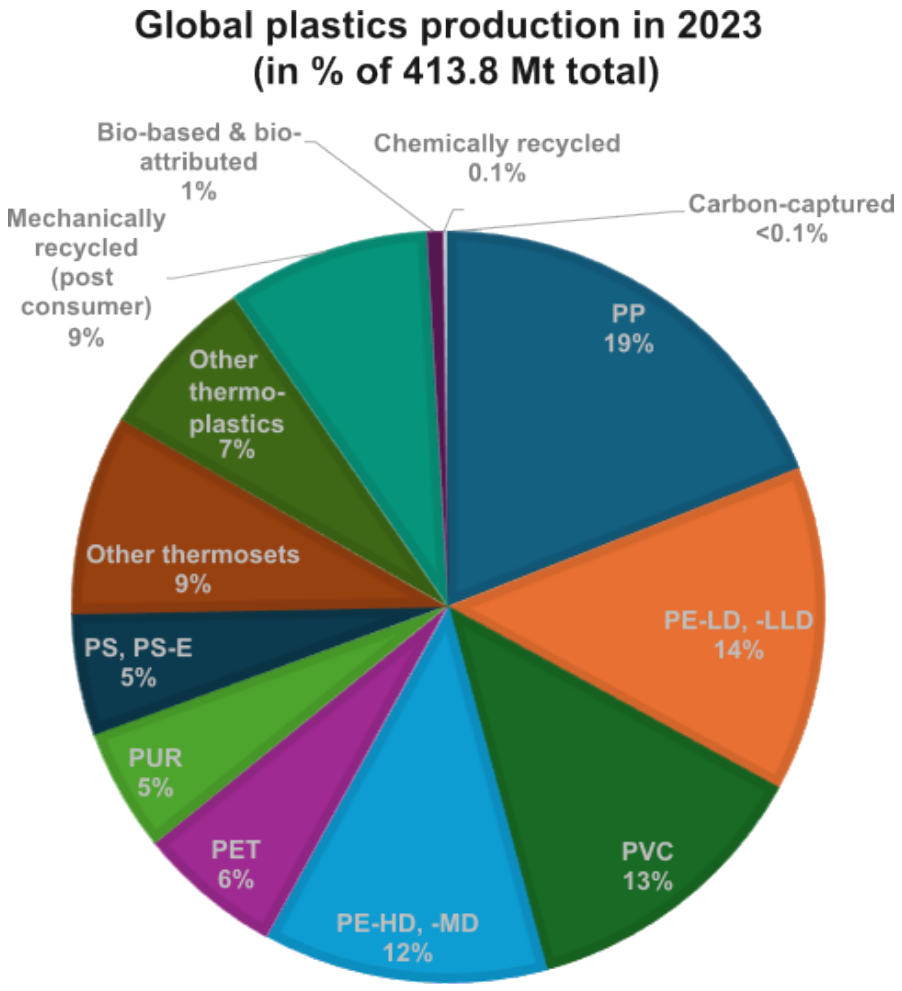

Figure 1.2: Global plastics production in 2023. Out of the total plastics production volume of roughly 414 million tons, polyethylene was the type of polymer produced most (108.4 million tons in total for LDPE, LLDPE, HDPE, and MD-PE, combined), followed by polypropylene (PP, 78.6 million tons). Other notable polymers are (in order of descending production volume): Polyvinyl chloride (PVC, 52.9 million tons), polyethylene terephthalate (PET, 25.7 million tons), polyurethane (PUR, 21.9 million tons), polystyrene (PS, 21.5 million tons), other thermosets, which include for example polyurethanes and resins made of acrylic, vinyl ester, or epoxy (35.6 million tons), other thermoplastics, which include for example polycarbonate or copolymers of styrene ABS (acrylonitrile butadiene styrene) (29.4 million tons). "Circular" plastics, i.e. recycled or bio-based plastics or those with raw materials based on carbon capture, accounted for 9.6% (39.7 million tons) of total production volumes. Based on data as published by Plastics Europe [7].

Nowadays, plastics face criticism due to their harmful impacts on the environment and partially unknown effects on human health [8]. Especially small plastic particles have gained a lot of attention. Earliest reports of such particles in the environment are from 1972 [9], but they were first termed microplastic (MP) in 2004 by Thompson *et al.* [10, 11]. Since then, they have been documented in almost all environmental settings [10, 12–15]. Evidence of transfer along the food chain exists, for example, MP particles were documented in drinks and foodstuff [16–18] as well as in human specimen [19–24]. The effects of MP exposure currently remain partially unknown. They have been found to affect health but the results are inconclusive to this point, as such studies often feature much higher concentrations of particles than found in environmental samples [25]. More detailed definitions of MP, as well as their distribution and effects on ecosystems and human health will be discussed in Chapter 2.

Due to these concerns, the European Union has committed itself to fight MP pollution and recently adopted the EU Action Plan: "Towards Zero Pollution for Air, Water and Soil" [26]. As a part of this plan, Commission Regulation (EU) 2023/2055 became effective in October 2023 [27], which restricts the use of MP intentionally added to consumer products. During this PhD, it became apparent that many producers of consumer goods had already started to adhere to the regulation before it became effective and stopped using synthetic particles in their commercially available products. New samples for evaluation of primary MP in consumer products could not be acquired, leading to a shift in the type of MP to be evaluated in this thesis from primary MP to microfibers. It is not known whether this was an early implementation of the EU regulation or driven by consumers' demand of products free of MP.

For monitoring the distribution of MP, correct quantification and characterization of particles found in a sample are important. Current methods mostly include a visual identification step, which is only possible for larger particles with a size >1 mm and prone to high error rates [28]. Vibrational (micro-)spectroscopy offers the possibility to characterize the chemical composition of particles. IR and Raman have become commonly applied methods, both offering respective advantages and disadvantages in the application of MP analytics [29]. The current state of MP analytics will be further discussed in Section 3.1, as well as challenges the methods currently available face. Depending on the method applied and the sample preparation protocol, results may vary, highlighting a need for standardization of sample preparation and measurement protocols [30].

For the above reasons and due to personal passion for this field of great scientific and societal interest, it was chosen as the objective of this thesis. This thesis aims to introduce femtosecond stimulated Raman microscopy (FSRM), a fast and broadband

technique for vibrational micro-spectroscopy [31], as a novel method for MP analysis, including development of sample preparation and measurement protocols for this technique to improve the current state of the art in the field.

2 Introduction to the Microplastics Problem

2.1 Definition and Types of Microplastics

MPs are small, solid plastic particles which are not soluble in water and are most commonly defined to be in a size range between 1 µm and 5 mm. Particles between 1 and 5 mm are referred to as large MPs [32]. Two main classes of MP origins can be distinguished: Primary and secondary MP, as summarized with some exemplary sources in Fig. 2.1. Primary MPs are produced intentionally and added to end-user products, e.g. cosmetics. Secondary MPs develop due to degradation of larger pieces of plastic [32], e.g. by abrasion of material, damage due to exposure to sun, or microbial action [25]. MPs are usually observed in the shape of microbeads, nurdles, fibers, fragments, or foams [33, 34].

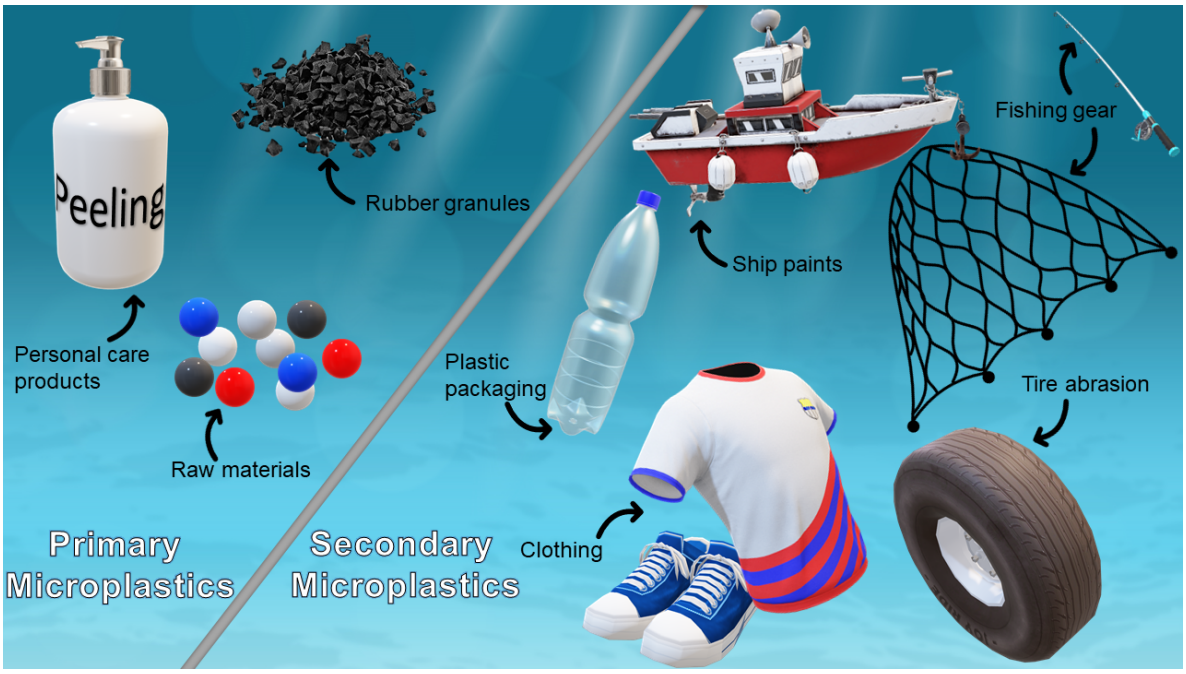

Figure 2.1: Examples for types and main sources of microplastics in the (aquatic) environment.

Examples for primary MP are plastic pellets, used for examples to build running tracks or playground flooring (cf. Fig. 1.1), cosmetics containing plastic glitter particles, personal care products like facial scrubs containing microbeads, which often display a spherical shape. Secondary MP accounts for the highest share of MP found in the environment, mostly caused by anthropogenic litter like plastic bags, bottles, and packaging materials. Fishing waste also significantly contributes to MP pollution [35], as well as paints and coatings, for example from ships [36]. Tire wear is often stated as the main

source of MP pollution due to the large amount of vehicles globally, although not many studies support a proportionately large presence of rubber particles in environmental settings [35]. In marine and freshwater samples, MP particles are primarily reported in the shape of fibers [33, 34], of which a main source is laundry of synthetic textiles [37]. These microfibers found in the environment will be further highlighted in Section 2.2.1.

The composition of MP particles varies depending on the sampling location. For example, concentrations were observed to be higher in sediments than in surface waters and the compositions differed as well [38]. Each plastic has a unique density, which influences its behavior and transport pathways in the environment. For example, lower-density MP particles are expected to be transported further when disposed in a river than higher-density particles [39]. A review of 42 studies on marine environments found that the most frequently identified polymer was polyethylene (PE), reported in 33 studies, followed by polypropylene (PP) in 27 studies, and polystyrene (PS) in 17 studies. The relatively low densities of these polymers enable them to float in both freshwater and seawater, which likely explains their frequent detection, as sampling is typically limited to certain water depths [28]. Polyamide, more commonly known as nylon, and polyester — both commonly used in textiles [40] — were the next most frequently reported polymers. These were followed by acrylic, polyoxymethylene, polyvinyl alcohol, polyvinyl chloride, polymethyl methacrylate, polyethylene terephthalate, alkyd, and polyurethane [28].

2.2 Environmental Distribution

MP has become ubiquitous and can be found in almost all environments. Most studies focus on MP in water, with a special emphasis placed on ocean water in the past [41]. Of the approximately 250 000 tons of plastics modeled to float in the oceans in a 2014 study, 35 500 tons are estimated to be particles below 5 mm [42]. Earliest reports of MP on the sea surface are from 1972 [9]. They were also found along shorelines around the world [10, 12, 34]. In 2013, MP was first reported in a lake, namely Lake Garda [43], and found in all lakes examined later [44]. A main route of plastics into larger bodies of water are rivers [45]. One of the first extensive studies on the distribution of microplastics in a river was conducted by Mani *et al.* in 2015 [46], focusing on the Rhine. This study held particular relevance to this thesis, as the thesis was conducted in Düsseldorf, a city situated along the Rhine's course. MP was found in all sampling locations along the Rhine, with a peak concentration in the Rhine-Ruhr metropolitan area [46], one of the largest urban areas in Europe. Population density has a direct impact on MP concentrations, as plastics are a significant form of anthropogenic waste. Wastewater

treatment plants (WWTPs) are capable of filtering out only a limited quantity and size of particles, including microplastics introduced into the water by human activity, which is often reported to result in the release of MPs into rivers [34]. Some reports, on the other hand, suggest that the impact of WWTPs on MP release into rivers is debatable [47], pointing to the need of further research. Sewage sludge of WWTPS, which displays a high concentration of MP, is often used as fertilizer for agricultural soil [48]. Inadequate waste management contributes to the further release of MPs into the environment [34], for example by consumer packaging discarded directly into or near water [47].

The oceans were recently found to not only be a sink for MP but can also act as a source. MP in the water can be re-emitted to air by small water droplets, resulting in presence of MP in the marine atmosphere [15]. Further reports of air transport of MP particles exist [49], for example particles were detected in remote mountain regions of the French Pyrenees [13]. Atmospheric deposition also causes MP contamination in protected national parks in the US [50]. The air in urban areas is, of course, also affected. For instance, all atmospheric samples collected in the metropolitan area of Hamburg were found to contain MP [51].

The research on MP contamination has so far primarily focused on aquatic ecosystems, with studies on terrestrial environments emerging more recently, particularly from China and Europe [52, 53]. For instance, particles have been detected in potting soil and in roadside ground in Cologne [54]. The first documented occurrence of MPs in agricultural soil was in 2005, where synthetic fibers indicated sewage sludge application, a common fertilization method [48]. From these fields, particles may be taken up by crops, as MPs have been detected in fruits and vegetables [55].

MP transport through the food chain has been reported in several additional ways [18]. Early findings revealed contamination in German beers [16], followed by bottled drinking water [17], raising concerns about regular human ingestion. MPs have also been found in condiments such as sugar [56] and salt [57]. Contamination levels varied based on the salt's origin, with sea salt showing the highest concentrations. These findings reinforce that MP accumulation in the environment transfers up the food chain. In this context, seafood has been studied most extensively [18], with reports of MPs found in mussels [58], fish [59], and shrimp [60], for example.

2.2.1 Microfibers in the Environment

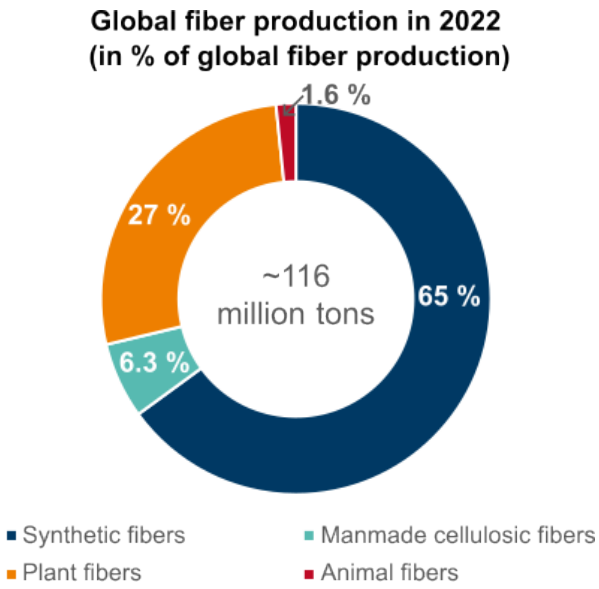

Figure 2.2: Global fiber production in 2022 in approximate % of global fiber production. The total fiber production was 116 million tonnes. For the three categories, the fibers with the highest share of total fiber production were the following: Synthetic fibers: polyester (54%), polyamide (5%), polypropylene (2.7%). Plant fibers: cotton (22%), other plant fibers (5.2%), flax (0.32%). Manmade cellulosic fibers: viscose (5%), acetate (0.82%), lyocell (0.28%). Animal fibers: wool (1%) (based on Ref. [40])

Among the numerous microplastics detected in the environment, fibers are the most commonly reported shape [34, 37]. Washing machine effluent is a major source for the release of microfibers into the environment, with possibly over 100 fibers per liter released from a single garment [12]. These fibers can only partially be removed from the sewage before their release into aquatic ecosystems [12]. The sewage sludge is especially enriched with fibers [48] and, as mentioned above, it is often brought on agricultural soils for fertilization. Globally, approximately 65 % of fabrics produced are of synthetic origin [40], as shown in Fig. 2.2. Polyester has the largest share (54 % overall), followed by cotton, polyamide, and viscose, a manmade cellulosic fiber [40]. Consequently, it is expected that most fiber particles reported in ecosystems are of synthetic origin, hence classifying them as MP. As an example, fibers account for the largest number of particles identified in food and drinks [61]. Recent studies, however, suggest that the proportion of fibers characterized as MP has been largely overestimated [62, 63]. More conflicting results further complicate the picture: synthetic particles were detected in beer [16] and drinking water [17], yet a focused analysis of fibers in beverages found no synthetic particles present, only cellulose fibers [64]. Additionally, blank samples showed similar particle counts as actual samples, highlighting not only the omnipresence of microfibers but also the importance of protocols for sample preparation and adequate qualitative analysis.

2.3 Potential Impacts on Ecosystems and Health

Microplastic particles which have been deposited into the environment are bioavailable to wildlife, i.e. they can be ingested in different ways, for example by being swallowed directly or indirectly, inhaled or absorbed through the skin [65]. In the example of ingestion by eating, bigger pieces of plastic debris or their small degradation products can be mistaken for food and are consumed directly. There have been reports of MP in filter feeders of various sizes, such as bivalves (mussels) [58], planktivorous fish [66], and humpback whales [67], all of which gather food particles from water by filtration. Additionally, evidence of a trophic transfer exist, meaning that the (micro-)plastics move up to higher trophic levels of the food chain [11, 65]. For example, plastic particles were found present in the guts of seabirds [68], with the perceived intake increasing over time [65]. Such an ingestion of MP poses several risks to organisms. First of all, particles can cause direct physical harm, for example due to abrasion, blockages in the gastrointestinal tract or reduced feeding caused by the non-digestible particles [11]. Another risk of MP ingestion is exposure to toxic chemicals that were added to the material upon production or adsorbed to the particles' surface from the environment [11]. Examples of such chemicals reported in or on marine plastic fragments include polychlorinated biphenyls (PCBs), polycyclic aromatic hydrocarbons (PAHs), and bisphenol A (BPA), which are endocrine disruptors and can cause long-term harm [65]. These persistent organic pollutants (POPs) are often non-polar and therefore easily adsorbed to hydrophobic MP surfaces [69]. To highlight one of these harmful POPs, the use of BPA and its salts in materials which come into contact with food, such as packaging, has recently been prohibited in the European Union due to its health risks [70]. These leached additives can have different impacts on ecosystems. There is also a risk of additives in MP leaking into the aquatic ecosystems, for example tire wear particles have been shown to introduce transformation products of quinone to creeks in the United States, likely linked to an acute increase in mortality rates of salmon [71]. A recent meta-analysis concluded that exposure of fish to MPs inhibits their growth, survival, and reproductive capabilities, with the exposure to MP in water causing more damage than through food [72].

Harmful heavy metal ions have also been found to adsorb to the surface of MPs, for example cadmium, nickel, or lead [69]. The smaller the particles are, the larger their area relative to their mass and, in turn, the potential amount of adsorbed pollutants [11]. Proteins can also be adsorbed to the surface of MP particles. This results in a unique pattern called a bio-corona. Such a bio-corona can change the physicochemical properties of the particle, which in turn influences the interactions with organisms, for

example resulting in a larger bio-availability and therefore easier uptake. The bio-corona can also further enhance the adsorption of other pollutants [69, 73].

As mentioned above, MP can be transported up the food chain and eventually be consumed by humans. Furthermore, humans can directly ingest or inhale MP, as it is ubiquitous (cf. Section 2.2). As a consequence, MP has been frequently reported in human specimens, for example in blood [22], placenta [20, 23], meconium [23], breast milk [24], lung tissue [19, 21], cirrhotic liver tissue [74], and kidney tissue [75]. These are indicators that MPs can traverse the body easily [11].

The effects of short- and long-term exposure of MP in humans cannot easily be assessed. Particles present in placenta can potentially affect the growth of the unborn child [20]. Some further conclusion can be drawn from assessments of the effects on other mammals. For example, behavioral differences and increased inflammation were observed in mice after exposure to MP [76]. It was shown in mice that nanoparticles can traverse the barrier between blood and brain and can potentially accumulate, causing blockages [77]. Besides potential direct effects on the blood stream, the accumulation of MP in the human body can lead to regions of localized toxicity, ultimately affecting the immune response [69]. Furthermore, the indirect effects of MP due to additives or adsorbed chemicals are potentially harmful for humans, as they are for marine life.

However, most reports on effects of MP in biota have employed higher MP particle concentrations than have been recorded in the respective relevant environment. Furthermore, sometimes opposing results show no actual negative effects, which emphasizes the importance of further studies on the effects of exposure to environmentally realistic MP concentrations [73].

3 Techniques for Microplastics Analysis

3.1 Current State and Challenges of Microplastics Analytics

MPs occurring in the environment display many different characteristics which need to be considered during their evaluation. Some examples are differing sizes, shapes, and chemical compositions of samples. The latter are not only affected by the type of polymer and its production and/or additives but also by the weathering of a particle and potentially adsorbed chemicals in the environment. Depending on the routes the particles have traversed to the sampling site, they display different states of aging and abrasion. Consequently, adequate reference materials and spectral databases of particles resembling those found in environmental samples are lacking [73]. Differences in the particles to be characterized are not the only challenge in analytics of MP. The level of MP pollution varies depending on the medium from which the sample is extracted (e.g., water, soil, biological specimens), influencing the amount of sample needed. Each medium to be investigated also requires specific cleaning and extraction protocols. Furthermore, different methods are typically employed for characterization and quantification of MP contamination. This often results in either choosing between a qualitative or a quantitative approach, or a combination of chemical identification with mass- or particle-based methods is required [73].

The ubiquity of MP has proven to be another challenge in the whole analytical process. During the sampling process, handling, and analysis, environmental MP can contaminate the samples [36, 64]. For example, as most fabrics produced globally are of synthetic origin [40], microfibers can easily be transferred from clothing of people handling the samples. Blank samples for the whole procedure are necessary to confirm results and avoid misinterpretations [64, 73]. However, no standardized methods for analysis, quality assurance, and quality control currently exist [73], rendering a comparison of studies challenging. It is therefore important to develop standardized protocols for sample preparation [30].

Contamination of samples can be minimized in several ways, for example by working in a laminar flow box or clean room and performing all steps of sample handling in an environment low or devoid of plastic. In addition to optimizing workflows by minimizing sample loss as well as contamination, analytical methods should be compared between laboratories to ensure adequate quality of the respective methods [73].

Several methods for microplastics analysis have become established, focusing on different aspects of the contamination. Some of these are summarized in Fig. 3.1. Methods can include either a purely quantitative approach, i.e. counting the number

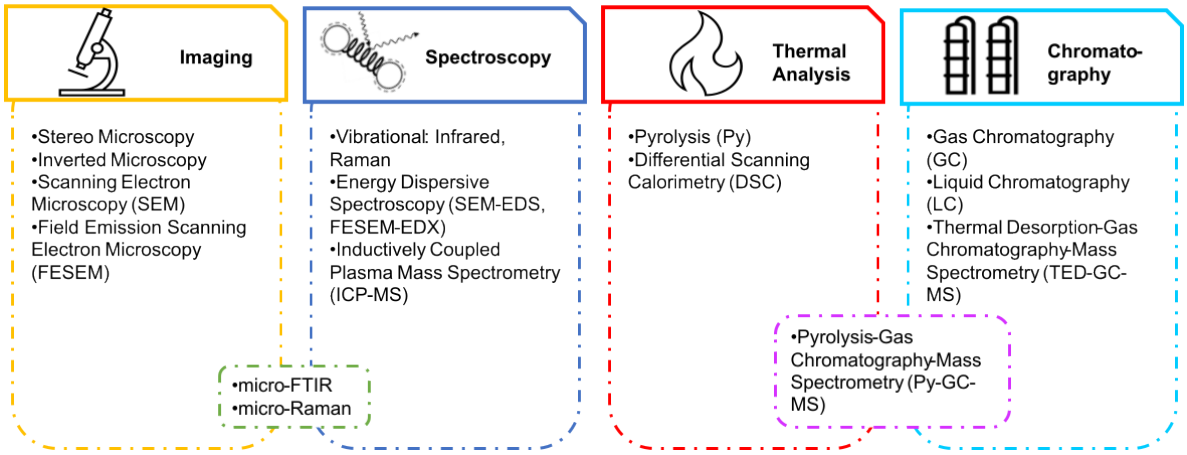

Figure 3.1: Summary of common MP analysis methods [25, 73].

or mass of particles observed, purely qualitative approach identifying only the types of polymers present or combinations thereof [73, 78]. Visual identification and imaging are commonly used methods [78] for quantifying or pre-sorting particles. More qualitative techniques determine the chemical composition of samples. Thermal degradation, most often pyrolysis (Py), coupled with chromatographical and/or spectrometrical approaches, usually gas chromatography-mass spectrometry (GC/MS) offers a simultaneous identification and quantification of particles [73]. Py was first demonstrated in MP analytics for the identification of tire abrasion in roadway dust already in 1966 [79] and the combination of Py-GC/MS was shown to identify anthropogenic compounds in soil [80]. Although the combination of these techniques is already established and yields a lot of information about MP contamination, it suffers the drawbacks that, for example, polymers cannot be distinguished from co-polymers if they both exist in the sample and information like particles' sizes, shapes, and numbers cannot be distinguished [73]. Further examples of methods based on mass spectrometry which have been applied in the analytics of MP are MALDI-ToF (matrix-assisted laser desorption/ionization time-of-flight mass spectrometry) coupled with MS [81] and inductively coupled plasma mass spectrometry (ICP-MS).

The above qualitative methods have in common that they are all destructive, rendering a further analysis of particles at a later point impossible. Vibrational spectroscopy is a non-destructive approach focusing on separate particles [73] and will be further discussed in Section 3.3. Further non-destructive imaging techniques like scanning electron microscopy (SEM) [82] have also been applied, potentially coupled with energy dispersive X-ray spectroscopy (EDX) [25, 83].

3.2 Visual Identification and Conventional Light Microscopy

Visual identification of particles is a commonly used method. Sometimes sorting happens by eye, more commonly, light microscopes or dissecting microscopes are used [78, 84]. A review of studies on environmental MP published until 2018 showed that in 79% of studies, visual identification was employed in some form [78]. Approximately half of the studies used it to pre-sort samples for further analysis. The other half stated a visual identification as their only method for MP characterization [78]. It is often a necessary step to sort out organic debris and is a valid method as it is fast, cheap, and relatively accurate for larger MPs down to a size of around 500 µm to 1 mm [28, 78]. Only few of the reviewed studies mention whether measures were taken to minimize researcher bias [78], which can be highly problematic as researchers often overestimate the number of particles that are actually synthetic, especially for small particles. Colored particles are more likely to be characterized correctly, highlighting the difficulty to assign environmental particles [85]. To minimize the bias, microscopical MP identification is often enhanced by staining samples, e.g. with a fluorescent dye. Nile red is the one used most commonly [84]. The combination of microscopical techniques with spectroscopical ones is also an important method to add a chemical analysis to usually purely quantitative visual methods and will now be discussed in more detail.

3.3 (Micro-)Spectroscopical Techniques

Spectroscopic techniques give insight into the chemical composition of samples and therefore enable a characterization of both synthetic (i.e. plastic) and natural particles. This makes MP distinguishable from particles that occur naturally, minimizing researcher bias and adding a qualitative character to the quantitative methods described before. Both (Fourier transform (FT)) infrared (IR) and Raman spectroscopy find broad applications in MP analysis [73]. They are label- and destruction-free, unlike fluorescence staining and thermal degradation, for example. Furthermore, they can be combined with microscopical techniques to simultaneously obtain information on the chemical composition and the size, shape, and number of the particles present. The application of the techniques will be explained in the following sections.

The acquisition of spectroscopic data should be followed by the crucial step of matching the obtained spectra with reference databases. Accurate particle identification can only be achieved by an adequate comparison, for which the Hit Quality Index (HQI) is a key metric. Higher HQI values indicate closer matches between a measured spectrum and a reference spectrum. HQI calculation typically employs instance-based machine

learning methods, such as Euclidean distance or Pearson correlation, although the precise HQI values can vary based on the algorithm or software used [73, 86]. Consequently, to ensure reliable MP identification, databases need to be carefully constructed. They must include not only spectra of pristine polymers but also realistic, weathered MP particles and relevant environmental materials, like cellulose, quartz, or wood, to minimize misidentification. Databases which can be flexibly modified and expanded as new data emerges, to accommodate additional spectra from different sources, materials, or environmental conditions, can help improve HQI precision across diverse conditions and enhance the overall reliability of spectroscopic techniques for MP characterization [73, 84].

3.3.1 Infrared Spectroscopy

IR (micro-)spectroscopy is a widely applied method to determine chemical compositions of MP samples [78], with examples for most environments existing [73]. It is based on molecular vibrations induced by the absorption of radiation in the infrared, usually the mid-IR (400 - 4000 cm^{-1}) [73]. Weathered particles can be identified via FTIR, as the changes in the surface of pristine polymers caused by aging can be observed in the spectra [73]. However, due to the inherent diffraction limit of radiation in the IR, ranging between 1.7 µm and 11 µm depending on the wavelength, particles smaller than 20 µm remain challenging to characterize [87]. Attenuated total reflection (ATR) is a commonly applied method for MP analysis [84], which enables operation close to the diffraction limit [88]. However, ATR is a destructive method, as it involves contact between the sample's surface and a crystal, resulting in sample damage and even possible cross-contamination [84]. However,the main limitation of IR microscopy in MP analysis is the strong IR cross section of water [89]. The strong and broad bands superimpose on many typical vibrational bands of polymers. Therefore, samples must be thoroughly dried to allow analysis [73].

3.3.2 Spontaneous Raman Scattering

Raman scattering (micro-)spectroscopy, albeit used less frequently for MP analysis compared to IR techniques, has also become widely applied in the field [78]. Its principle will be outlined in Section 4.1. Compared to IR absorption, Raman scattering offers several advantages. For one, a better spatial resolution can be achieved because the applied wavelengths are shorter, resulting in a lower diffraction limit. Thus, smaller particles in the µm range can be characterized [29]. By combining spontaneous Raman scattering spectroscopy, which typically employs incident light in the visible range, with confocal

optical microscopy, a lateral resolution of around 1 µm or lower is achievable, as opposed to around 10 µm for IR microscopy [73]. Another advantage of Raman over IR is that it is less sensitive to water, as water is a weak Raman scatterer [90]. Thus, samples do not necessarily need to be dried, reducing the number of steps for the preparation of samples and, consequently, the potential loss of particles. However, spontaneous Raman microscopy also has several disadvantages. Laser induced fluorescence [29, 85, 91], especially prominent in environmental samples, can distort spectra. The fluorescence is caused for example by pigments added to the polymer [85, 89] or by biological residue in samples [89, 92]. The MP particles therefore need to be carefully separated from the surrounding sample matrix to remove any disturbing residues [73]. The fluorescence background can further be reduced by choosing longer-wavelength lasers for excitation, for example at 785 nm instead of the most typical excitation wavelength of 532 nm. However, higher wavelength excitation requires higher total laser powers. This might result in destruction of sample particles but also organic residues, which will produce degradation products that superimpose the Raman spectra of plastic particles. Furthermore, relative Raman signals within one spectrum depend on the excitation wavelength. Therefore, Raman spectra recorded at different excitation wavelengths often cannot be directly compared to each other [73]. A correction of the spectra is possible, which will be described in more detail in Section 4.2.3.

The most important drawback of Raman microscopy are the low cross-sections for Raman scattering [93], resulting in long acquisition times. Typical reported acquisition times are 1 s per pixel [89]. For full imaging techniques in which spectra are acquired for each spatial pixel, measurements of up to 38 hours have been reported [29]. Here, a spectral range of 160 – 3600 cm^{-1} was recorded with an integration time of 500 ms per scan and twenty averages per spectrum, and a 10 µm step size on a sample area of 1000 x 1000 µm, which equals 10 000 total spectra. Due to these long acquisition times, only parts of the sample, typically placed on a filter, can be scanned. This results in the loss of information. For example, Li *et al.* have performed a step-by-step scan of an approximately 1.5 mm^2 area of a filter with a total are of 227 mm^2 [73, 94]. This corresponds to only 0.667% of the filter surface. It is thus questionable whether the result is statistically correct and further sample regions should be evaluated for that sake.

Another technique commonly applied in spontaneous Raman microscopy, aimed at reducing long acquisition times, involves manual selection [29, 78]. Here, the sample can be pre-scanned and several points of interest distinguished for a full spectral evaluation. Commercial software is available and has already been applied to automate this process [95]. However, this methods risks that some particles are missed because they were not

distinguished as points of interest in the pre-evaluation. Furthermore, particles which are positioned close to each other might be mistaken for one particle and, thus, be identified incorrectly.

3.3.3 Non-linear Raman Approaches

Non-linear spectroscopy techniques aim to increase sensitivity and, consequently, increase speed of microscopical measurements. The most popular non-linear approaches applied in Raman microscopy are coherent anti-Stokes Raman scattering (CARS) [96, 97] and stimulated Raman scattering (SRS) [31, 98, 99]. These methods both employ multiple photons which induce Raman scattering by generating a coherent signal upon interaction with a sample. Both methods are unaffected or only slightly affected by disturbing fluorescence, as the Raman probe detected is typically more intense than the fluorescence. Furthermore, fluorescence mostly does not occur at the detected wavenumbers.

CARS is a third-order non-linear process for which three laser fields are applied which resonantly enhance anti-Stokes scattering in a medium [100]. As CARS was not applied in this thesis, only its applications for MP analytics will be discussed here. The first reported application of CARS for MP analysis was a study on the ingestion of PS beads by zooplankton in 2013 [101]. Another example of evaluating uptake of MPs and effects of the studied PS spheres on the marine life using CARS microscopy are shore crabs [102, 103]. Broadband, multi-color CARS approaches have been demonstrated for example to distinguish uptake of PS beads in live cells [104]. CARS does not usually suffer of fluorescence background and, especially at high concentrations of a medium, the CARS signal is strong, as the signal scales quadratic with the concentration, whereas spontaneous Raman signals scale linearly with concentration. However, CARS also suffers from major disadvantages, the main one being a non-resonant background observed in spectra, which is mixed with the signal, thus limiting sensitivity. Furthermore, due to the aforementioned quadratic scaling of the signal with concentration, low concentrations of molecules are not easily detected [100].

SRS, which is also a third-order non-linear process, employs two laser beams to stimulate Raman scattering. The principle of SRS is explained in more detail in Section 4.2.1. Unlike CARS, SRS signals scale linearly with concentration and mostly do not exhibit a non-linear background [99]. SRS-based approaches have been demonstrated in proof-of-principle studies for fast monitoring of MP contamination [105, 106]. However, SRS microscopy has not been frequently applied for MP contamination of environmental samples until now. A first proof-of-principle was published in 2018 by Zada *et al.* [107]

and it has later been applied to analyze microfibers found in environmental samples [63, 108]. The first method employed by Zada *et al.* is based on recording several maps for one pre-selected wavenumber each, while scanning every spatial pixel of the sample for the selected wavenumber. Usually, a sample was evaluated for 6 relevant Raman shifts, including one in the silent region to correct for artifacts [107]. Another approach, as applied by Laptenok *et al.*, performs a pre-scan of the sample's area of interest at a selected wavenumber with a full spectrum recorded for one position selected according to the pre-scan [108]. Thus, for the most common implementation of SRS including two narrow-band laser beams, the methods compromise either in terms of spectral coverage (i.e. only measuring certain wavelengths) or in terms of spatial coverage (i.e. only recording full Raman spectra in a few selected points).

4 Femtosecond Stimulated Raman Microscopy

4.1 Raman Scattering: An Overview

When a photon interacts with a transparent sample (gas, liquid, or solid), it is typically transmitted without changes to its direction or energy. However, some scattering will be observed, with components scattered either elastically (i.e., without a change in frequency) or inelastically (i.e., the scattered photon's frequency differs from that of the incident photon), as schematically shown in Fig. 4.1. One type of inelastic scattering that can be observed is Raman scattering, where the scattered photon has a lower (Stokes Raman scattering) or higher frequency (anti-Stokes Raman scattering) than that of the incident photon. At ambient conditions, Stokes Raman scattering is much stronger than anti-Stokes Raman scattering. The effect was first described by Smekal in 1923 [109] and later confirmed by Raman and Krishnan in 1928 [110], hence the name "Raman scattering". A Raman spectrum is a plot of the number of scattered photons as a function of the Raman shift $\tilde{\nu}$ [cm^{-1}].

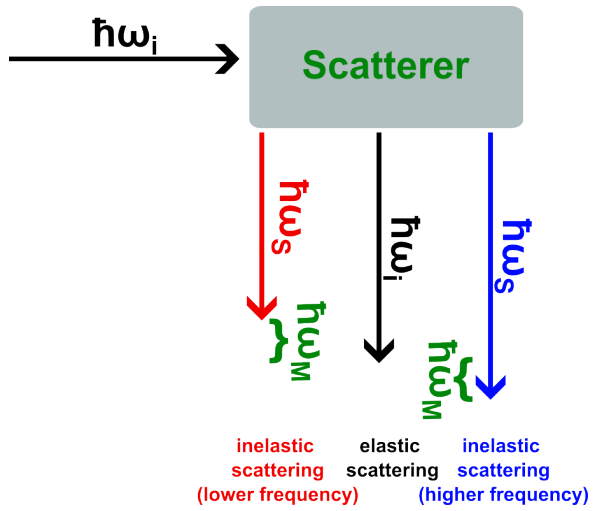

Figure 4.1: Scheme of spontaneous scattering processes. The length of the arrows represents the energy $\hbar\omega$ of the photons involved in the processes. In the case of elastic light scattering, the incident (rightward arrow) and scattered photons (downward arrows) have the same energy (middle). For Raman scattering, i.e. the inelastic processes, the scattered photon's energy changes. It can either have a lower (red arrow, left) or higher (blue arrow, right) energy than the incident photon. The case of lower frequency is called Stokes scattering, the case of higher frequency anti-Stokes scattering. The energy difference between the incident and scattered light is the observed Raman shift.

Several theories describe Raman scattering [111]. Here, the focus will be on the quantum mechanical approach. For the sake of simplicity, we assume monochromatic incident light consisting of a given number of photons with energy $\hbar\omega_i$. When this incident light interacts with a molecule of initial energy E_i, it can be scattered in different ways. Most likely, it will be elastically scattered, meaning that no change in energy is observed. This type of scattering is termed Rayleigh scattering. The light can also be scattered with an observed shift in its energy. This shift in energy is caused by an interaction of the incident light with the molecule. Before the interaction, the

molecule is in its vibrational ground state, where molecular bonds exhibit zero-point vibrations. These vibrations modulate the molecular polarizability. Interaction of the incident light with this time-dependent polarizability results in excitation to a virtual energy level. During this process, energy is transferred between the photons and the molecule. Stokes Raman scattering is the most likely scattering to be observed, with the annihilation of one photon of energy $\hbar\omega_i$ and creation of a new photon of lower energy $\hbar\omega_\mathrm{s}$. The molecule then transitions to a state with energy E_f. The energy difference between the incident and scattered photon corresponds to the perceived Raman shift $\hbar\omega_\mathrm{M}$ [111], which gives insight into the vibrational modes of a molecule. The energies observed in this process called Stokes scattering can be described by eq. 4.1

$$\hbar\omega_\mathrm{S} = \hbar\omega_i - \hbar\omega_\mathrm{M}. \tag{4.1}$$

Scattered light may also contain photons of higher energy than the incident light, which is termed anti-Stokes scattering and described as

$$\hbar\omega_\mathrm{AS} = \hbar\omega_i + \hbar\omega_\mathrm{M}. \tag{4.2}$$

Anti-Stokes Raman scattering is less likely because it involves molecules which are in an excited vibrational state before interaction with the photon. The vibration then relaxes back to the lower-energy ground state, which results in a higher frequency of the scattered light compared to the incident one. Under ambient conditions, the majority of molecules will be in the ground state, therefore anti-Stokes Raman scattering is highly unlikely. However, with increasing temperature, excited states are more likely to be populated, therefore anti-Stokes Raman scattering will become more likely.

The process of spontaneous Raman scattering is inherently weak, resulting in commonly low signal levels. The strength of the interaction between light and a molecule is usually described in terms of the (scattering) cross section σ. For IR absorption in common compounds, σ lies in the range of 10^{-19} to 10^{-17} cm^2 [93], for UV-Vis absorption they are higher, ranging from 10^{-16} to 10^{-15} cm^2 [93]. Raman scattering cross sections are around ten orders of magnitude smaller than comparable IR scattering cross sections, as they range between 10^{-30} to 10^{-26} cm^2 [93]. Resonance Raman scattering cross sections can reach up to 10^{-23} cm^2[93]. Acquiring Raman spectra therefore requires long measurement times due to the need to average many spectra for an adequate signal-to-noise ratio (SNR). This especially influences the time a microscopical measurement requires, as many spectra need to be recorded. Various techniques aim at enhancing the signal. For example, samples can be adsorbed to a surface in a spectroscopy technique labeled

SERS (surface enhanced Raman spectroscopy) [112, 113] or a variation of it labeled TERS (tip-enhance Raman spectroscopy), which combines Raman spectroscopy with atomic force microscopy [114–116]. Approaches which are inherently label-free include non-linear techniques like CARS (coherent anti-Stokes Raman spectroscopy) and SRS (stimulated Raman spectroscopy), which require the use of at least two laser sources to induce Raman scattering. SRS is the basis of the technique applied here and will be detailed in Section 4.2.1. As CARS is not applied in this thesis, its principles will not be further discussed.

4.2 Principles and Fundamentals of FSRM

4.2.1 Femtosecond Stimulated Raman Scattering

Stimulated Raman scattering, a process first described in 1962 by Eckhardt *et al.* [117], is a non-linear Raman scattering process and the basis of the method employed in this thesis, femtosecond stimulated Raman spectroscopy (FSRS). The stimulated Raman effect is much stronger than the spontaneous one [93], which decreases the time needed to acquire spectra with a sufficiently high SNR. To stimulate Raman scattering, radiation of two different frequencies is required. For the sake of consistency in the theoretical description to follow, the angular frequencies will be labeled ω_{Probe} and ω_{Pump}, as they are supplied by the respective *Raman probe* and *Raman pump* beams employed in the setup. The photons' energies are $\hbar\omega_{\mathrm{Probe}} > \hbar\omega_{\mathrm{Pump}}$ and the energy difference is equal to that of the Raman active mode,

Figure 4.2: Scheme of the stimulated Raman scattering process. The length of the arrows represent the energy of the photons. When the Raman condition is met, one photon of energy $\hbar\omega_{\mathrm{Probe}}$ is annihilated, whereas one additional photon of energy $\hbar\omega_{\mathrm{Pump}}$ is created.

$$\hbar\omega_{\mathrm{Pump}} = \hbar\omega_{\mathrm{Probe}} - \hbar\omega_{\mathrm{M}}. \tag{4.3}$$

If this *Raman condition* is fulfilled, one photon of $\hbar\omega_{\mathrm{Probe}}$ is annihilated (stimulated Raman loss, SRL) and one of $\hbar\omega_{\mathrm{Pump}}$ is created (stimulated Raman gain, SRG) [111, 118] (compare Fig. 4.2). This leads to an attenuation of the probe and an amplification of the pump. The change in the number of detected photons caused by SRS and/or SRL scales with the magnitude of the Raman band. In the application in this thesis, it is typically of the order of 10^{-4} [119].

Although Raman shifts are often initially expressed in terms of frequency, wavenum-

bers (cm^{-1}) are the most commonly applied unit in Raman spectroscopy (see eq. 4.4). Therefore, in subsequent sections, the Raman shift will be presented in wavenumbers for consistency and clarity.

$$\widetilde{\nu} = \frac{1}{\lambda} = \frac{\omega}{2\pi c} \tag{4.4}$$

By measuring the attenuation or amplification of either of the two beams after interacting with a molecule, the Raman signal can be computed for the energy difference at hand. The most common implementation of SRS, which is portrayed in Figure 4.3, employs two lasers of narrow spectral width to stimulate a Raman active vibration. Several Raman active modes can be probed by tuning the energy of one or both beams to address a different Raman vibration [99, 120]. For SRS to occur, the two photons must arrive at the sample not only in the same position but also at the same time. For that reason, pulsed lasers are usually employed. Each pulse contains many photons within its short duration. They therefore arrive at the sample position at almost the same time. The two light sources are synchronized to ensure an overlap in time for the pulses and, consequently, maximize the number of photons arriving at the sample position at the same time. In a continuous wave (cw) laser, the distribution of photons over time is random. Thus, the likelihood of photons of both beams arriving at the same time and enabling an interaction is low, rendering cw lasers unsuitable for application in SRS.

FSRS is a process based on the same non-linear phenomenon [120, 122] but employs a broadband femtosecond laser pulse as Raman probe, as shown in the comparison between the two techniques displayed in Fig. 4.3. The broadband Raman probe, synchronized with a narrow-band picosecond Raman pump, allows SRL to be measured across the entire spectral range of the probe pulse simultaneously, capturing Raman signals for all vibrational modes that fulfill the Raman condition without the need to sequentially tune the excitation wavelength. Consequently, FSRS provides near-instantaneous spectral coverage, which significantly reduces acquisition times for full Raman spectra compared to SRS. FSRS has been successfully applied in the investigation of ultrafast photochemical reactions, protein folding, and proton transfer reactions, where tracking vibrational changes in real-time reveals functional dynamics [119].

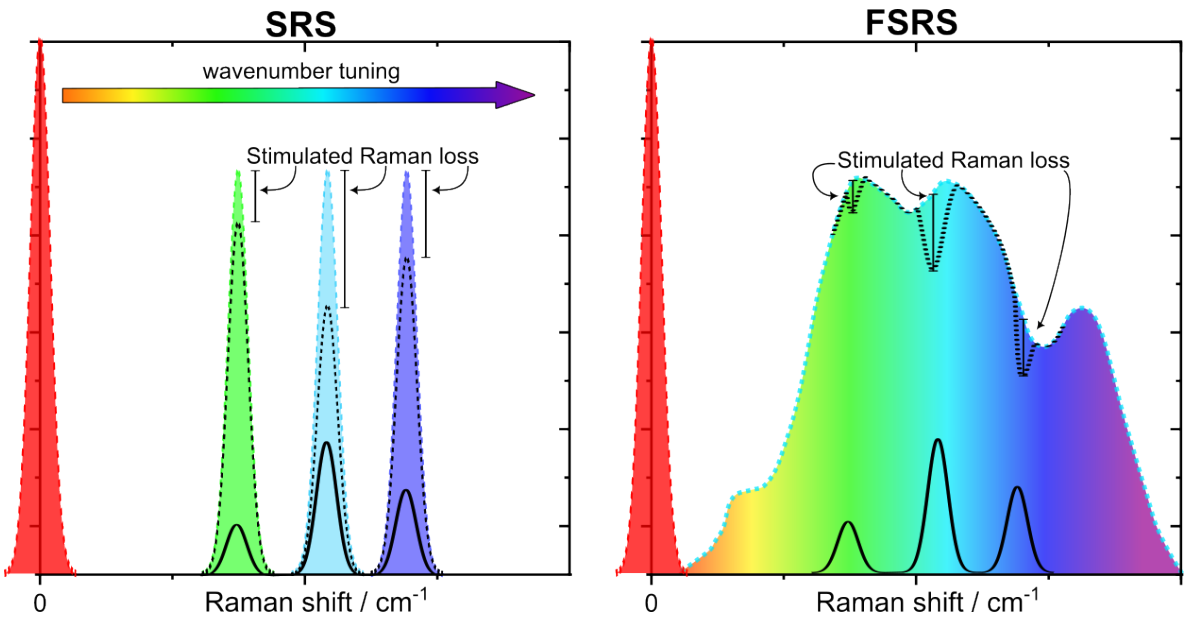

Figure 4.3: A comparison between the most common modality of SRS and FSRS. In conventional SRS (left) two narrow bandwidth laser pulses are employed. Their wavenumber difference is tuned to cover the Raman spectral range to acquire a Raman spectrum (schematically shown in black). If the Raman condition is fulfilled, the high frequency pulse (green to blue colors) will undergo stimulated Raman loss (SRL) from which the Raman signal can be computed. In FSRS (right) a narrow bandwidth Raman pump pulse (red) and broadband probe (rainbow color gradient) are employed. Raman resonances show up as small dips in the probe spectrum for all positions which meet the Raman condition. From these dips the Raman spectrum is obtained. Adapted from ref. [121].

4.2.2 Advantages of FSRM

SRS was first applied in microscopy by Ploetz *et al.* in 2007 in the research group led by Peter Gilch, who supervised this thesis. The technique applied FSRS and was thus termed femtosecond stimulated Raman microscopy (FSRM). Freudiger *et al.* later described a setup based on "conventional" SRS, employing two narrow-band pulses [98]. SRS microscopy has since become a frequently applied technique, especially in biological and medical applications [123]. Advantages of applying SRS for imaging over spontaneous Raman scattering are faster measurements due to increased Raman signal as well as a lower likelihood of spectra being distorted by fluorescence of the sample. Compared to CARS, another advantage of SRS is that the acquired spectra are mostly background-free and closely resemble spontaneous Raman spectra [99]. This enables an easy comparison of results with spectral databases. However, as described in Section 4.2.1, it requires tuning of the wavenumbers of one or both of the laser beams employed. When applying SRS in microscopical techniques, that typically means that within one scan of a sample region, only one Raman shift can be recorded. It is therefore necessary to perform several scans for few selected wavenumbers, compromising spectral coverage.

These wavenumbers can be selected with prior knowledge of the sample's Raman bands. Another method of SRS microscopy is to only record full Raman spectra for selected points of interest, compromising spatial coverage. Either way, some information on the sample composition is lost. FSRM, on the other hand, provides complete Raman spectra for each sample position recorded. Thus, no prior knowledge of the sample's composition and the Raman active modes expected is necessary. Furthermore, it is important to point out that the current modalities of FSRM do not require high laser powers, enabling an acquisition of fast Raman maps without destruction of sensitive samples [124].

4.2.3 Comparing Stimulated and Spontaneous Raman Spectra

Stimulated Raman spectra look similar to those acquired from spontaneous Raman scattering, as the same characteristic Raman active modes are probed and Raman shifts observed are detected. In a quantum electrodynamical view, spontaneous Raman scattering can be treated as a form of SRS driven by the zero-point energy fluctuations of the vacuum electromagnetic field [125]. However, the relative signal strengths of the observed bands are different for spontaneous Raman and SRS spectra, necessitating adjustments to enable quantitative comparisons. The procedure necessary to achieve comparability are summarized here. Only a brief comparison of the acquired spectra will be given in terms of the dependence on the frequency of the detected light, the bandwidth of the exciting light source and the depolarization ratio of the Raman active modes. The derivation of relevant equations has been summarized in literature and previous doctoral theses [118, 126] and is outside of the scope of this thesis.

A germanium diode detector is employed for acquisition of the spontaneous FT-Raman spectra. This diode does not display a uniform spectral responsivity, i.e. the ratio of generated photocurrent to the power of incident light is not the same for every wavelength. Identical light fluxes at different Raman shifts will thus result in non-identical signals. The probability of an incident photon triggering an electric response is given by the quantum efficiency. The spectral responsivity $\mathcal{R}$ [A/W] can be converted into the quantum efficiency η for each detected wavelength λ via eq. 4.5 [127]

$$\mathcal{R} = \eta \frac{e_0}{hc} \lambda \tag{4.5}$$

with the elementary charge e_0, the Planck constant h, and the speed of light c. The quantum efficiency in the relevant region for the respective Raman shift is shown in Fig. 4.4. During the measurements here, the temperature of the detector was approximately 18°C. A reference function for the spectral responsivity at 25°C is the closest

approximation available for calculation of the quantum efficiency. As the responsivity is temperature dependent, the function is expected to deviate from the real values. More accurate values could be obtained by recording a reference spectrum before the measurement. However, such references were not recorded, so the quantum efficiency has to be approximated using reference values. The detector is most efficient for wavelengths which correspond to detected Raman shifts of around 2850 cm^{-1}. This implies that Raman shifts in this region will be displayed as proportionately larger than in other regions, as the detection is more sensitive for the respective scattered photons. This can be corrected for by dividing the recorded spectrum by the quantum efficiency for the respective detection wavelength.

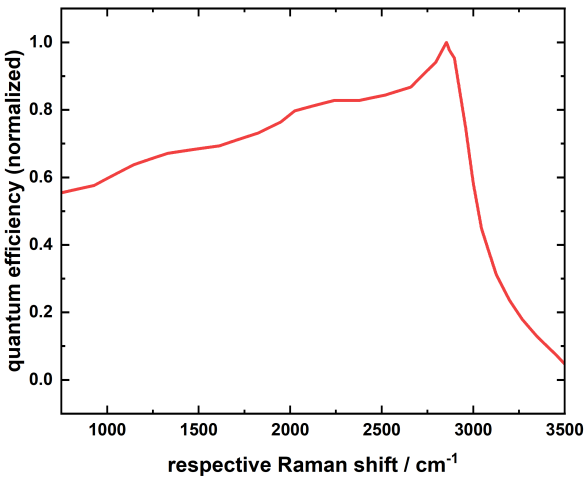

Figure 4.4: Quantum efficiency of the Ge-detector used in the FT-Raman spectrometer at 25°C, shown for the respective Raman shift detected. Calculated based on data from [128]

The differential Raman scattering cross-section describes the probability of Raman scattering to occur and therefore the observed magnitude of the respective Raman band. It is defined as $\frac{d^2\sigma_{\mathrm{SRS}}}{d\Omega d\omega_S}$, with σ_{SRS} describing the scattering cross section of SRS, Ω the solid angle, and ω_{S} the angular frequency of the scattered light. For spontaneous Raman scattering, when considering the zero-point radiation field intensity, this cross section depends on the angular frequency of the incident light ω_i, as well as the scattered light ω_S and the number of molecules per unit volume N, as shown by eq. 4.6. Additionally, the differential Raman scattering cross-section is linearly dependent on the imaginary part of the third-order non-linear susceptibility χ^3_R.

$$\frac{d^2\sigma_{\mathrm{spont}}}{d\Omega d\omega_S} = \frac{\hbar\omega_i\omega_S^3}{\pi c^4 N}\mathrm{Im}\chi^3_R \tag{4.6}$$

χ^3_R is a tensor that describes a molecule's non-linear response to high-intensity optical fields, enabling interactions between the Raman pump and probe with the medium. In SRS, only the imaginary part of χ^3_R contributes to the SRL or SRG, resulting in Lorentzian line shapes in absence of inhomogeneous broadening [118, 119].

The differential scattering cross-section for SRS can be described by taking into account the angular frequency of the pump light, ω_{Pump}, and that of the probe ω_{Probe}, as well as the spectral photon flux $\mathrm{F}(\omega_S)$ (photons $m^{-2}s^{-1}Hz^{-1}$), as expressed by eq.

4.7[119]:

$$\frac{d^2\sigma_{\mathrm{SRS}}}{d\Omega d\omega_S} = \frac{32\pi^2\hbar\omega_{\mathrm{Probe}}\omega_{\mathrm{Pump}}F(\omega_{\mathrm{Probe}})}{c^2N}\mathrm{Im}\chi_R^3 \tag{4.7}$$

The frequency of the incident light of spontaneous Raman, ω_i, corresponds to that of the pump light in SRS, ω_{Pump}, whereas that of the scattered light ω_S corresponds to that of the probe light, ω_{Probe}. Typical spontaneous Raman setups may employ different wavelengths for the excitation of Raman scattering. Within one experiment, ω_i or ω_{Pump} are constant. However, the frequency of detected light, ω_S or ω_{Probe} depends on the Raman shift detected. It is apparent from eq. 4.6 that the spontaneous Raman signal scales with ω_S^3, which, in turn, depends on the excitation ω_i, resulting in detection of different absolute frequencies, according to eq. 4.8

$$\omega_S = \omega_i - \omega_M. \tag{4.8}$$

Converted in terms of wavenumbers $\widetilde{\nu}$ employing eq. 4.4, that dependence is

$$2\pi c \cdot \widetilde{\nu}_S = 2\pi c \cdot (\widetilde{\nu}_i - \widetilde{\nu}_M), \tag{4.9}$$

resulting in a frequency dependence of

$$(2\pi c)^4 \cdot \widetilde{\nu}_i\widetilde{\nu}_S^3 = (2\pi c)^4 \cdot \widetilde{\nu}_i(\widetilde{\nu}_i - \widetilde{\nu}_M)^3. \tag{4.10}$$

Spontaneous Raman spectra will therefore differ slightly depending on the chosen excitation. For the SRS process, the Raman signal scales linearly with the detected frequency of ω_{Probe}, thus the Raman signals scale differently in relation to each other than for the spontaneous process. For both techniques, the frequency of the incident / pump light is a constant factor. The photon flux, which influences the differential cross section of the SRS process, is canceled out by referencing the probe spectra with and without contribution of the pump. A comparison of spectra is challenging if no correction for this frequency dependence is performed.

In addition, also the spectral linewidths need to be considered. The width of the Raman band observed in SRS is determined by the convolution of the bandwidth of the Raman pump employed and of the width of the observed Raman band, as well as the spectrograph's resolution [119].

This correction of spectra will now be demonstrated using the example of benzonitrile, a solvent which is frequently used as a standard for alignments in our laboratory. The normalized spontaneous Raman spectrum of benzonitrile shown in Fig. 4.5(a) fea-

tures Raman bands in different wavenumber regions. The relative signal of the Raman bands at 2229 cm $^{-1}$ and 3072 cm $^{-1}$ will be compared, with a normalization of the spectra for the latter. In the original spontaneous spectrum, their ratio is 3.21:1.

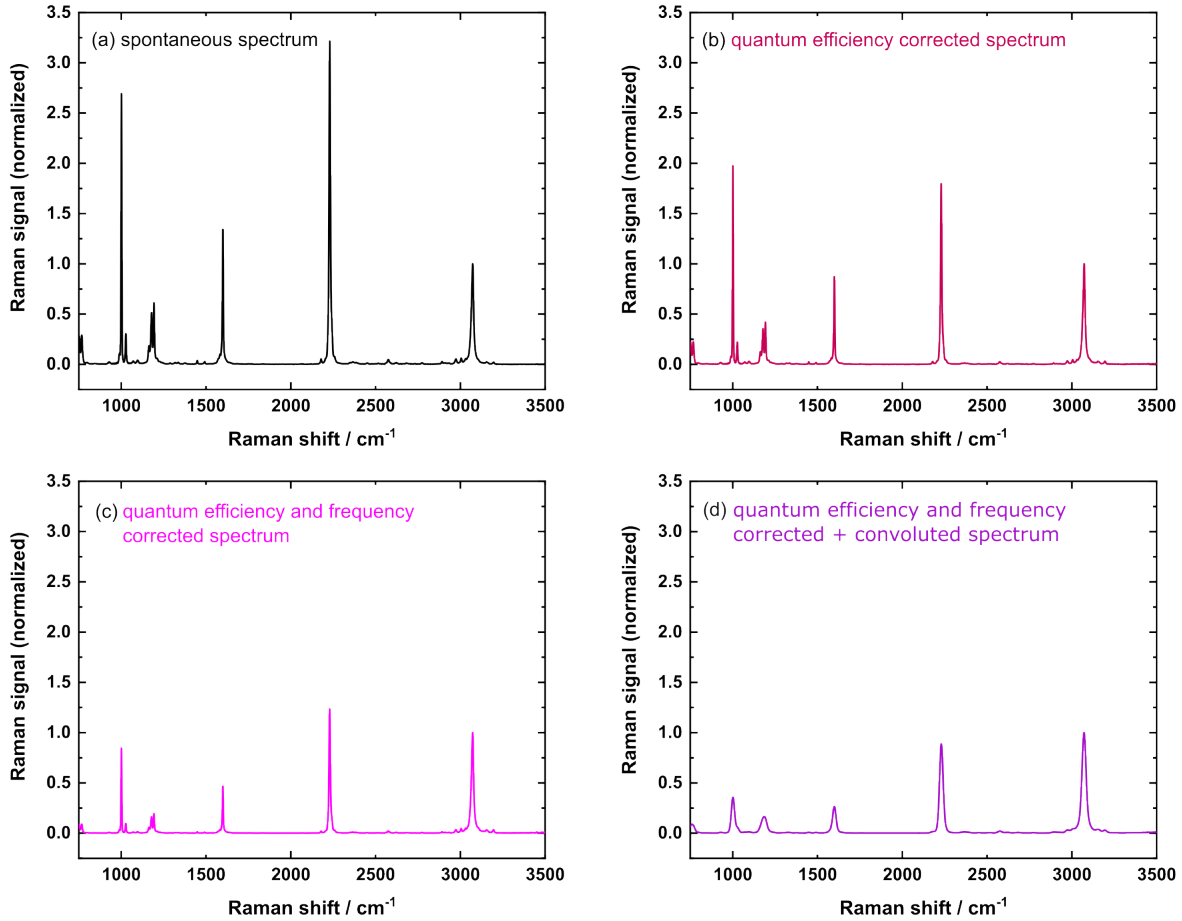

Figure 4.5: Steps in the conversion of spontaneous Raman spectra for comparison with FSRM spectra, illustrated for the example of benzonitrile: (a) original FT-Raman spectrum, (b) spectrum after correction for the spectral quantum efficiency of the Ge-detector, (c) spectrum after correction of spectral quantum efficiency and frequency dependence of the Raman signal on the detected wavenumber, (d) quantum efficiency- and frequency-corrected spectrum after convolution with a Gaussian fit of the Raman pump spectrum. All spectra were normalized for the CH stretching Raman band at 3072 cm $^{-1}$.

First, the recorded spontaneous spectrum is corrected for the spectral quantum efficiency of the germanium diode used to detect the FT-Raman spectra, which is shown in Fig. 4.4. Each Raman signal is divided by the quantum efficiency for the respective Raman shift observed. The resulting normalized spectrum is shown in Fig. 4.5(b). The ratio of the two Raman bands highlighted above decreases to approximately 1.80:1.

Next, the spontaneous spectrum is corrected for the frequency dependence of the detected scattered light. The excitation wavelength employed was 1064 nm (ν_i = 9398 cm^{-1}). Each Raman signal recorded is divided by $(\omega_S)^3$ and the resulting normalized

spectrum shown in Fig. 4.5(c). As a result of the correction, the ratio between the two Raman bands treated here as an example decreases further to 1.23:1.

Finally, the frequency-corrected spectrum is convoluted with a Gaussian fit of the Raman pump's spectrum. The Raman pump, whose width determines the spectral resolution of FSRM, was determined to be approximately 30 cm^{-1} (FWHM). As a result of the convolution, as seen in Fig. 4.5(d), the ratio of the two Raman bands decreases to 0.89:1. The more narrow a Raman band, the more pronounced the expected decrease in its height will be due to the convolution. Furthermore, the lower-wavenumber Raman bands appear to coalesce. In the spontaneous spectrum, three sets of close-lying Raman bands are observed with maxima at 752 cm^{-1} and 768 cm^{-1}, 991, 1001 cm^{-1}, and 1027, as well as 1163 cm^{-1}, 1187 cm^{-1}, and 1193 cm^{-1}. In the frequency-corrected and convoluted spectrum, only three bands with maxima at 761 cm^{-1}, 1002 cm^{-1}, and 1187 cm^{-1} are observed. The broadness of the Raman pump pulse does not enable resolution of these single bands.

An FSRM spectrum of benzonitrile is corrected for the frequency dependence by dividing the Raman signal by the respective angular frequencies ω_{Probe}. For $\nu_{\text{Pump}} = 10\ 235\ cm^{-1}$, this means dividing the FSRM signals by:

$$\omega_{\text{Probe}} = (\nu_{\text{Pump}} - \nu_M) \cdot 2\pi c$$

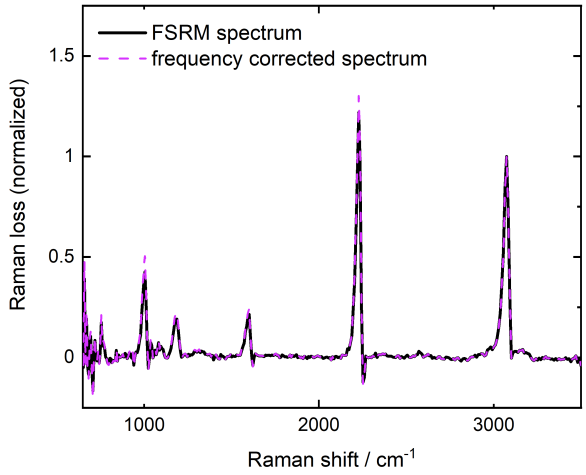

Figure 4.6: Frequency correction of an FSRM spectrum of benzonitrile, recorded within an acquisition time of 1 s. The original spectrum (black, solid line) and frequency corrected spectrum (violet, dashed line) do not differ strongly from each other. Both spectra were normalized for the CH stretching Raman band at 3072 cm^{-1}.

The corresponding FSRM spectra are shown in Fig. 4.6. It becomes apparent that the original and frequency corrected spectrum do not strongly deviate from each other.

An additional factor impacting the Raman signal in SRS will now be discussed. In SRS, two linearly polarized light sources are employed which need to overlap temporally and spatially at the sample position. The polarizations also have to match. Therefore, the stimulated Raman scattering observed also depends on how sensitive a Raman band is to polarization. More precisely, it depends on the depolarization ratio ρ. ρ is defined differently depending on the geometry of detection. The scattered light can be either detected in a 90° angle or a 180° angle relative to the excitation. The latter is also often referred

to as forward-scattering. Depolarization ratios for both are of similar magnitude [111]. In the case of detection of light scattered spontaneously in a 90° angle to excitation, as schematically depicted in Fig. 4.7(a), ρ is defined as follows:

$$\rho = \frac{I^{\perp}}{I^{\parallel}} \tag{4.11}$$

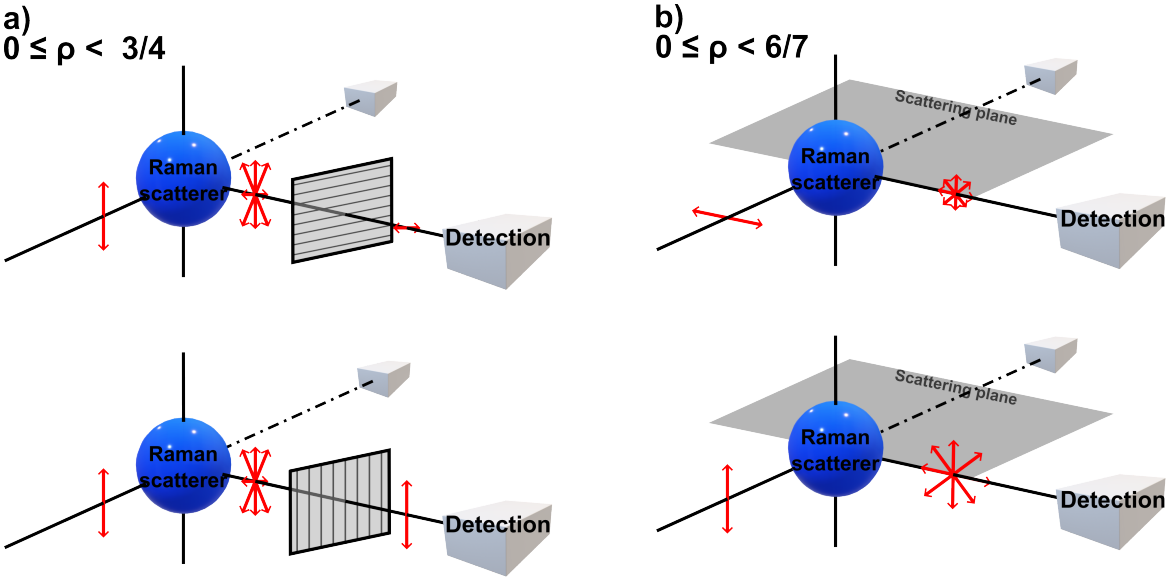

Figure 4.7: Detection geometries for the determination of Raman scattering depolarization ratios. (a) Light scattered spontaneously is detected in a 90° (180°, dotted line) angle to excitation, with a polarizing filter placed perpendicular (top) or parallel (bottom) to the exciting light's polarization. (b) The exciting light is polarized parallel (top) or perpendicular (bottom) to the detection plane and detected in a 90° (180°) angle to excitation.

$I^{\perp}$ denotes the power of scattered light with a polarization perpendicular to that of the exciting radiation, whereas $I^{\parallel}$ denotes the power of scattered light with a polarization parallel to excitation [111]. The value of ρ is in the range $0 \leq \rho < 0.75$ with a value of 0 observed for a completely polarized (isotropic) Raman band and a value of 0.75 for a strongly unpolarized (anisotropic) Raman band. ρ cannot become 1 as all vibrational systems are somewhat polarizable, whereas it is possible for a Raman active mode to be fully polarized and not scatter light with a polarization perpendicular to the incident one [111]. In an alternative determination of ρ, the polarization plane of incident light is either perpendicular or parallel to the scattering plane. A polarized band will show stronger Raman scattering for incident light perpendicular to the detection plane, as shown in Fig. 4.7(b). The detection remains constant. For this case, ρ is in the range $0 \leq \rho < 6/7$ [111, 129]. The two definitions of ρ are convertible. In FSRM, the linearly polarized probe beam acts as an analyzer and scattering is detected in a forward geometry (180°). Consequently, the first case shown in Fig. 4.7(a) applies here [130]. A

strongly polarized band (ρ near 0) will strongly decrease in intensity if the polarization of the two beams becomes gradually more unmatched, whereas a strongly unpolarized band (ρ near 0.75) will be only slightly affected [130].

4.3 FSRM Setup

The development of the FSRM setup over time and the current state can be found in refs. [31, 121, 124, 131]. The setup, which is schematically depicted in Fig. 4.8, is based on a Ti:Sa laser (Femtolasers, Fusion BB 400) with an output centered around 810 nm, a spectral width of approximately 120 nm (FWHM), average light power of approximately 440 mW, and a repetition rate of 75 MHz. The light can be used as Raman probe without further spectral broadening, which is the main advantage of using a femtosecond laser. It is reflected by a beam splitter, at which light with wavelengths > 950 nm is transmitted to be coupled into a fiber amplifier. The reflected probe light passes a delay stage to enable temporal overlap of the two pulses at the sample position. Then, it is guided to two sets of chirped mirrors (Venteon, DCM 7) which introduce a negative chirp. This precompensates the temporal chirp which is caused by the focusing

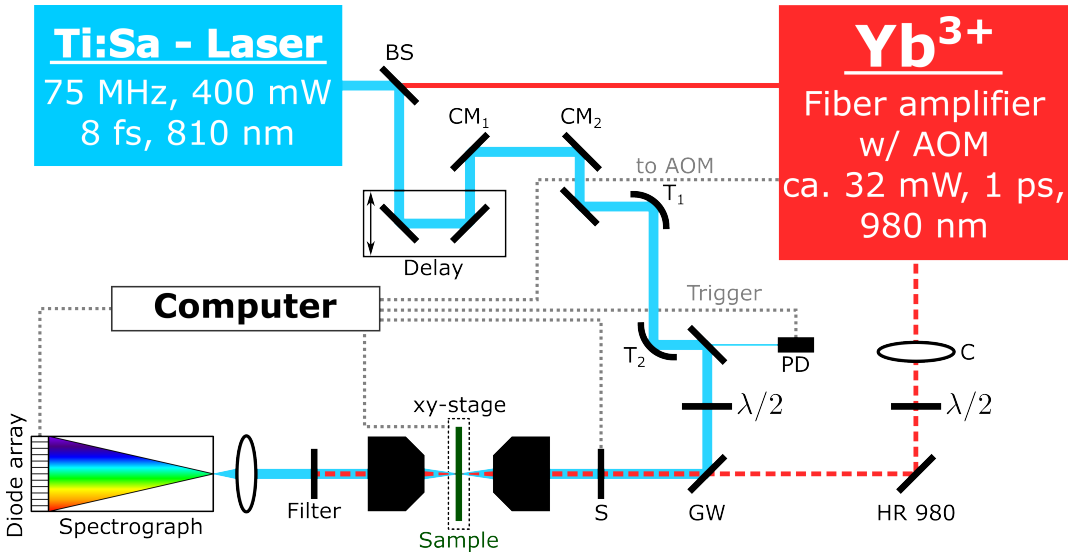

Figure 4.8: Scheme of the FSRM setup. The probe light generated by the Ti:Sa Laser is split by a beam splitter (BS). The reflected light passes a delay stage and two sets of chirped mirrors (CM) and is expanded by a reflecting telescope (T_1 and T_2). A portion of the light is coupled into a photodiode (PD), which is used as a trigger diode. The light passes through a half-wave plate ($\lambda/2$) and is reflected at a glass wedge (GW). The light transmitted by the BS has a wavelength > 950 nm and is coupled into a home-built Yb^{3+}-doped fiber amplifier (compare Fig. 4.9). The amplified pump light is coupled out, remaining light of the pump diode is filtered by a longpass filter (HR980). The beam's polarization is aligned with that of the probe light by a $\lambda/2$-plate and the two beams are recombined at the GW. They are guided into a microscope objective, focused on the sample placed on an xy-stage and the transmitted light is collected by another objective. The pump light is filtered out and the probe light coupled into the detector. Adapted from ref. [132].

objective. The probe beam is broadened in a reflecting telescope, followed by a portion of the light being coupled out to a photo diode, which serves as a trigger to synchronize the probe pulses with the detector readout. The light then passes a λ/2-plate, followed by reflection on a glass wedge in the Brewster angle. Only light with a perpendicular polarization is reflected. Therefore, the probe light can be attenuated by changing the polarization with the λ/2-plate.

After splitting the two beams, the Raman pump pulse is generated. As mentioned above, only wavelengths > 950 nm are transmitted through the beam splitter. This light (with a power of roughly 200 µW) is coupled into a customized fiber amplifier, as schematically depicted in Fig. 4.9, with the help of an aspheric lense (Thorlabs, CFC-11-B-APC). Generally, polarization maintaining fibers of type Hi1060 (Corning) are applied except for the active fibers, which are doped with Yb^{3+} (Liekki, Yb1200- 4/125). The light enters at the first port of an optical circulator (Precision Micro-Optics), a device in which light that enters in any one port will exit from the next. Thus, the light exits the circulator at the second port. It then passes a wavelength division multiplexer (WDM), where it is mixed with light from a pump diode (Axcel Photonics, BF-915-0200-P5A). The diode supplies cw-light with a wavelength of 915 nm, which pumps the Yb^{3+}-doped fiber and induces a population inversion. The seed light and light to pump the amplifier pass the first active fiber, which is approximately 5 cm long, and amplifies the pulsed seed light at a wavelength

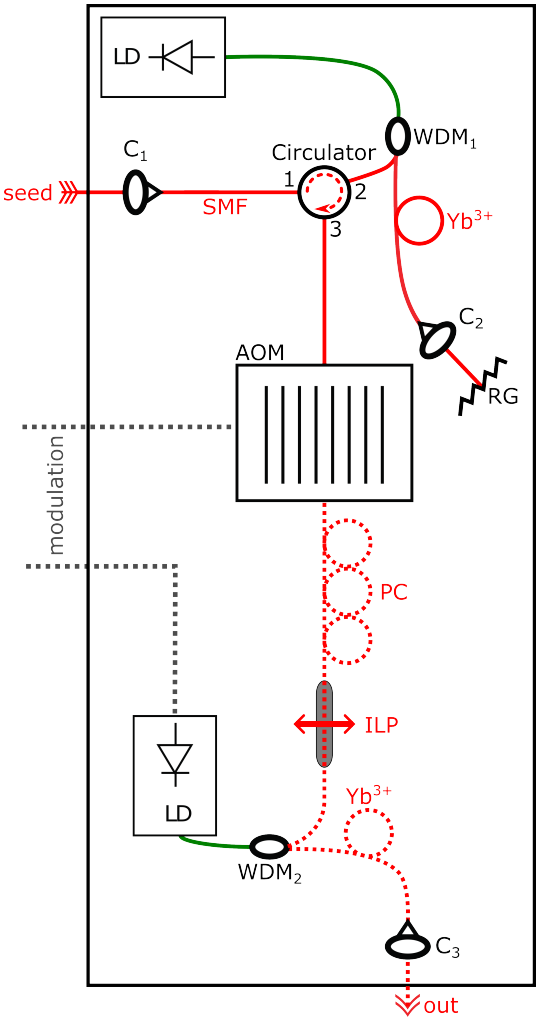

Figure 4.9: Scheme of the fiber-doped amplifier. The seed light is coupled into or out of the single mode fiber (SMF) using lenses (C). Wavelength division multiplexers (WDM) mix the seed light with light of a laser diode (LD), which pumps the active fibers (Yb^{3+}), in which the seed light is amplified. A refractive grating (RG) narrows the light spectrally after the first step of amplification. An acousto-optic modulator (AOM) is employed for the on/off-modulation of the pre-amplified light. A polarization controller (PC) adjusts the polarization and an in-line fiber polarizer (ILP) further attenuates light of different polarization before a second step of amplification. Adapted from [132].

of 977 nm. The spectral width after the first step of amplification added by the diode light is narrowed by coupling the light out of the fiber and focusing it on a reflective grating using a lens. Only the desired wavelength is coupled back into the fiber. The narrowed light passes the first active fiber and the WDM again before entering the circulator in the second port, which it exits at the third port. Next, the pre-amplified pulsed light passes through an acousto-optic modulator (AOM) (AA Opto-Electronic, AA.MT8O.IR6O.FIO-SM5-J3V-A) which enables periodically turning the pump pulse on and off for 50 µs each, synchronized with the detector readout rate. During the "off"-phase of the AOM, the power of the second laser diode which pumps the second stage of amplification is reduced. This was implemented because the first few pulses of each train of Raman pump pulses passing from the amplifier had been observed to display much higher peak powers than the rest of the pulses, caused by a large population inversion building up in the active fiber during the off-phase. Reducing the power of the laser diode during the off-phase reduces the population inversion, which suppresses the high peak powers in the beginning of the on-phase, ultimately preventing damage to samples [124]. After passing the AOM, the pulsed light is guided through a fiber-based polarization controller (Thorlabs, FPC030) to adjust the polarization. The polarization is further controlled by passing through an in-line fiber polarizer (Thorlabs, ILP850PM-APC), which attenuates unwanted light with an orthogonal polarization. Finally, the pulsed light is mixed with the pump light of a second laser diode in a WDM, as described above, and passes a second active fiber, where it is amplified to its final power. The Raman pump is coupled out of the fiber using a microscope objective (Zeiss, 10x, NA 0.22, AR 1.06). A longpass filter removes the transmitted light of the laser diode. A $\lambda/2$-plate enables aligning the polarization of the Raman pump with that of the Raman probe. The light is thus amplified from $\approx$ 200 µW which enter the fibers to $\approx$ 32 mW measured at the entrance of the microscope objective.

The amplified Raman pump beam is expanded in a telescope and recombined with the Raman probe at the glass wedge. The beams are coupled into a microscope objective (Zeiss, Fluar, 20x, NA 0.75) by a periscope. At the entrance of the microscope objective, the Raman probe beam usually has an average power of around 2 mW. Both beams are focused on the sample placed on an piezo-xy-stage (Princeton Instruments, P-542.2CD). During scanning, this stage moves continuously in a zigzag-pattern. In this manner, technically every probe spectrum is measured in a slightly shifted position from the one before. However, this distorts the generated false-color images only slightly [132]. The piezo stage is placed on another xy stage which can manually be adjusted for rough alignments before starting a measurement.

After interacting in the sample, both beams are transmitted and collected by a

second objective (Zeiss, Achroplan, 100x, NA 1.25). The remaining Raman pump light is filtered out by passing a shortpass filter. Finally, the remaining Raman probe light is guided into a polychromator where it is spectrally dispersed to be detected by a diode-array detector (Quantum Detectors, ULTRA). The detector has 512 pixels and a readout rate of 20 kHz. One readout of the detector takes 50 µs. The trigger mentioned before synchronizes the detection with the start of a phase when the Raman pump train is modulated on or off by the AOM. Two consecutive readouts always consist of one Raman probe spectrum in presence $S_{Probe+Pump}$ and another one in absence S_{Probe} of the Raman pump as a function of the probe wavelength λ_{Pr}.

With $\lambda_{\mathrm{Pump}} = 977$ nm as the central wavelength of the Raman pump, the recorded wavelengths are converted into Raman shift via eq. 4.12 (derived from eq. 4.3):

$$\tilde{\nu} = \frac{1}{\lambda_{\mathrm{Probe}}} - \frac{1}{\lambda_{\mathrm{Pump}}}. \tag{4.12}$$

The Raman signal for each wavenumber $R(\tilde{\nu})$ is computed by referencing the probe signals in presence and in absence of the pump via eq. 4.13

$$R(\tilde{\nu}) = 1 - \frac{S_{\mathrm{Probe+Pump}}(\tilde{\nu})}{S_{\mathrm{Probe}}(\tilde{\nu})}. \tag{4.13}$$

The corresponding spectra $S_{Probe+Pump}$ and S_{Probe} are averaged separately before this calculation.

FSRM maps recorded are impacted by the position of the sample relative to the focal plane. These sectioning capabilities arise from the fact that the SRS process is primarily sensitive to material located at or near the microscope's focal plane [133], as shown schematically in Fig. 4.10. If a particle or material is not (fully) positioned within the focal plane, this will be reflected by the spatial distribution of the Raman loss recorded. For material within the focal plane, Raman loss will be higher than for regions outside of the focal plane.

The position of the sample relative to the focal plane also affects the transmission of the Raman probe light applied. One advantage of the recorded data is that the probe spectra for each position can be applied to also calculate a transmission map, without the need of any further measurements or even use of different setups. As the SRL is small compared to the total probe light recorded, it is not considered and all spectra recorded for a position $S_{Probe,sample}$ are averaged for the calculation. An initial spectrum is recorded in a position with high transmission (water for the samples relevant in this thesis) $S_{Probe,water}$ before the scan and used to calculate the averaged transmission T over the spectrum of 512 pixels for each sample position, as shown in eq. 4.14, with $\tilde{\nu}_{\mathrm{i}}$

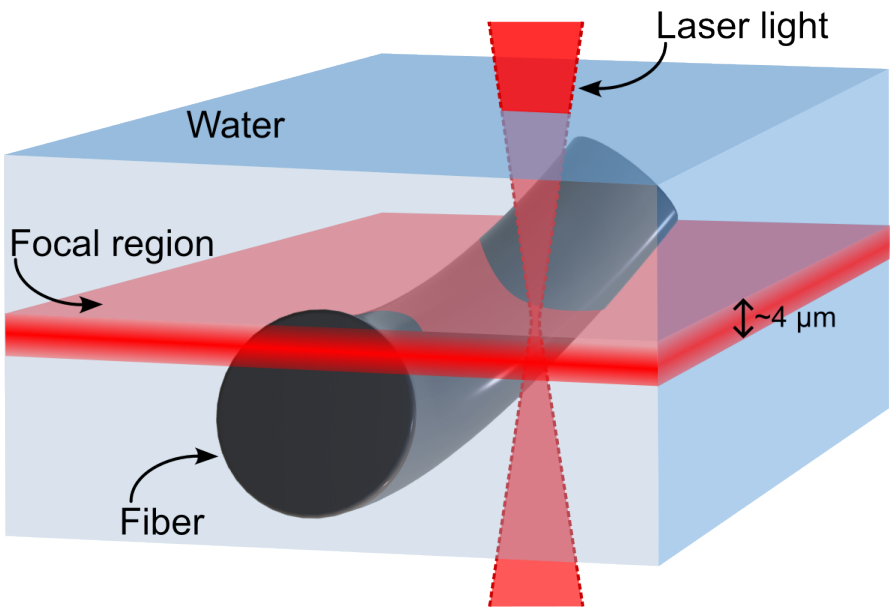

Figure 4.10: Sectioning capabilities of FSRM demonstrated for the example of a fiber positioned only partially within the focal plane. In SRS, Raman scattering is stimulated mostly for material in or close to the focal plane. From ref. [121]

denoting the wavenumbers assigned to each of the 512 pixels of the detector.

$$T = \frac{1}{512} \sum_{i=1}^{512} \frac{S_{\text{Probe,sample}}(\tilde{\nu}_i)}{S_{\text{Probe,water}}(\tilde{\nu}_i)} \tag{4.14}$$

5 Experimental Methodology

5.1 Sample Selection and Preparation

Comparison of spontaneous and FSRM Raman spectra of solvents

For comparison of spontaneous Raman spectra with FSRM spectra, the following solvents were used: benzonitrile (> 99.0 %, Tokyo Chemical Industry Co.), acetonitrile (> 99 %, CHEMSOLUTE), toluene (≥ 99.8 %, Fisher Scientific), methanol (≥ 99.9 %, Fisher Scientific), propan-2-ol (≥ 99.5 %, Fisher Scientific), and ethanol (gradient grade for liquid chromatography, Sigma-Aldrich).

Spontaneous Raman spectra were recorded using a FT Raman spectrometer (Multiram, Bruker), made accessible by the group of Prof. Janiak. Solvents were placed in a 1 mm cuvette. Raman spectra were acquired using a Nd:YAG laser with 1064 nm emission and at a power set to 600 mW. The detector employed is a germanium diode detector. As explained in Section 4.2.3, this detector does not have an equal responsivity for all wavelengths recorded. This means that for some Raman shifts, the quantum efficiency of detection is higher than for others. Photons scattered with the respective energy are more likely to be detected than those which lie in regions of lower responsivity, where photons are not detected as well. Reference functions for the detector's spectral responsivity are available for different temperatures. During the measurements shown here, the detector temperature was approximately 18°C. The closest temperature for which a spectral responsivity function of the detector is available is 25°C. The resulting spectral quantum efficiency was shown before in Fig. 4.4 for the respective Raman shift recorded in the relevant region.

For FSRM measurements, 17 µL of the solvents were dropped on an object slide (Menzel, 24 x 60 mm, #1) using an Eppendorf® pipette. The drop was immediately covered with a second cover slip (Menzel, 18 x 18 mm, #1) and the sides sealed with clear nail polish to prevent evaporation. The prepared sample was placed on the xy-stage of the FSRM and a single spectrum is recorded in one position.

Microbeads

Two different standards were used as microbead samples. Poly(methyl methacrylate) (PMMA) beads were acquired from micro particles GmbH. They have a diameter of 21.83 µm with a standard deviation of 0.35 µm. The standard is a 10 wt% suspension in water (Lot: PMMA-F-L-621-10 mL). Polystyrene (PS) beads were acquired from Thermo Fischer Scientific. They have a diameter of 11 µm. No information on the standard deviation of the diameter is available. The standard is a ∼ 4 wt% suspension

in water.

For preparation of microbeads samples, water of HPLC gradient quality (Fisher Chemical) was used. The PMMA standard was diluted with water in a 1:1 volume ratio (1 mL of standard, 1 mL of water). The PS standard was not further diluted. For FSRM sample preparation, 9 µL of each sample was used.

Consumer goods (facial scrub)

As examples of consumer goods containing primary MP, two facial scrubs were analyzed: *ULTRA Rapid Action Akut* from Clearasil, which contains polyethylene, and *Sébium Gel Gommant Exfoliating Purifying Gel Peelinggel für aknöse Gesichtshaut* from Bioderma, which contains cellulose acetate.

It was attempted to dissolve the products in distilled water for filtration. This was unsuccessful for the Clearasil facial scrub. In the course of the bachelor thesis of Lars Fuxen [134], it was unsuccessfully attempted to extract the MP particles. This will not be further described here. The Bioderma facial scrub easily dissolved in water, leaving only MP particles in suspension after dilution.

Microfibers

For measurement of microfibers, undyed fabric samples were selected to prevent light absorption by dyes or pigments, as FSRM measurements are conducted in transmission. The chosen fabrics included nylon, polyester, and linen, sourced from *Stoffe Wolle Kurzwaren Weinreich* in Düsseldorf, Germany. Additionally, a wool fabric sample was obtained from *Axel Suijker Textil* in Quakenbrück, Germany, and a denim fabric sample was taken from a used pair of jeans composed of 69% cotton, 26% polyester, 4% viscose, and 1% elastane.

Approximately 0.6 mg of each fabric was cut into small pieces using scissors. The fragments were further broken down into smaller particles by placing them in distilled water and manually tearing them apart with two spatulas. The resulting liquid, containing the particles, was transferred to a volumetric flask and shaken for 3 minutes, followed by filtration as described below.

For the measurements of microfibers created from denim fabric, it was necessary to bleach the fabric. Sodium hypochlorite (NaOCl) was chosen as a bleaching agent. This choice was based on its effectiveness in procedures designed to extract microplastics from soil organic matter without significantly damaging the plastic [135]. The denim fabric was first soaked in distilled water for 30 minutes before being transferred to a 6.5% NaOCl solution, following a sample preparation protocol described by Palanisamy *et al.* [136]. After 2 hours of bleaching, the fabric exhibited visible discoloration. The

bleached fabric was then rinsed with distilled water using a filter, and the sample was prepared following the procedure outlined above.

Filtration of particles suspended in water

The workflow for all aqueous samples analyzed in this thesis is summarized in Fig. 5.1. The solutions prepared as described above were filtrated over an aluminum oxide filter (0.2 µm, Whatman®, Anodisc®, 25 mm Ø) using a vacuum pump. The filter was specifically chosen as the material is transmissive when wet and does not feature disturbing Raman signals in the relevant wavenumber regions [87]. The wet filter was positioned onto an object slide (40 x 60 mm, #1 thickness) and covered with a round cover slip (25 mm Ø). To ensure that the filter remained sufficiently wet during the measurement, additional water was pipetted between the cover slip and the filter using an Eppendorf® pipette. The edges of the cover slip were then sealed with clear nail polish to prevent evaporation of water.

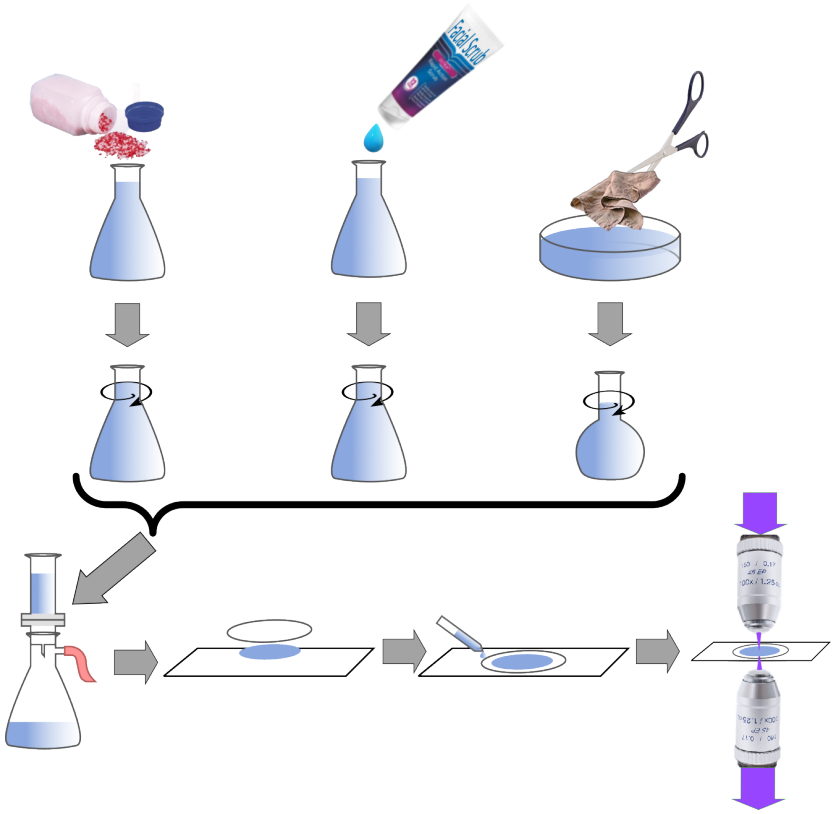

Figure 5.1: Scheme of sample preparation. The samples are first diluted in water. For polymer beads and facial scrub, the sample is added to water and mixed. For fibers, the fabric is cut as small as possible and further dissected using two spatulas before being transferred to a volumetric flask and shaken. After this step, all sample types are treated in the same manner: The sample is filtered using a vacuum pump, transferred to an object slide, and covered with a cover slip. Water is added before sealing the cover slip. Finally, the sample is placed in the FSRM for measurement.

5.2 FSRM measurements

An object slide containing a sample prepared like described above was fixated on the piezo stage. For inhomogeneous samples, an approximate sample position was located visually by using the microscope objectives as a conventional light microscope. The laser light was blocked, a white light lamp placed in the entrance of the focusing objective and the image of the sample was projected onto a white paper placed under the collecting objective. A position of interest was located and the lamp removed. After unblocking the laser beam path, the laser light was roughly focused visually on the white paper. The focus of the two objectives and the focal plane were then optimized by maximizing the probe signal in the detector as well as the detected Raman loss. Single Raman spectra could be recorded. Before acquisition of a map, the Raman probe needed to be adjusted. The alignments before a measurement were for maximum signal in a chosen position. This included increasing the power of the Raman probe until almost saturation of the detector to acquire a single image with a signal-to-noise ratio (SNR) as low as possible for that position. However, during a scan, the stage moves and it is possible that some regions of the sample are more transmissive for the probe light than the point used for alignments. To avoid saturation of the detector, the power of the Raman probe was decreased by turning the $\lambda/2$-plate, which decreased the Raman probe light reflected at the glass wedge. This, in turn, also lead to increased noise observed in the Raman spectra acquired afterwards and a lower SNR. Thus, the saturation threshold of the current detector is a factor limiting SNR.

During the acquisition of a Raman map, the piezo stage on which the sample is mounted moves continuously back and forth in a zigzag pattern to systematically cover the sample region. The speed of movement is adjusted so that the stage moves the chosen step-size within the chosen acquisition time. This means that spectra are not all recorded in one point before the stage moves to the next point for acquisition of the next spectrum, but that each averaged spectrum representing one spatial pixel will be composed of spectra recorded in slightly shifted positions towards each other. This configuration was chosen as it significantly decreases the time required for a measurement and does not substantially affect the generated spatial map [132]. For most FSRM measurements shown in this thesis, 100 FSRM Raman spectra were averaged for each pixel, i.e. 200 probe spectra were recorded, resulting in an acquisition time of 10 ms per pixel. The main reason was that, at faster scanning speeds, it was observed that the movement of the sample stage would also move the samples. A displacement of particles was often visible in the generated FSRM maps.

5.3 Selected Statistical Methods

In the following sections, an overview of the statistical methods that were used to evaluate the samples will be given. The simplest and most straightforward evaluation of hyperspectral images, like those recorded with FSRM, is a univariate analysis which describes the strength of one spectral characteristic for each spectrum recorded, for example a single Raman band or an integral of one. However, as one advantage of FSRM is that it generates broadband Raman spectra, information would be lost if one only focuses on a single aspect of the hyperspectral dataset. A multivariate analysis, which considers multiple spectral regions, ideally the whole spectrum, can give more insight into the data at hand and potentially uncover patterns which had been unknown before.

The statistical methods used here were a clustering algorithm called fuzzy c-means (FCM) [137, 138] and a technique for reduction of dimensionality called principal component analysis (PCA) [138–142]. In the context of this thesis, only a brief overview of how the applied algorithms work will be given. The mathematical backgrounds of these standard algorithms will not be detailed here.

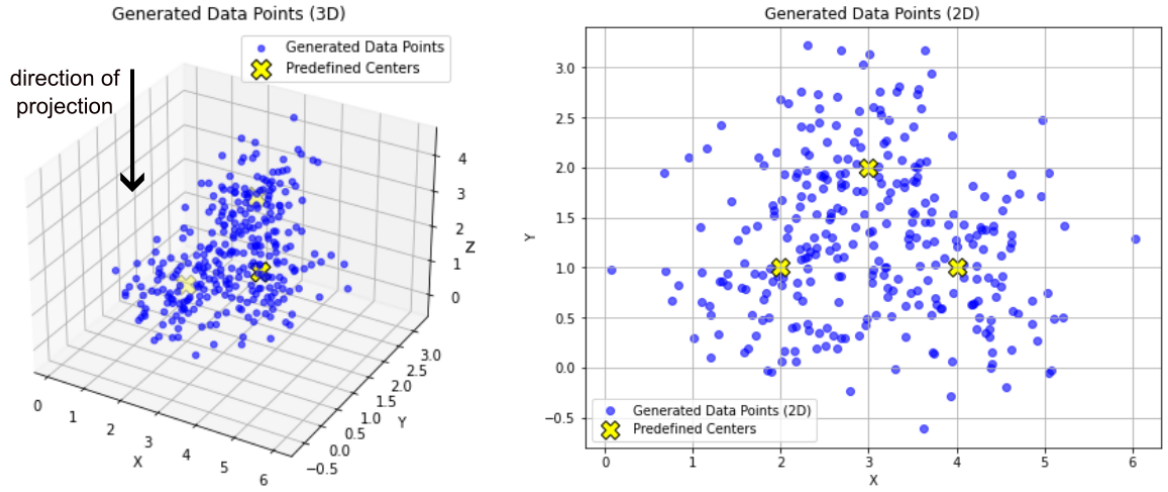

Figure 5.2: Randomly generated data points for visualization of statistical methods employed. A total of 300 points were generated around three predefined centers ([2, 1, 1], [4, 1, 2], and [3, 2, 3]) with a standard deviation of 0.6. The same dataset is plotted in 3D (left) and as a 2D projection (right) for better visualization and comparison.

The algorithms will be visualized here by a dataset of randomly generated points, of which plots are shown in Fig. 5.2. A three-dimensional dataset was chosen to enable both FCM and PCA evaluations. The points of the dataset have been chosen because they were found to achieve a good visual representation of the algorithms used. The dataset consists of 300 points randomly generated in three dimensions around three

predefined centers with a standard deviation of 0.6. The three centers are [2, 1, 1], [4, 1, 2], and [3, 2, 3]. In terms of an FSRM measurement, the three dimensions might represent three different Raman shifts. For example, values along the x-axis might represent the Raman signal strengths detected for the aromatic C=C stretching vibration observed for polyester at 1614 cm^{-1}, the y-axis that of the CH stretching vibration at 2843 cm^{-1} observed in polymers like nylon and polyester, and the z-axis that of the OH stretching of water, observed at 3133 cm^{-1}.[1]

5.3.1 Fuzzy C-Means Clustering

The fuzzy c-means algorithm is a clustering algorithm, which means that it is employed to split data into different groups, called clusters. Clusters are most often defined by being homogeneous internally, i.e. data points within a cluster are similar, and heterogeneous externally, i.e. objects grouped in different clusters show low similarity [143]. The centroid of a cluster is the center of all data points in the corresponding cluster. To describe FCM, first, a general description of the common clustering algorithm k-means clustering [144] will be given, of which FCM is a variation. K-means is a hard clustering algorithm. This means that each object is partitioned into only one cluster. Simply speaking, the centroids of the clusters are iteratively adjusted until a specified point of convergence is achieved [145], often corresponding to the minimization of a criterion of distance (e.g. root mean squared error or Euclidian distance) between the centroids and all objects in the respective clusters.

Usually, k-means clustering follows a pattern of five steps [143, 146]:

1. The number of clusters is chosen manually. This implies that some prior knowledge about the data is required or needs to be found by testing different values.
2. The centroids are initialized, i.e. they are randomly set or estimated as starting points.
3. Each object in the dataset is classified by assigning it to the cluster of its nearest centroid.
4. The centroids are recalculated.
5. Steps 3 and 4 are repeated until the distance between the centroids and the objects is minimized. The mean squared error is a common measure for this distance.

[1] Negative values appear in the generated dataset due to the parameters employed in its generation. However, Raman spectra typically do not display negative values. The description of the generated data in terms of observed Raman shifts is abstract and does not directly correspond to experimentally acquired spectra.

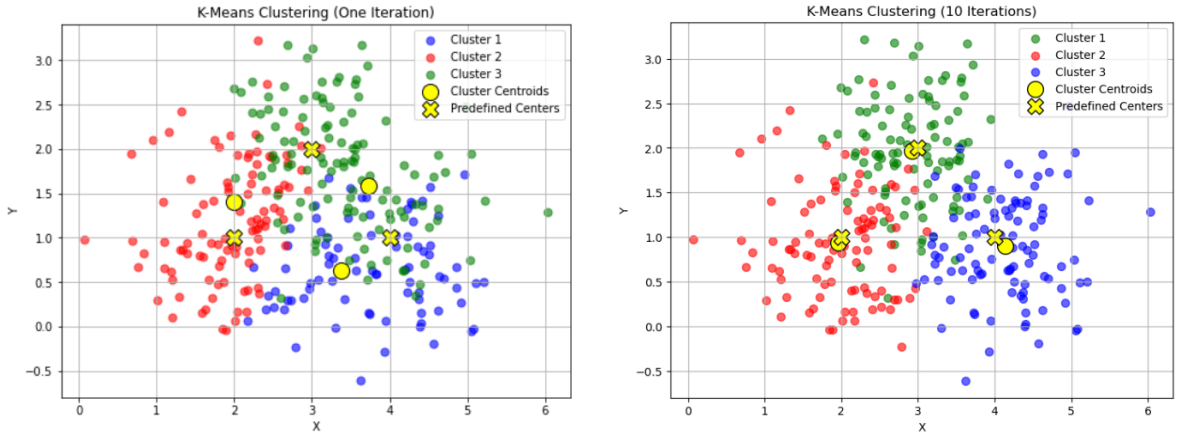

Figure 5.3: Visualization of the k-means clustering algorithm. On the left, one iteration was performed for clustering. On the right, 10 iterations were performed. The distance between the calculated centroids and the predefined centers is visibly larger in the case of only one iteration compared to that after 10 iterations, at which the algorithm classified the distance between the objects in each cluster and the corresponding centroids as the achievable minimum.

For the exemplary dataset shown above, the number of clusters chosen is 3, as it is known that three centers define the dataset. As shown in Fig. 5.3, for one iteration of this process, where the centroids have been estimated only once, the three calculated centroids deviate strongly from the predefined centers. Iterating through the process several times moves the centroids closer to the predefined centers. In the evaluation at hand, the maximum number of iterations the algorithm was allowed to do was set to 20, a minimum was determined after a total number of 10 iterations. For purposes of better visualization, the data is represented as a 2D projection on the xy-plane. It is important to mention that clustering methods like k-means are susceptible to getting "stuck" in local optima [146]. As the starting points are set at random and the process is iterative, it is possible that a position of the cluster centroids yields a minimum distance locally but globally, different positions would result in an even lower distance between the centroids and the assigned cluster's data points. It is therefore often advisable to optimize the algorithm's parameters by running it several times with different initial centroids. This has not been observed to be a problem with the generated dataset.

FCM [137] is based on a similar process but instead of assigning each object to strictly one cluster, the algorithm allows objects to belong to clusters with a certain degree of membership, ranging from 0 to 1 [143]. This continuum of degrees of membership is called "fuzziness" [147], hence the name fuzzy c-means. This fuzziness enhances a partition like k-means as it enables exploring substructures within the dataset which would be lost by hard partitioning of objects into the clusters. It is important to note that the degree of membership does not describe a probability but rather a weighting

factor. Degrees of membership to all clusters do not necessarily add up to 1.

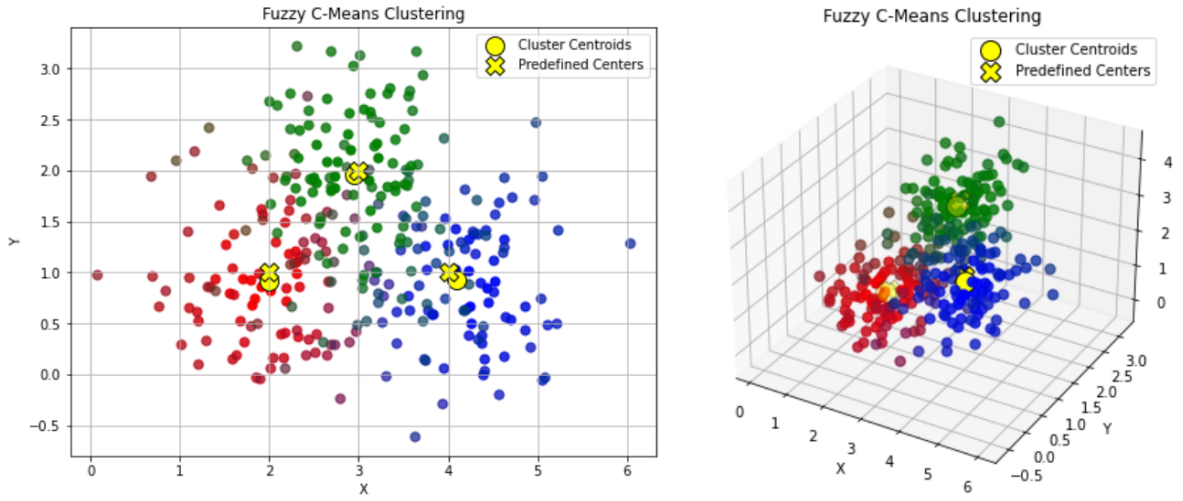

Figure 5.4: Visualization of the fuzzy c-means clustering algorithm for the generated dataset in 2D (left) and 3D (right). The algorithm stopped re-calculating the centroids after a total of 39 iterations.

The results of the FCM algorithm are visualized in Fig. 5.4. Similar to k-means clustering above, a maximum number of iterations is set for the algorithm to perform. Here, due to the specific program used, it is 150. The algorithm stopped after a total of 39 iterations. A color gradient represents the degrees of membership of the objects to each cluster. For the three-dimensional view, there is gradual change of the objects' colors towards the next closest cluster.

For a dataset generated in an FSRM measurement, the clustering algorithm works in the same manner. Above, it was already mentioned that the values for x, y, and z might represent the Raman signal strengths at 1614 cm^{-1} (aromatic C=C stretching), 2843 cm^{-1} (CH stretching), and 3133 cm^{-1} (OH stretching). For an FSRM measurement of nylon and polyester in water, which consists of 40 000 spectra (200 times 200 spatial pixel), the values for these three Raman bands can be extracted and plotted in 3D, as shown in Fig. 5.5. For the sake of better visualization, only every 20^{th} data point is shown.[2]

The results of an FCM analysis of the dataset are shown in Fig. 5.6. Again, only every 20^{th} point of the dataset is included. Note that here, no color gradient was added to represent degrees of membership, as it was found to distort the visualization. Apparently, when only plotting every 20^{th} point, most points belonging to cluster 1 (red) are missing, suggesting that only few points belong to that cluster.

[2]Negative values observed can be attributed to noise patterns for spectra which do not display a Raman band at the respective Raman shifts or a baseline shifted to negative values, for example.

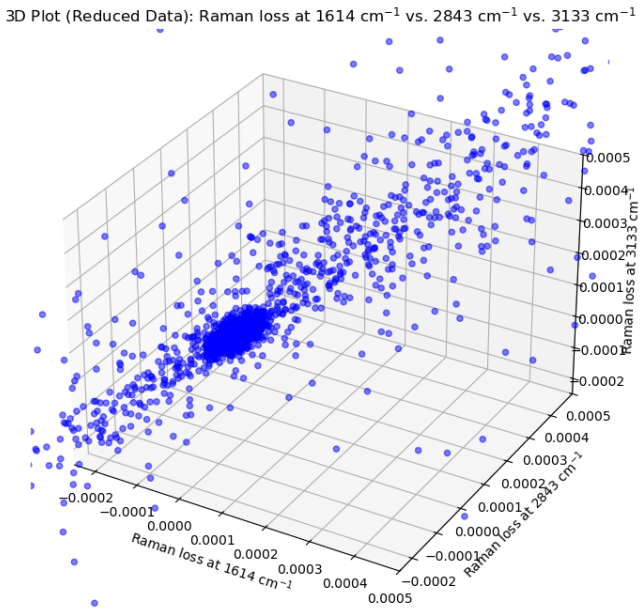

Figure 5.5: 3D plot visualizing the Raman signal at 1614 cm^{-1} (x-axis), 2843 cm^{-1} (y-axis), and 3133 cm^{-1} (z-axis). Each point represents one object (a.k.a. one spectrum) from the dataset with the respective values for the three relevant Raman bands represented by the position along the respective axis. The FSRM dataset at hand is a measurement of a sample of polyester and nylon in water. For better visualization, only every 20^{th} data point is shown and the axis limits were adapted to exclude outliers.

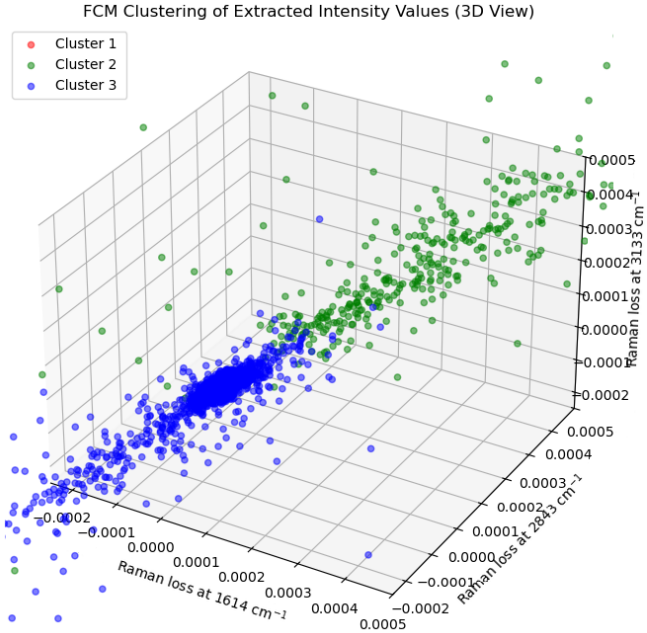

Figure 5.6: Plot of the FCM results for the exemplary FSRM measurement of nylon and polyester fibers in water. Each object is represented by one point color-coded according to the FCM cluster for which it has the highest degree of membership. For better visualization, only every 20^{th} data point is shown and the axis limits were adapted to exclude outliers.

Eventually, this evaluation is employed for Raman imaging data, so it should be represented in form of a map. This can be achieved by grouping the list of 40 000 objects in a matrix of 200 x 200. The 200 lines and 200 rows are then plotted, with each of the objects colored according to the FCM cluster for which it has the highest membership gradient, as shown in Fig. 5.7.

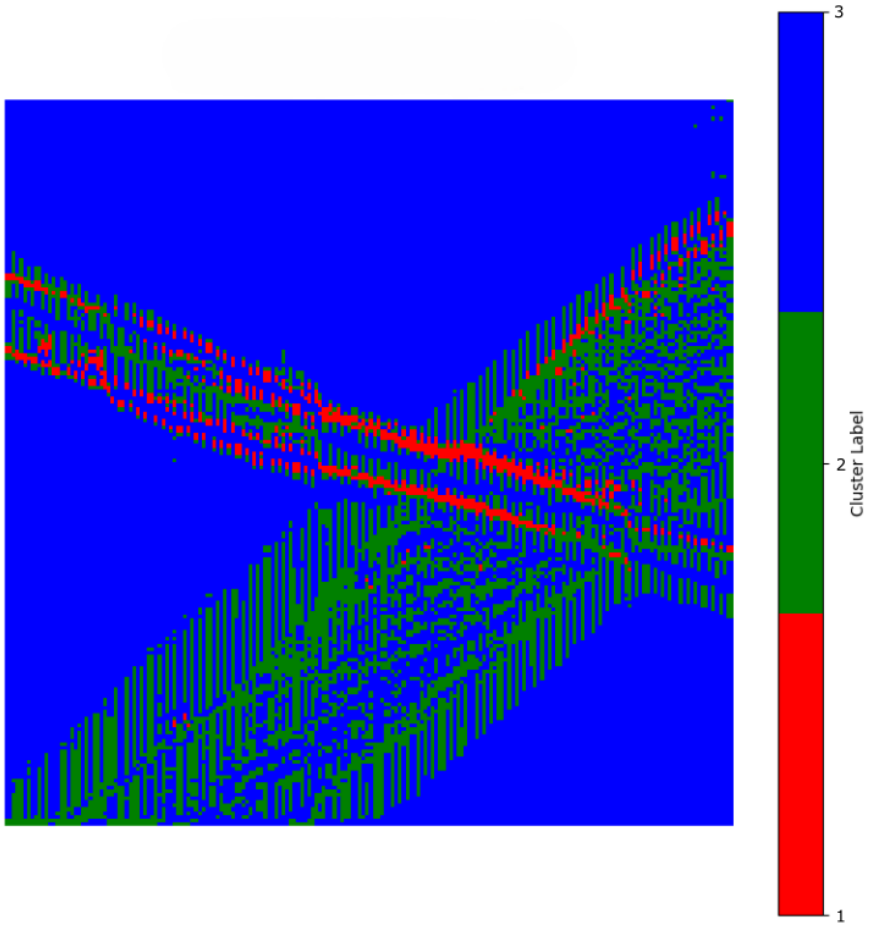

Figure 5.7: Contour plot of the FCM results for the exemplary FSRM measurement of nylon and polyester fibers in water. Each object (i.e. each spectrum) in the dataset is represented as one point assigned the color of the respective FCM cluster for which it shows the highest degree of membership. No color gradient was applied to represent degrees of membership for better visualization.

Here, the above assumption is verified that only few points belong to cluster 1. At this point, the data will not be more deeply discussed, as the parameters were not optimized for this calculation. Due to the experimental design and samples used, it is known that the larger, mostly green shape observed in the map belongs to nylon, the smaller one to polyester. An analysis with better parameters and a deeper discussion of the measurement evaluated here can be found in Section 6.2.3.

5.3.2 Principal Component Analysis

Principal component analysis (PCA) is an algorithm employed to reduce the dimensionality of large datasets while maintaining the most important information. The technique has been described in various ways and under different names over time [139–142]. Essentially, PCA is used to explore unknown data by identifying significant features, called principal components (PCs). Especially in large datasets, covariances, which are measures of linear relationships between different criteria [148], can be identified using PCA. In a dataset consisting of Raman spectra, each spectrum is one object, described by a certain number of variables, i.e. Raman shifts. Thus, a PCA can reveal correlations in variations of the Raman signals at different wavenumbers. Again, the explanation of the steps of a PCA given here will neither include the mathematical deduction of the technique nor go into detail on how the eigenvalue problem is solved. In principle, a PCA follows five steps:

1. The data is centered. This is achieved by calculating the mean of each variable and centering the dataset around these values.

2. A covariance matrix is computed. With this, the covariances among the variables can be measured.

3. The eigenvalues and eigenvectors of the covariance matrix are calculated. The direction of the principal component is defined by the eigenvectors, while the variance of the dataset explained by each eigenvector is represented by the corresponding eigenvalues. The number of eigenvectors equals the number of variables each object in the dataset displays.

4. The eigenvalues are sorted in descending order. The eigenvector with the largest eigenvalue is the direction along which the dataset has the maximum variance. Theoretically, each eigenvector represents a principal component. However, usually few eigenvectors with the largest eigenvalues explain most variance in the data and are therefore chosen as principal components for further evaluation.

5. The dataset is projected onto the selected principal components.

For the dataset randomly generated around 3 centers here, which consists of 300 objects described by 3 variables (x, y, z), that means that first, the average of each variable is calculated and the data centered around those averages. A visualization of this is shown in Fig. 5.8. Only two variables of the dataset are plotted, namely the

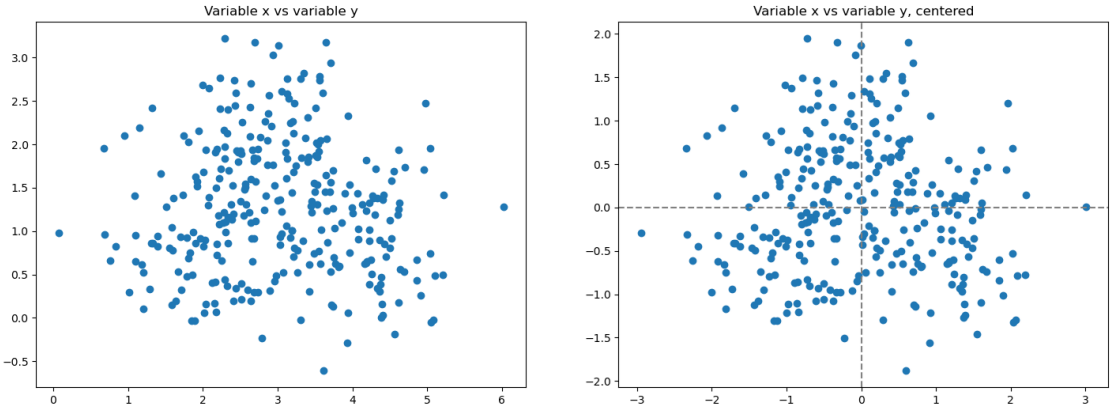

Figure 5.8: Centering of the data for PCA. The data for the first two variables (x and y) is shown. On the left, the values for x and y are plotted against each other. The data is centered by computing the mean of each variable and setting this mean as the center of the data, as shown on the right. For simplicity, this is visualized for two variables only.

values for the coordinates x and y. This calculation is performed for each variable in a dataset.

A pairwise covariance is then computed. The centered values for each pair of variables are multiplied. For the variable pair x and y, a histogram of the resulting values is shown on the left side of Fig. 5.9. For each combination of variables, the pairwise product is calculated and averaged. The resulting values are the covariances. The covariances are arranged into a square matrix in which each row and column corresponds to a variable, so that each element represents the averaged pairwise product of the variables in the respective column and row. This matrix is the covariance matrix, which quantifies the covariance between the selected values, as shown on the right side of Fig. 5.9 for the variables in the generated dataset. In summary, the covariance s_{xy} between the variables x and y for n objects is calculated via eq. 5.1 [148]

$$s_{xy} := \frac{1}{n} \sum_{i=1}^{n} (x_i - \bar{x}) \cdot (y_i - \bar{y}) \tag{5.1}$$

The covariance matrix is then decomposed into its eigenvalues and eigenvectors. The eigenvectors define the direction of a principal component, whereas the eigenvalues represent the variance explained by each principal component. Each principal component is a linear combination of the original variables, weighted by the corresponding eigenvector coefficients. These weighted coefficients are often referred to as loadings. The principal components are then sorted in descending order, which is shown in Fig. 5.10 for all three variables (x, y, and z).

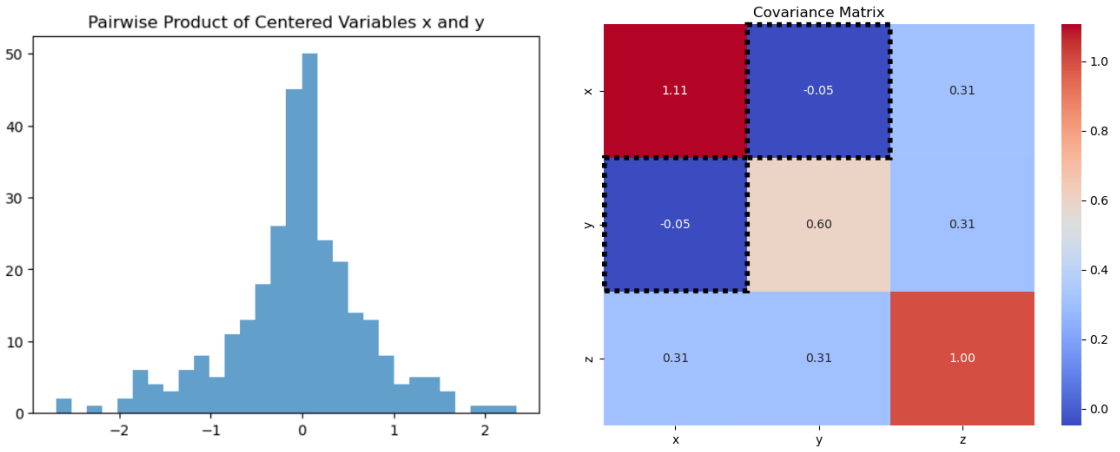

Figure 5.9: Generation of the covariance matrix of the generated dataset. On the left, a histogram of the pairwise product of the first two centered variables, x and y, is shown. On the right, the covariance matrix of the dataset is shown. The average values of the pairwise product of variables x and y, as shown in the histogram, are marked with a black dotted line in the covariance matrix. The color scale represents the values of the covariance between each pair of variables.

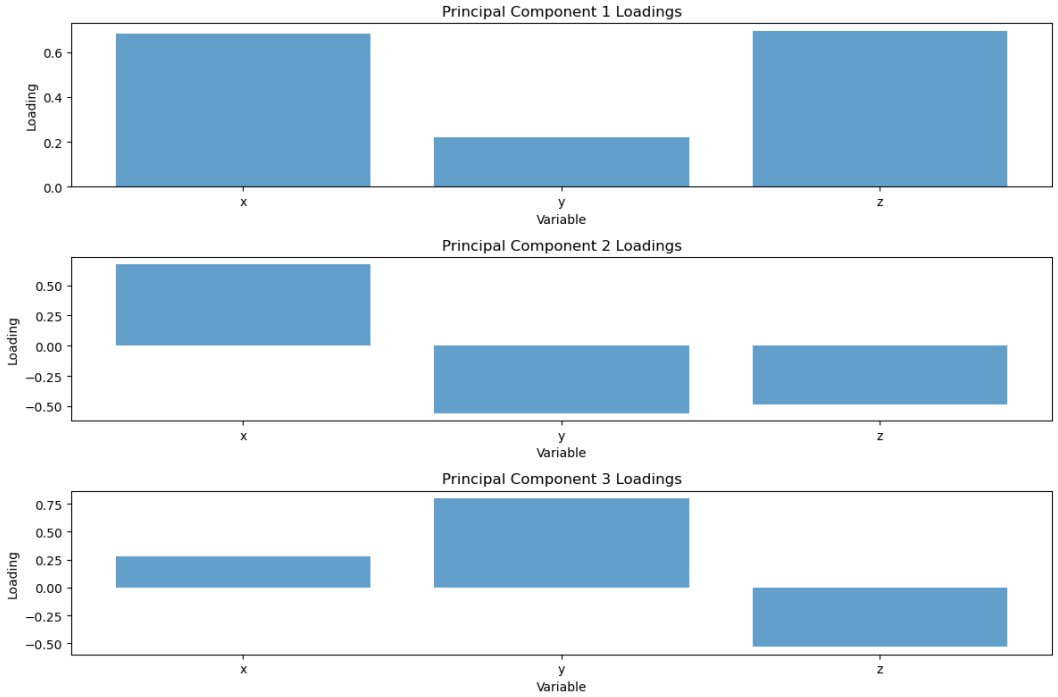

Figure 5.10: PCA loadings of the generated dataset.

As the number of principal components computed equals that of the number of variables in a dataset, one typically aims to minimize the number of principal components while still maintaining a high rate of overall explained variance to decrease the complexity without loss of information. In exploratory data analysis, this is achieved by a *scree plot*. Here, the total variance explained by the principal components is plotted in

descending order. The number of principal components which to retain is determined by the *elbow criterion*, a point in the plot where the slope is observed to decrease. This means that principal components after this point do not add a relevant amount of explained variance in the dataset and are not used for further evaluation. For the generated dataset here, which contains only three variables, the scree plot shown in Fig. 5.11 is close to a line, so all principal components determined by the PCA should be used for any further evaluations.

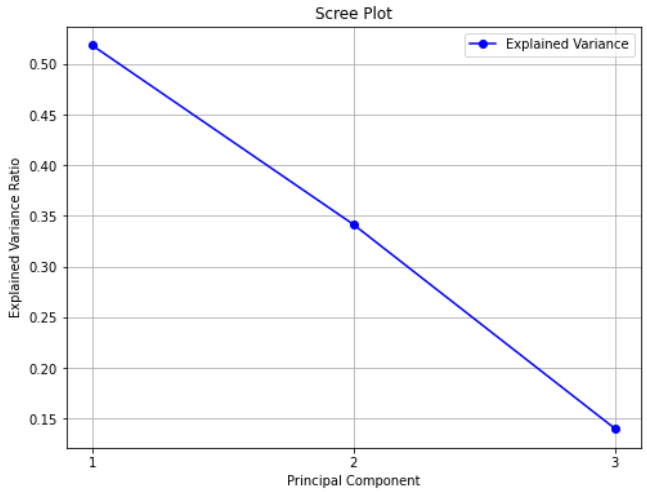

Figure 5.11: Scree plot of the explained variance ratio of the principal components determined for the generated dataset.

Finally, the dataset is projected onto the selected principal components, i.e. the objects are plotted on the new area projected by two principal components, as shown in Fig. 5.12. Typically, the component which explains less variance is plotted against the one which explains more variance. This means that a distance in points along the axis of principal component 1 shown here represents a bigger variance in the dataset than along the axis of principal component 2.

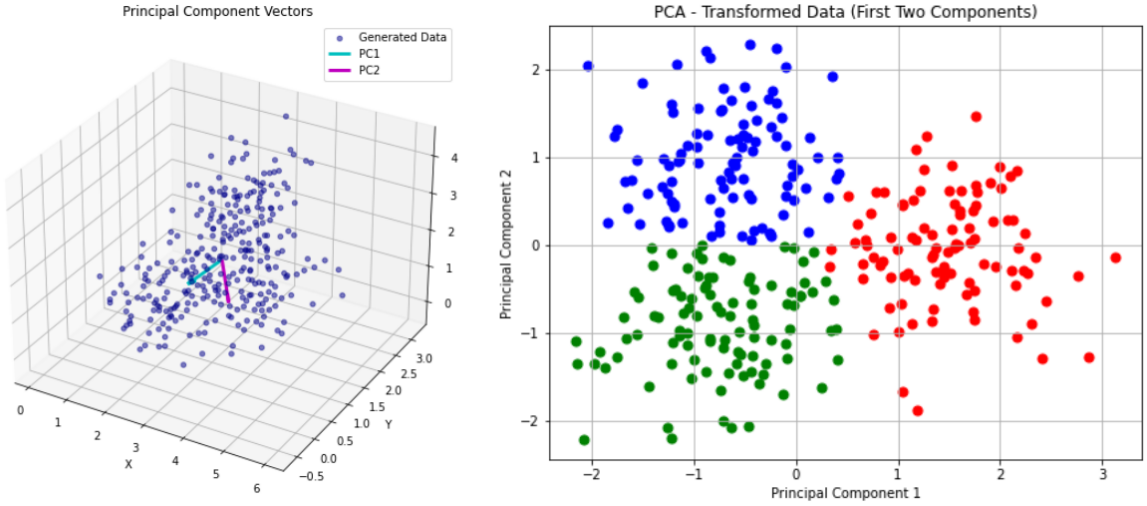

Figure 5.12: Results of the PCA decomposition of the generated dataset. The unit vectors representing the first two principal components (PC1 and PC2), which are projected in the dataset (left), form the area the dataset is projected on (right).

Now, PCA will be applied to the exemplary FSRM dataset for fibers of nylon and polyester in water evaluated in the above Section 5.3.1. To better demonstrate PCA's capabilities of dimension reduction, five variables will be used for the evaluation. The chosen variables are the Raman signals at the wavenumbers 1614 cm^{-1}, 2843 cm^{-1}, and 3133 cm^{-1}, as described above. Additionally, the Raman bands at 1287 cm^{-1} (CO-O stretching observed in polyester) and 2001 cm^{-1} (no band expected) are taken into account. The first two components calculated via PCA are plotted against each other on the left side of Fig. 5.13. On the right, the explained variance ratio for the five principal components calculated is shown as a scree plot. Here, the "elbow" is discernible. Components 3 to 5 form an almost horizontal line, therefore components 4 and 5 do not add significantly to the explanation of the dataset's variance. Three components suffice for the reduction of dimensionality. If PCA was to be used as a form of pre-evaluation, this can also hint at the number of clusters to be used for other algorithmic evaluations, like FCM.

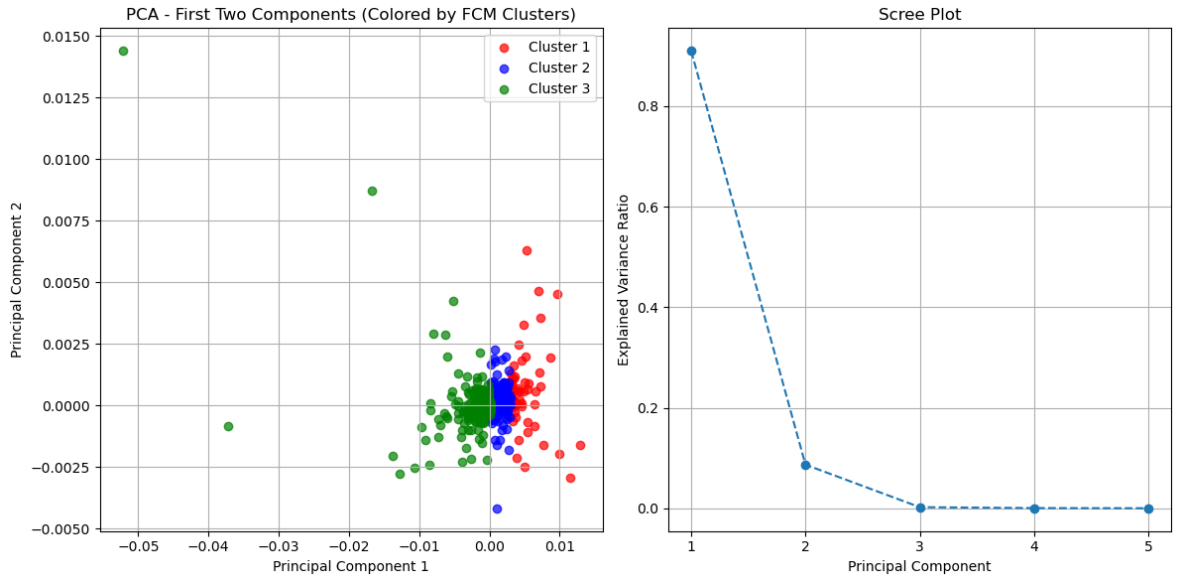

Figure 5.13: Results of the PCA of the FSRM dataset of nylon and polyester fibers in water. On the left, the projection of the dataset onto the first two variables is shown for every 20^{th} data point. On the right, the scree plot shows the variance explained by each principal component. An "elbow" at PC3 suggests that 3 principal components suffice for a description of the dataset without loss of relevant information, as additional principal components do not add significantly to the overall explanation of variance in the dataset.

The loadings of all variables on the respective principal components are represented in Fig. 5.14. Here, it will be stressed again that the loadings do not directly represent Raman signals. Each principal component is a linear combination of the signals at the respective Raman shifts and each observation, i.e. each spectrum, is, in turn, a linear combination of the principal components. Thus, negative values are expected for some

loadings. Positions with a high value of such a principal component denote the absence of the respective variable, for example of the OH stretching Raman band in regions within a fiber that did not absorb water.

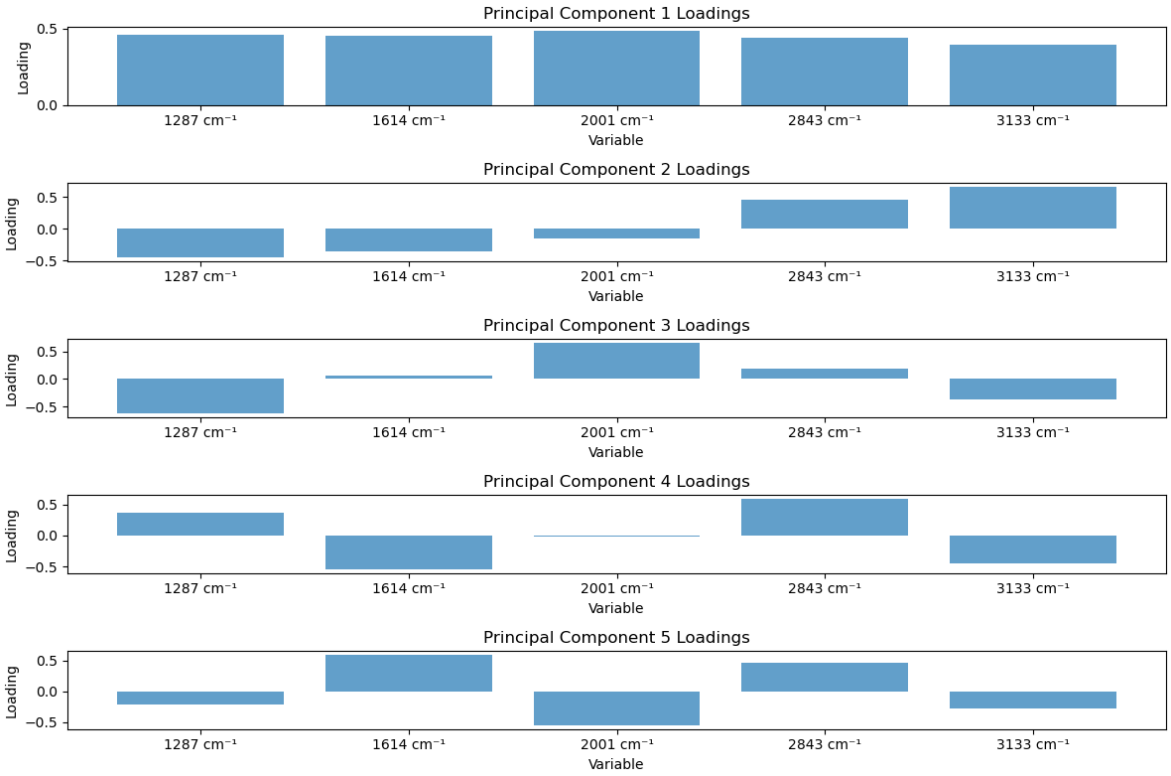

Figure 5.14: Loadings of the variables to the principal components determined for the FSRM dataset of nylon and polyester fibers in water.

6 FSRM Analysis of Microplastics – Results and Discussion

6.1 Comparison of FSRM Raman Spectra with Conventional Raman Spectra

As previously explained in Section 4.2.1, one advantage of SRS spectroscopy is that the spectra achieved are comparable to the ones observed by spontaneous Raman scattering. PMMA beads are frequently used as a standard to demonstrate and test Raman microscopical setups [106, 149, 150] and were chosen to mimic MP samples. Therefore, the results will first be discussed for this sample. During previous projects involving the FSRM, Raman bands at low wavenumbers expected from spontaneous spectra were not observed in FSRM spectra. For example, this was the case for PMMA [151]. An uncorrected spontaneous FT Raman spectrum of PMMA, recorded in approximately five minutes, and an FSRM spectrum, recorded within 10 ms and extracted from a Raman map, are compared in Fig. 6.1.

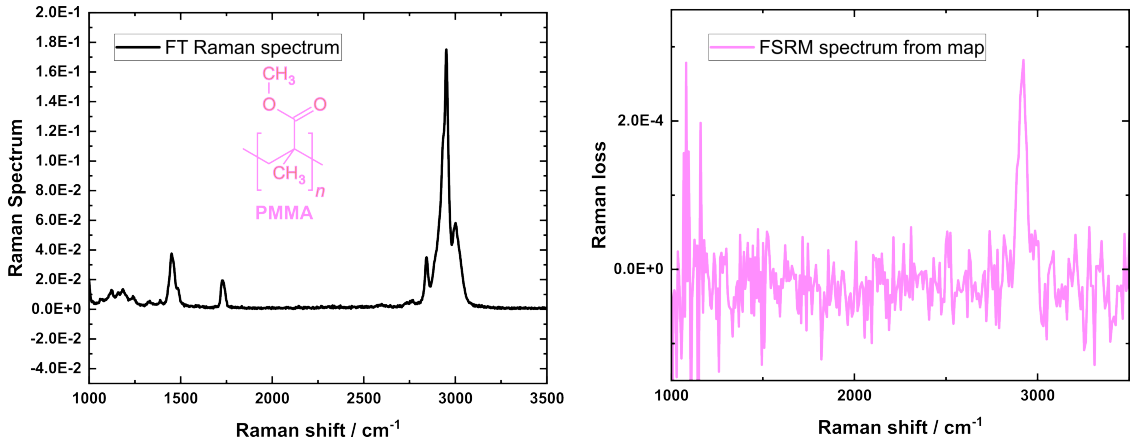

Figure 6.1: Comparison of uncorrected spontaneous Raman (left) and FSRM spectra (right) of PMMA. Acquisition of spontaneous spectra typically required around 5 minutes. The FSRM spectrum was extracted from a single pixel in an FSRM map, recorded with 10 ms acquisition time.

The changes of detection sensitivity for different wavenumbers of the Ge-detector employed in the FT-Raman spectrometer has not been considered in the above spectrum. By dividing the spectrum by the respective quantum efficiency, this can be accounted for. A given reference function for the spectral responsivity of the detector at 25°C [128] is employed for calculation of the quantum efficiency (cf. Fig. 4.4). During the measurement, the detector temperature was roughly 18°C. Here, no reference spectra for correction of the spectral responsivity were recorded before the measurement,

so the function applied is an approximation of the actual spectral responsivity.

The different frequency dependencies of spontaneous and stimulated Raman scattering were already discussed in Section 4.2.3. The effect of the different detection frequencies on the spectra can be corrected by dividing the Raman signal of the spontaneous spectrum by ω_S^3 and the stimulated spectrum by ω_{Probe}, as is apparent from equations 4.6 and 4.7. Both spontaneous and stimulated spectra also depend on the frequency of excitation. As this is a constant factor, it does not need to be considered here because a normalization of the spectra renders it irrelevant. An exemplary calculation for the correction of spectra is given in Section 4.2.3.

The stimulated Raman spectrum further depends on the spectral width of the Raman pump employed. The broader the pump, the broader and lower the Raman band in the stimulated spectrum. Therefore, the spontaneous Raman spectrum needs to be convoluted with the spectrum of the pump. A Gaussian fit of the pump spectrum was used for the convolution.

For PMMA, a comparison of the spontaneous spectrum converted in this manner with the frequency corrected FSRM spectrum with 10 ms acquisition time shown in 6.1, as well as a longer acquisition time of 1 s to achieve a higher SNR, is shown in Fig. 6.2. All spectra were normalized for the highest Raman band, the CH stretching band at 2950 cm^{-1}. The converted spectra were corrected such that the maximum of the CH stretching band are at 2950 cm^{-1}, as observed in the uncorrected spontaneous spectrum. Slight misalignments in the beam path of the FSRM detection were sometimes observed to result in the positions of Raman bands being shifted from the expected positions according to literature.

It is apparent that the noise observed in the wavenumber range below 2000 cm^{-1} in the 10 ms acquisition FSRM spectrum exceeds the signal levels expected from the spontaneous spectrum. In the spectrum with longer averaging of 1 s, the expected Raman bands can be observed, albeit being lower than expected relative to the CH stretching band. The Raman signal with one maximum observed at 977 cm^{-1} in the converted spectrum as well as the FSRM spectrum displays two maxima in the uncorrected spontaneous spectrum. This is an example of the dependence of the spectral resolution on the width of the pump light, as the convolution performed reduces the spectral resolution.

The relative Raman signals of the bands observed for PMMA in the frequency-corrected FSRM spectrum recorded within 1 s and the converted spontaneous spectrum are listed in Table 1. As the spectra were normalized for the CH stretching Raman band observed at 2950 cm^{-1} in the uncorrected spontaneous spectrum, the ratios are compared to that of this band. For most Raman bands, the relative signals are comparable for the

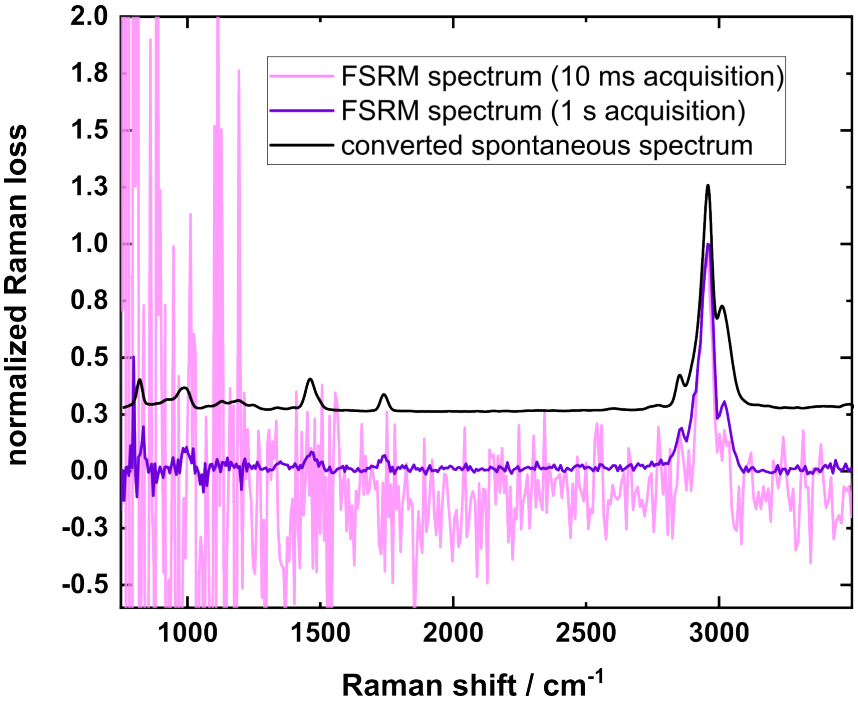

Figure 6.2: Comparison of converted spontaneous and frequency-corrected FSRM spectra of PMMA. All spectra were normalized for the CH stretching vibration at 2950 cm^{-1}.

corrected FSRM and converted spontaneous spectrum, supporting that FSRM spectra are comparable to spontaneous ones upon suitable correction. The Raman signal at 1450 cm^{-1}, however, is significantly higher in the converted spontaneous spectrum relative to the corrected FSRM spectrum. As described in Section 4.2.3, the anisotropy of a band can affect the measured SRS signal. The more depolarized a Raman band, the lower the signal in SRS, as two polarized pulses are employed here. The depolarization ratio of the band at 1450 cm^{-1} is high with a value of $\rho \approx 0.751$ compared to the Raman band at 1730 cm^{-1} with $\rho \approx 0.155$ [152], which might explain the perceived relative difference.

Table 1: Raman band positions and relative Raman signals of converted spontaneous Raman and frequency-corrected FSRM spectra of PMMA.

Raman band position [cm^{-1}]	relative Raman signal FSRM	relative Raman signal spontaneous
813	0.196	0.145
977	0.106	0.109
1450	0.085	0.147
1730	0.070	0.079
2842	0.190	0.165
2951	1.000	1.000
3001	0.307	0.469

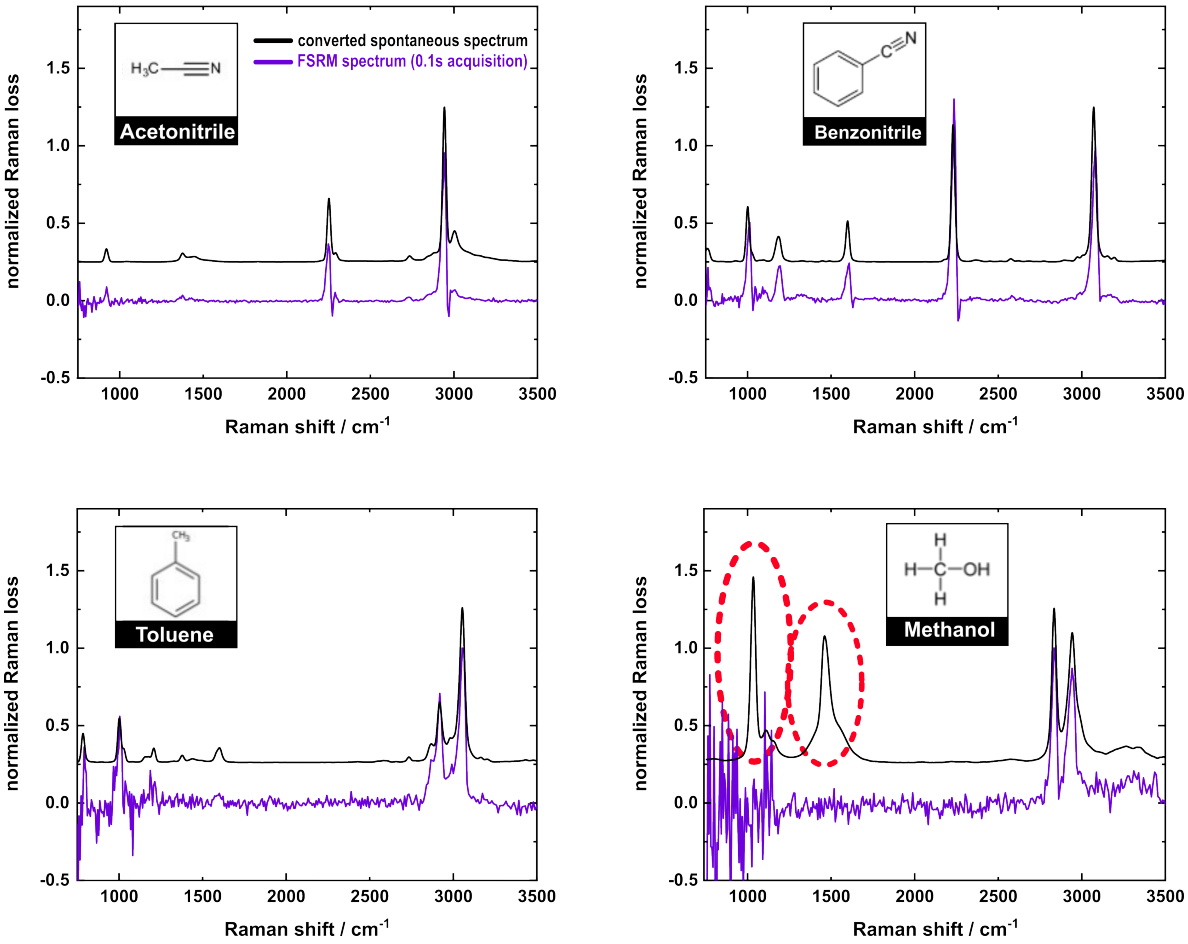

Figure 6.3: Comparison of converted spontaneous Raman and frequency-corrected FSRM spectra of selected solvents. The spectra were normalized for the CH stretching band. FSRM spectra were acquired within 0.1 s.

To further explore the comparison of FSRM spectra with spontaneous ones, additional measurements were conducted employing solvents which exhibit Raman bands in different spectral regions. The solvents chosen were acetonitrile, benzonitrile, toluene, and methanol. The spectra were frequency-corrected and converted as described above and are shown in Fig. 6.3. All spectra were normalized for the CH stretching Raman band. The acquisition time of 1 s for FSRM spectra shown here is 10 times longer than usually applied in the FSRM Raman maps to achieve a higher SNR. Small deviations from the expected band positions were observed in FSRM, which can be caused by the actual maximum of a Raman band being observed in a position between two pixels of the detector or by slightly shifted incoupling of the Raman probe beam into the detector, which will shift the Raman band position to the next detector pixel, accordingly. To this end, the band positions were overlapped by matching the positions of the CH stretching Raman bands observed in FSRM to the ones observed in the spontaneous

spectrum. Band positions were observed to match relative to the CH stretching bands. The Raman active modes associated with the Raman bands observed in the spectra shown in Fig. 6.3 are summarized in Table 2, together with a comparison of the Raman signals relative to the CH stretching Raman bands.

For acetonitrile, benzonitrile and toluene, all Raman bands expected from the spontaneous spectrum are also observed in the FSRM spectrum. Narrow Raman bands observed in the unconverted spontaneous spectrum which are close to each other appear to coalesce as a consequence of the convolution with the Raman pump spectrum. For benzonitrile, this is observed for bands located at 991 cm^{-1}, 1001 cm^{-1}, and 1027 cm^{-1}, as well as 1163 cm^{-1}, 1187 cm^{-1}, and 1193 cm^{-1}. For toluene, this is observed for the bands located at 1004 cm^{-1} and 1032 cm^{-1}, 1155 cm^{-1}, 1180 cm^{-1}, and 1211 cm^{-1}, 1586 cm^{-1} and 1605 cm^{-1}, as well as 2981 cm^{-1} and 3003 cm^{-1}. As expected, for the corresponding bands in FSRM, only one band is observed as well. Bands not observed in the FSRM spectrum have a low relative signal in the spontaneous spectrum and are most likely below noise level.

The relative Raman signals are also comparable for both methods in most cases. Deviations are mostly observed for Raman bands which have a higher depolarization ratio ρ than other bands, i.e. the band is highly unpolarized, resulting in a lower relative signal in FSRM. In the relevant spectral library [129], ρ is defined in such a way that it lies in the range $0 \leq \rho < 6/7$. In the case of acetonitrile, the Raman bands observed at 2943 cm^{-1} and 920 cm^{-1} were reported to be highly polarized with $\rho = 0.05$ or less [129]. The relative intensities are comparable, similar to other strongly polarized bands at 2253 cm^{-1} ($\rho < 0.1$) and 2293 cm^{-1} ($\rho = 0.2$) [129]. For a Raman band with a higher depolarization ratio at 1375 ($\rho = 0.5$) [129], the relative signal observed in FSRM is approximately half of that observed in spontaneous Raman. Similarly, for benzonitrile, the relative signals are comparable for strongly polarized or moderately unpolarized Raman bands at 1002 cm^{-1} ($\rho = 0.05$ for 991 cm^{-1} band and $\rho < 0.1$ for 1026 cm^{-1} band), 1187 cm^{-1} ($\rho = 0.3$ for 1192 cm^{-1} band), and 3072 cm^{-1} ($\rho = 0.3$) [129], with the highly polarized band at 1002 cm^{-1} showing a slightly larger relative signal in FSRM than in the spontaneous spectrum. For a stronger degree of depolarization, a larger difference in the relative signal is observed, which is the case for the band at 1600 cm^{-1} ($\rho = 0.8$) [129]. The band observed at 2232 cm^{-1} ($\rho = 0.4$) [129] is disproportionately large in FSRM compared to spontaneous Raman, which is contrary to expectation from the depolarization ratio. As explained above in Section 4.2.3, a reference function of the spectral responsivity at 25°C was applied, which is the closest available to approximately 18°C which were recorded during the measurement. Deviations between the actual responsivity as well as a difference in temperature might explain the observed difference in relative

Table 2: Raman band assignments for selected solvents and comparison between relative signals observed in frequency-corrected FSRM and converted spontaneous spectra. The stated values are centers of the maxima observed in the converted spontaneous Raman spectra. Raman bands in parentheses refer to separate bands observed in the unconverted spontaneous spectrum but not in the converted spontaneous or FSRM spectrum.

Sample	Raman band [cm^{-1}]	Band assignment	Relative signal FSRM	Relative signal spont.
acetonitrile [153, 154]	920	CC stretching	0.088	0.085
	1043	CH_3rocking	–	0.004
	1375	sym. CH bending	0.035	0.058
	1447	anti-sym. CH bending	–	0.036
	2253	CN stretching	0.365	0.411
	2293	CH bending and CC stretching	0.053	0.060
	2734	CH stretching overtone	0.022	0.040
	2943	sym. CH stretching	1.000	1.000
	3003	anti-sym. CH stretching	0.069	0.201
benzonitrile [155]	1002 (991, 1001, 1027)	CC ring	0.505	0.357
	1187 (1163, 1187, 1193)	CH bending	0.223	0.165
	1600	C=C stretching	0.242	0.264
	2232	CN stretching	1.301	0.886
	2577	combination	0.032	0.021
	3072	CH stretching	1.000	1.000
toluene [156, 157]	787	CC bending	0.361	0.188
	1003 (1004, 1032)	CC bending	0.560	0.287
	1158 (shoulder)	CH bending	0.210	0.038
	1209 (1155, 1180, 1211)	CH bending	–	0.093
	1379	CH_3 bending	–	0.047
	1602 (1586, 1605)	CC stretching	0.062	0.095
	2736	combination/overtone	–	0.036
	2870	combination/overtone	0.278	0.121
	2919	sym. CH_3 stretching	0.708	0.398
	2982 (2981, 3003)	anti-sym CH_3 stretching	0.161	0.160
	3055	arom. ring CH stretching	1.000	1.000
methanol [158]	1035	C-O stretching	–	1.202
	1109 and 1157	CH rocking	–	0.213
	1462	CH bending	–	0.822
	2835	sym. CH stretching	1.000	1.000
	2942	anti-sym. CH stretching	0.870	0.842

signal. For toluene, the relative signal observed in FSRM is larger than that observed in the converted spontaneous spectrum for the highly polarized bands at 1003 cm^{-1} ($\rho < 0.05$ for both 1004 cm^{-1} and 1032 cm^{-1} bands), 1209 cm^{-1} ($\rho < 0.05$) – of which the band observed in FSRM at 1158 cm^{-1} is a shoulder –, and 2919 cm^{-1} ($\rho < 0.1$) [129]. In this case, the aromatic CH stretching vibration at 3055 cm^{-1} for which the spectrum was normalized is moderately depolarized ($\rho = 0.3$) [129], which can explain the stronger effect observed compared to other solvents discussed above. The moderately depolarized Raman band at 1379 cm^{-1} ($\rho = 0.3$) [129] is likely not observed in FSRM because it is below the noise limit. The strongly unpolarized Raman band at 1602 cm^{-1} ($\rho = 0.8$) [129] is considerably lower in the FSRM spectrum than in the spontaneous spectrum.

An important finding of the above measurements and evaluations is that all Raman bands expected from the converted Raman spectrum are observed in the frequency-corrected FSRM spectrum in a similar ratio to the CH stretching Raman band for acetonitrile, benzonitrile and toluene. Raman bands at lower wavenumbers, supposedly not observed in earlier measurements, were therefore below the noise level due to the chosen acquisition times for fast mapping.

However, for methanol, the low-wavenumber Raman bands for C-O stretching at 1035 cm^{-1}, CH_3 rocking at 1109 cm^{-1} and 1157 cm^{-1}, and CH_3 bending at 1462 [158] are not observed in the FSRM spectrum. Both bands should be significantly larger or comparable to that of the CH stretching vibration according to the converted spontaneous spectrum.

The following depolarization ratios have been reported for the respective Raman bands observed in methanol: 1034 cm^{-1}: 0.2, 1112 cm^{-1}: 0.5, 1450 cm^{-1}: 0.7, 2835 cm^{-1}: 0.05, 2944 cm^{-1}: 0.1 [129]. The bands which are observed in the FSRM spectrum are strongly polarized with values near 0, whereas the missing bands are more depolarized. However, for example the band expected at 1034 cm^{-1} has a ρ comparable to that of the CH stretching band, which is visible. A lower Raman signal relative to the strongly polarized bands could be explained by the higher depolarization ratio but even a highly depolarized band would be expected to appear in the FSRM spectrum, as is the case for the other solvents discussed. It was not tested within the course of this thesis which effect rotating the relative polarizations of Raman pump and probe by 90° has on the FSRM spectrum of Methanol. Further measurements should be done in this regard.

One possible explanation which was tested was a temporal chirp of the Raman probe employed. The result of a temporal chirp would be that some frequencies of it arrive at a later time, leading to some frequencies not being properly matched with those of the probe light upon arrival at the sample. Negative "wings" observed at the side of the

narrow Raman bands for acetonitrile and benzonitrile are an indicator for a temporal overlap which is not perfectly aligned, a known effect in stimulated Raman [159]. If this was the cause of the missing Raman band in the FSRM spectrum, the bands would be visible in the spectrum at a different delay of the Raman probe relative to the pump. For benzonitrile, for example, a shift in the Raman bands is observed when scanning through different positions of the delay stage. The separate spectra can be depicted in a contour plot, as shown in Fig. 6.4.

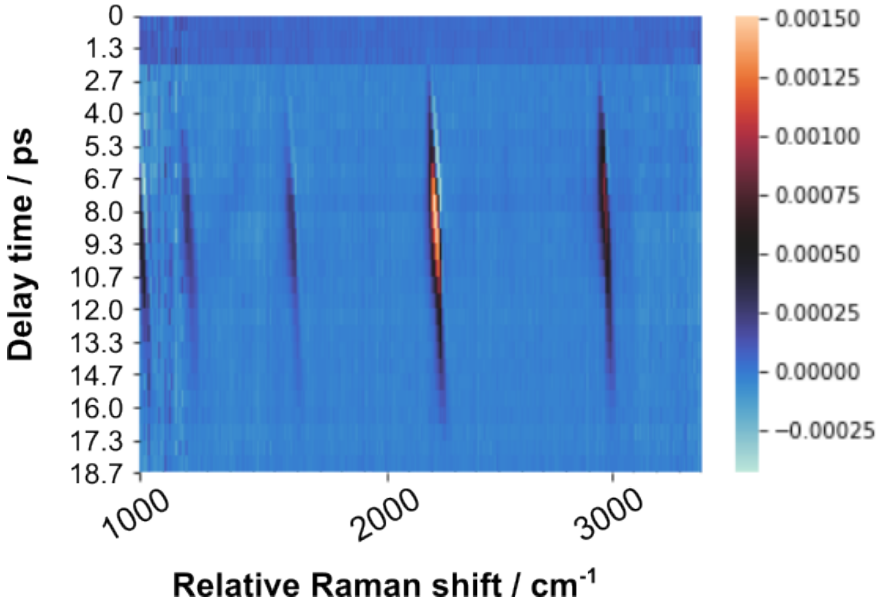

Figure 6.4: Contour plot of FSRM spectra of benzonitrile for different delays of the Raman probe. The delay mirrors were moved between measurements and the resulting time delay with respect to the first measurement is reported on the vertical axis. The FSRM signal for the respective Raman shifts of spectra recorded at different delays of the Raman probe are color-coded.

If the beam path of the Raman probe is correctly aligned, all frequencies of the probe light are expected to arrive at the same time. Changing the delay time of the probe is expected to change only the Raman signal. However, the tilting observed in the position of the Raman bands suggests that different frequencies of the probe arrive at different times, thus shifting the Raman band depending on the delay. As can be seen in the case of benzonitrile, a chirp in the probe slightly affects the signal position but all Raman bands are still visible at the same delay time at which the CH stretching band is maximized. The same was tested for a methanol sample (cf. Fig. 6.5) and no additional Raman bands were observed for different delays. The alignment of the probe and its resulting chirp are therefore not the cause of the low-wavenumber Raman bands of methanol not being observed with FSRM.

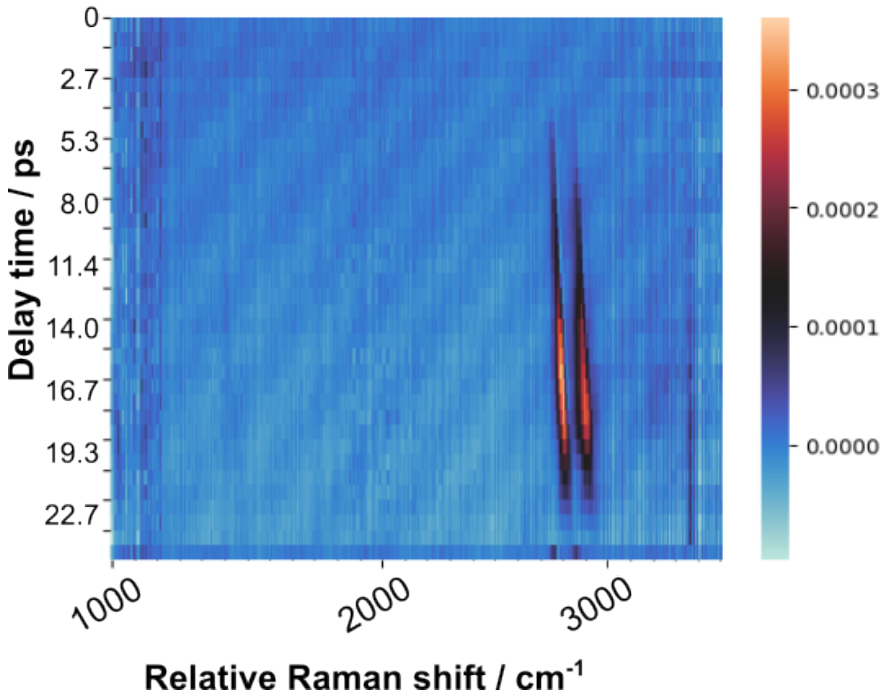

Figure 6.5: Contour plot of FSRM spectra of methanol for different delays of the Raman probe. The delay mirrors were moved between measurements and the resulting time delay with respect to the first measurement is reported on the vertical axis. The FSRM signal for the respective Raman shifts of spectra recorded at different delays of the Raman probe are color-coded.

During alignments for the measurements of methanol samples, a baseline effect was observed. When defocusing the two microscope objectives by lifting the top one, as schematically shown on the left side of Fig. 6.6, the baseline would tilt and shift downward, as can be seen in the Raman spectra on the right side of Fig. 6.6. The Raman bands in the CH stretching region are still observed. The observed shift was stronger the higher the focusing objective was lifted. This is not typically observed for other samples, liquids and solids alike. Usually, a defocusing only results in a decrease of signal while the noise increases. This suggests that another non-linear effect is present in the case of methanol. Additional to the baseline shift, a Raman band appears with a maximum at 1107 cm^{-1}. The Raman bands not observed under good focusing conditions, however, are expected at 1035 cm^{-1} and 1452 cm^{-1}. The Raman probe laser displays a peak in that region. Combined with the downward shift of the baseline, which indicates that photons of the same energy as that of the Raman probe are generated, this suggests a possible enhancement of the probe light. Another possible cause for the additional band observed can be a contribution from the cover glass, as borosilicate glass exhibits Raman bands in a similar region (950 and 1090 cm^{-1}) [160]. By elevating the focusing objective, the focus of the Raman pump and probe might partially be shifted into the cover slip. Still, this additional band has not been observed

in other samples; thus, a contribution from glass cannot be asserted.

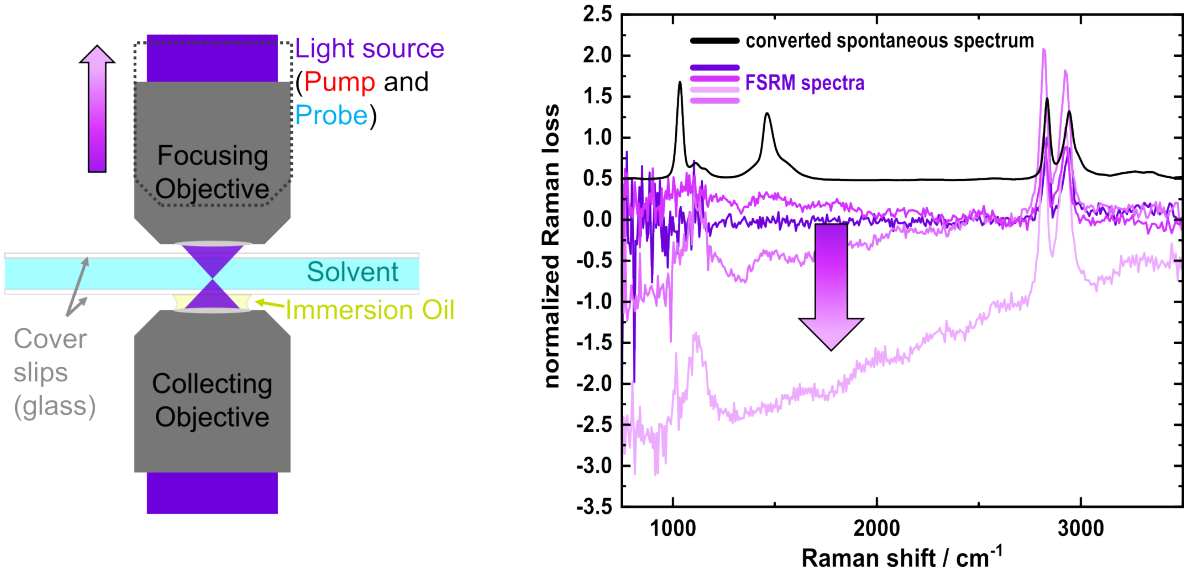

Figure 6.6: Focus shift resulting in baseline shifts of methanol spectra. The arrow denotes the upwards movement of the top objective which results in a baseline shift in the corresponding spectra on the right (shown by the hue turning lighter).

Cross-phase modulation (XPM) might also explain the effect. XPM describes that the pump modulates the refractive index in the medium, which, in turn, causes a shift in the probe [161]. XPM has been shown to distort (femtosecond) SRS, with the effect increasing with the non-linear refractive index n_2 of the medium [162]. However, methanol features the lowest n_2 of the solvents investigated [163]. Thus, the effect observed cannot solely be explained by XPM.

Further alcohols, ethanol and 2-propanol, were also examined for this effect, as the lower-wavenumber bands for C-O stretching and CH_3 bending are expected for other alcohols as well. The baseline-shift including a Raman band observed at 1107 cm^{-1} was observed as well, as shown in Fig. 6.7. The effect appeared to be less pronounced for ethanol and 2-propanol than for methanol. For both of these alcohols, upon misalignment of the focus, an additional Raman band could be observed at 1417 cm^{-1} where the CH_3 bending vibration is expected. However, the band observed was very weak. For 2-propanol, it was slightly larger than for ethanol. Further alcohols were not tested here, so a trend cannot be deduced. During the course of this thesis, the effect could not be explained. Future projects should investigate the effect under conditions with less tightly focused light, for example by employing FSRS spectroscopy. Furthermore, the effect of the chain length on the lack of low-wavenumber Raman bands and the baseline shift observed upon misalignment of the focus should be further investigated.

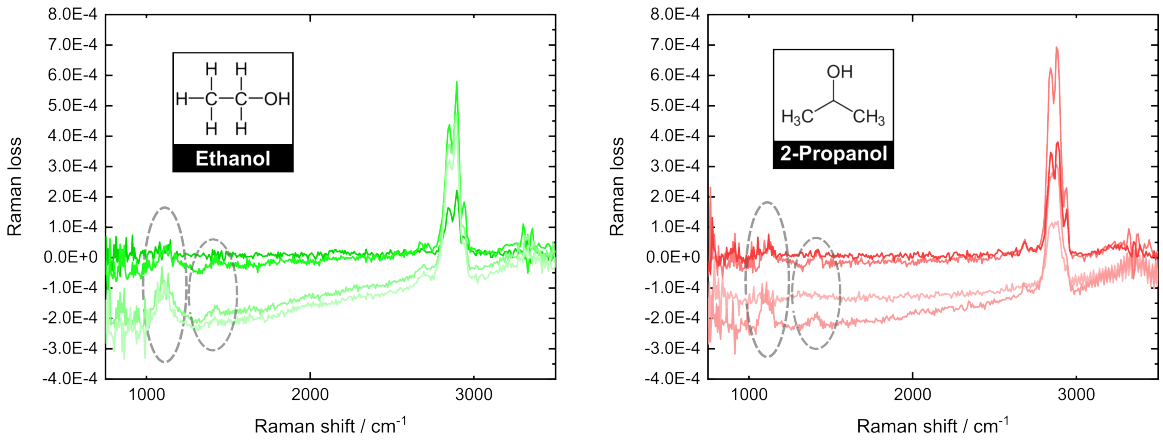

Figure 6.7: Baseline shift observed in ethanol (left) and 2-propanol (right) upon shifting the focus.

6.2 Analysis of Selected Samples

6.2.1 Microbeads in Water

The process of sample preparation, measurement and evaluation of MP samples was first tested using standards. PMMA and PS microbeads were used to simulate the preparation of MP samples in water, as they are commonly applied to test micro-spectroscopical techniques [97, 164, 165] and have been applied to demonstrate FSRM before [31]. The microbeads samples were prepared as explained in Section 5.1. To this end, microbeads dispersed in water needed to be filtered. The number of steps added to the sample preparation process should be as low as possible to avoid loss of sample as well as introduction of contamination of MP present in the laboratory environment. Therefore, samples should be measured directly on the filter. A filter based on aluminum oxide (0.2 µm, Whatman®, Anodisc®, 25 mm Ø) was chosen because the material does not feature disturbing Raman signals in the relevant wavenumber regions [87]. The filter also needs to be transmissive for FSRM measurements, which is the case when it is wet. The wet filter, which was placed on a microscope slide, was therefore covered with a second, round glass slide and the edges sealed with clear nail polish to prevent evaporation. For acquisition of the FSRM maps, the prepared sample was placed on the sample stage and a region of interest determined visually by using the microscope objectives as conventional light objectives: A white light lamp was placed on the focusing objective and a white paper placed under the collecting objective, onto which the transmitted image of the sample region was projected. When a region of interest was determined, the lamp was removed, the light of the probe laser first focused visually and finally, the beam paths aligned for maximum Raman loss and minimum noise. Before an FSRM map could be recorded, the probe light was reduced

to avoid saturation of the detector during the measurement. A reference spectrum with the Raman pump laser blocked was recorded for calculation of the FSRM spectra. This aims at reducing detector-related noise patterns, which will be briefly explored in Section 7.3.2. When the acquisition of a Raman map was started, the piezo stage on which the sample was mounted moved in a zigzag pattern to cover the whole area selected, which was usually 200 x 200 µm. The movement of the stage was continuous and its speed adjusted to the chosen number of FSRM spectra to be averaged per spatial pixel. Most measurements shown here feature an acquisition time of 10 ms per pixel, equal to 100 FSRM spectra averaged. FSRM imaging of PMMA and PS beads in water with corresponding spectra extracted from the map is shown in Fig. 6.8. The 200 x 200 µm map with a step size of 1 µm was recorded with an acquisition time of 10 ms. The measurement took around 7 minutes.

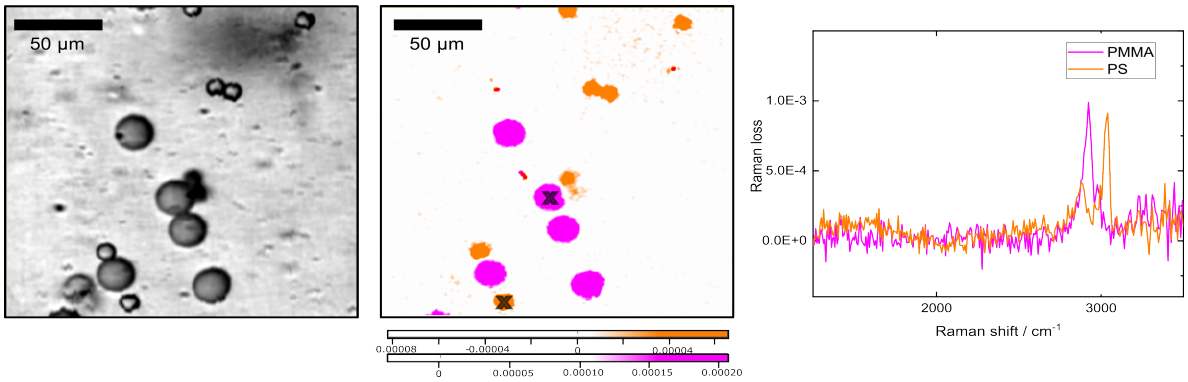

Figure 6.8: FSRM imaging of PMMA and PS beads. On the left, a map of the probe beam transmission is shown. In the middle, a false-color image is shown. On the right, two spectra of marked positions in PMMA and PS beads are shown. A univariate analysis was used to generate the false-color image. The descriptors applied were baseline-subtracted integrals of the Raman bands in the regions 2771 cm^{-1} - 3050 cm^{-1} (PMMA) and 2967 cm^{-1} - 3088 cm^{-1} (PS).

The transmission map on the left side of Fig. 6.8 features spherical beads of different sizes, making PMMA and PS distinguishable. In total, 5 larger PMMA beads and 6 smaller PS beads seem to be located in the focal plane, as their edges do not appear blurry and the centers of the spheres feature higher transmission for the probe. Further beads seem to be located above or below the focal plane and can only be distinguished as blurry approximately round shapes with low transmission. In the Raman map in the middle, the baseline-subtracted integrals in the regions 2771 cm^{-1} - 3050 cm^{-1} for PMMA and 2967 cm^{-1} - 3088 cm^{-1} for PS are color-coded. 5 beads of PMMA and 7 beads of PS can be observed. Some additional spots which do not resemble the shape of the other particles and do not correlate with a particle observed in the transmission map are seen. One more PS bead can be distinguished than in the transmission map, the particle is located in the center of the map and is attributed to one seemingly

out-of-focus particle. In the transmission map, the PMMA beads have an approximate size of 23.2 µm and the PS beads of 9.9 µm. In the FSRM map, the diameter of the PMMA beads appears slightly smaller than in the transmission map with a diameter around 18.7 µm. The values are within range of the particle sizes stated to be 21.83 µm for PMMA and 11 µm for PS. The varying sizes might be attributed to the varying thickness of the beads along the beam direction due to the spherical shape.

However, the most apparent difference between the transmission and Raman map is the shape of the particles. In the FSRM map, the PS particles in particular do not appear as spherical and the edges are not smooth like observed in the transmission map. The different sizes and shapes can have several reasons. One reason are refractive index mismatches between the beads and surrounding water, which distort the recorded Raman spectra [166]. Furthermore, due to the three-dimensional shape, the edges of the particles might not lie in the focal plane, thus causing different scattering for the probe beam, which in turn is not detected adequately anymore after passing through these regions. In the transmission map, it is apparent that the transmission is generally lower towards the edges of the particles, decreasing the SNR as well as the integral in the selected wavenumber regions. Another reason for the irregular shapes can be a low FSRM Raman signal in the relevant regions. At the time of measurement, instabilities in the probe laser intensity and necessary repairs in the fiber amplifier have frequently resulted in low signal levels. Consequently, small changes in the diffraction during the scan of a sample region caused an unproportionately large increase in noise compared to the overall signal levels. This strongly affects the integrated Raman signal, and thus the shape of the particle appears more distorted. Furthermore, the color-coding is adjusted manually and might distort the particle size and shape.

The acquisition time for the above measurement was 10 ms per pixel, which is longer than the potentially possible 0.1 ms that were demonstrated before [131]. The longer acquisition time was chosen for two reasons. One reason, as described above, were low signal levels caused by technical difficulties at the time of the measurement. Longer averaging times lead to a higher SNR and, consequently, better imaging. The second reason were movements of the particles observed during the scan if lower acquisition times were chosen. The sample was placed on a stage which continuously moved during the acquisition of one Raman map. The lower the chosen acquisition time, the faster the movement of the stage. As the particles were suspended in water here and not fixed, they could move inside the matrix. In evaluations after a fast scan, the beads were not observed as spherical anymore but as lines along the axis of movement.

6.2.2 Consumer Goods: Facial Scrub

Consumer goods, specifically facial scrub, were chosen as the next step for MP sample preparation. The type of MP contained was known as it was stated on the list of ingredients and the concentration was also expected to be high because the particles are typically used as abrasive agents in the scrub. Furthermore, consumer goods could be easily acquired and the MP was expected to be easily extracted. The first facial scrub acquired, *ULTRA Rapid Action Akut* from Clearasil, contained polyethylene (PE) as the ingredient with the second highest concentration after water. The clear scrub contained two types of particles visible by eye: dark blue beads and white or transparent smaller particles. A small portion of the scrub was applied to an object slide for first FSRM test measurements. The blue beads were found to not be transparent so could not be evaluated. For the smaller transparent particles, however, this was possible. An FSRM map of such a particle recorded with a step size of 0.5 µm and an acquisition time of 10 ms/pixel was recorded within 49 mins and is shown in Fig. 6.9.

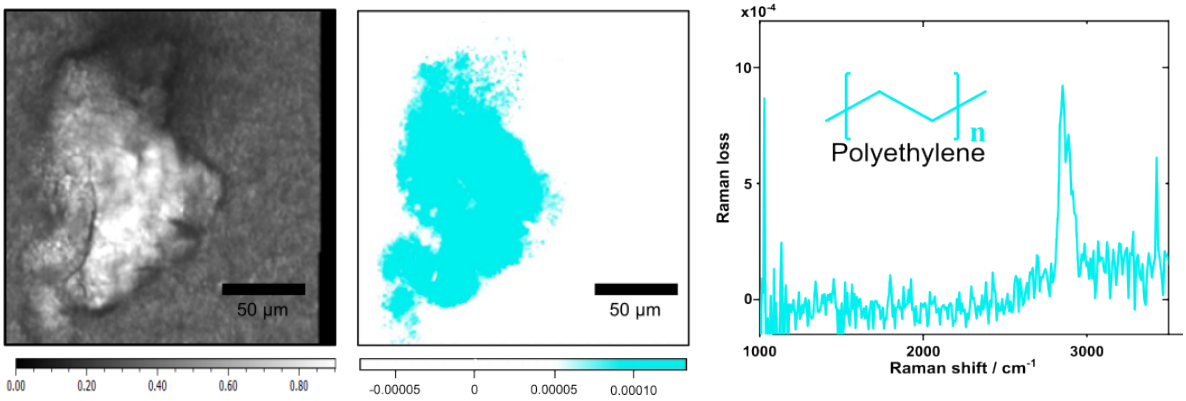

Figure 6.9: FSRM imaging of a polyethylene particle acquired from facial scrub with the corresponding Raman spectrum from one pixel of the map. On the left, a map of the Raman probe's transmission is shown. In the middle, the baseline subtracted area from 2781 - 2964 cm^{-1} of the CH stretching Raman band is color-coded. On the right, a single spectrum extracted from one pixel within the map is shown. The 200 x 200 µm map with 0.5 µm step size and 10 ms/pixel was recorded within approximately 49 minutes.

Both the probe transmission map on the left and the Raman map in the middle, color-coded for the descriptor defined as the baseline subtracted area from 2781 - 2964 cm^{-1}, reveal a particle with an irregular shape. The particle is roughly 103 µm wide and 154 µm long. Presumably, particles in a facial scrub of such shape enhance the exfoliating properties. The Raman spectra recorded, of which one is shown on the right side of Fig. 6.9, corroborate the assumption that the particle consists of polyethylene, the second most abundant ingredient of the facial scrub.

After initial test measurements, the particles were supposed to be extracted from

the scrub. During the course of a Bachelor's thesis, the extraction of particles from the matrix was unsuccessful [134]. Due to these difficulties and to achieve a broader range of primary MP samples measured, it was tried to acquire different sample. However, it was found that consumer products containing MP have become rare. Whether this is due to increased consumer awareness, policy changes, or both, cannot be said. Only one additional facial scrub containing MP particles was commercially available, namely *Sébium Gel Gommant Exfoliating Purifying Gel Peelinggel für aknöse Gesichtshaut* from Bioderma. The Bioderma product contained cellulose acetate, a bio-based polymer. This facial scrub could easily be filtered after being suspended in water. A corresponding FSRM map is shown in Fig. 6.10. The transmission as well as the Raman signal of the particle was found to be low prior to the measurement, therefore an acquisition time of 1 s/pixel was chosen, resulting in a total time of 71 minutes for measurement of the 200 x 200 µm map with 1 µm steps.

The transmission map on the left side of Fig. 6.10 shows a particle which also displays an uneven shape. The particle is approximately 126 µm wide. Its length cannot be determined, as it is only partially positioned within the scanned region. As the transmission of the Raman probe was low in many regions of the particle, a Raman signal in the CH stretching region at 2922 cm^{-1} can only be observed in a small region of the particle. Therefore, in the false-color Raman map, there is a large area which appears white, as it is neither attributed to the Raman band of cellulose acetate, nor to that of the surrounding water.

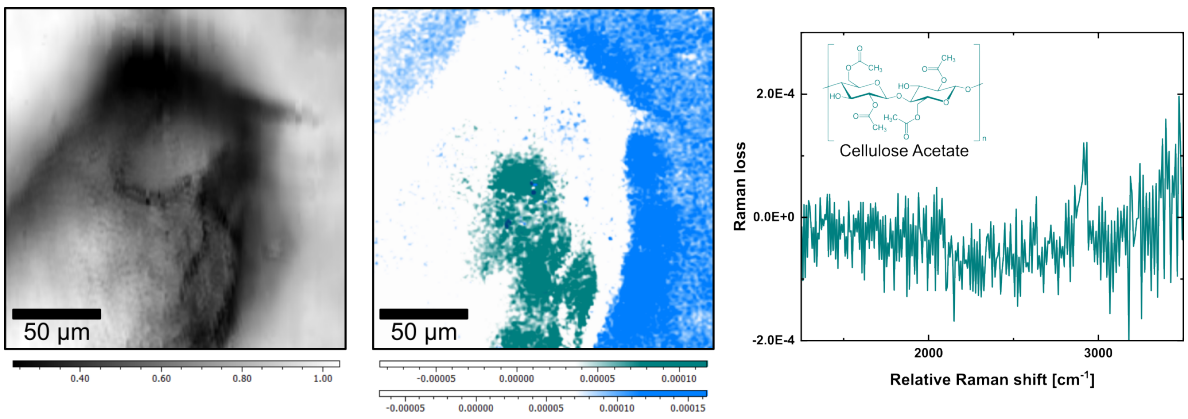

Figure 6.10: FSRM imaging of a filtered cellulose acetate particle acquired from facial scrub. On the left, a map of the total transmission of the Raman probe is shown. In the Raman map in the middle, the Raman signals for cellulose acetate (teal, baseline subtracted Raman signal at 2922 cm^{-1}) and water (blue, baseline subtracted area from 2999 cm^{-1} - 3815 cm^{-1}) are color-coded. A corresponding spectrum of the particle extracted from a single pixel in the map is shown on the right. The 200 x 200 µm map with 1 µm steps and an averaging time of 1 s/pixel was recorded within approximately 71 minutes.

6.2.3 Textile Fibers in Water

As primary MP in consumer goods have become unavailable during the course of this thesis, which fortunately decreases some sources of output into the environment, the focus of this thesis was shifted towards secondary MP. More specifically, microfibers, as they make up a considerable amount of MP found in environmental samples (cf. Section 2.2.1) and fabrics made of synthetic fibers are easily available.

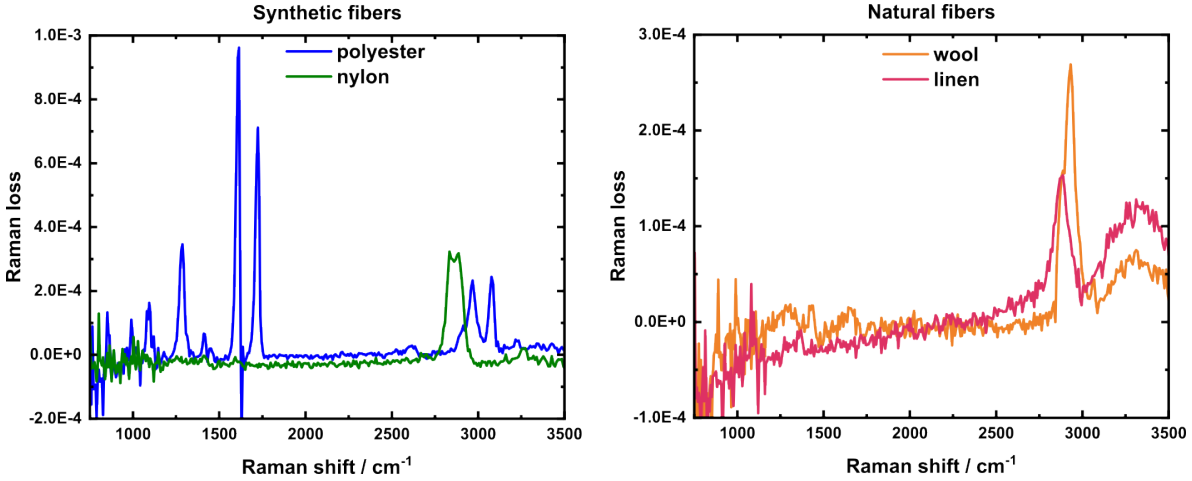

Figure 6.11: FSRM spectra of fiber samples. The reference spectra were recorded in a single position of the respective fiber samples and the FSRM aligned for maximum Raman loss. The acquisition time for each spectrum was 1 s. Adapted from ref. [121].

After showing before that, in principle, MPs can be analyzed via FSRM, here it will now be shown that a qualitative distinction between particles is possible without necessary prior knowledge about the particles' composition. Specifically, both natural and synthetic fibers will be evaluated. For this purpose, common examples of fabrics were chosen. Polyester and nylon were chosen as samples of synthetic fibers, linen (a plant fiber consisting mainly of cellulose) and wool (an animal fiber) as samples of natural fibers. First, FSRM Raman spectra of each fiber were recorded, which are shown in Fig. 6.11. The single spectra were recorded with an acquisition time of 1 s to achieve lower noise and higher SNR. It is important to note that the polyester and nylon fibers were transmissive for the pump and probe light, therefore spectra could be recorded directly, whereas the natural fibers had to be soaked in water to become adequately transmissive. The spectra of wool and linen therefore display the broad Raman band of water ranging approximately from 3100 cm^{-1} to 3600 cm^{-1} [167]. The Raman bands observed are summarized in Table 3, as well as the Raman active modes associated with the respective bands. If a Raman band's baseline-corrected integral was used as a descriptor for evaluation of recorded FSRM maps, the descriptor's range is also noted. Some Raman bands reported in literature have not been observed here. For linen, these were

positioned at 1341 cm^{-1}, 1334 cm^{-1}, and 1291 cm^{-1} [168, 169]. For wool, a Raman band located at 1460 cm^{-1} [168, 169] is likely masked by other vibrations or below noise limit, comparable to a band associated with NH stretching expected at 3276 cm^{-1}, most likely masked by the broad Raman band associated with OH stretching vibrations of water [169, 170]. Generally, Raman bands at wavenumbers lower than reported in Table 3 were not observed.

Table 3: Raman bands observed in FSRM spectra of fiber samples and their assignment to Raman vibrations as well as the respective descriptors employed in algorithmic evaluations of measurements.

Sample	Raman band [cm^{-1}]	Band assignment	Descriptor [cm^{-1}]
nylon [168, 169]	1410	CH_2 bending	1415 - 1457
	1593	C=O stretching	1579 - 1768
	2834 and 2887	CH stretching	2739 - 3011
	3273	NH stretching of secondary amino group	3254 - 3346
polyester [168, 169, 171]	851	CC stretching	
	990	COC bending	
	1094	CO and CC stretching	
	1179	CC ring stretching	
	1287	CO-O stretching	1244 - 1335
	1410 and 1451	CH_2 bending	
	1614	aromatic CC ring stretching	1561 - 1651
	1723	C=O stretching	1678 - 1765
	2895, 2968, and 3077	CH stretching	2932 - 3041
linen [168, 169]	1081 and 1100	sym. and anti-sym. glycosidic ring breathing of COC	1094 - 1160
	1159	CC and CO stretching of the glycosidic ring	
	1382	CH_2 and HCO bending	
	1465	CH_2 bending scissors	
	2887	CH stretching	2754 - 2990
wool [168–170]	1307 and 1515	COO^- and CH_2 bending CH bending	
	1650	C=O and COO^- stretching	1599 - 1699
	2932	CH stretching	2773 - 3013
water [167]	3100 - 3600	OH stretching	3069 - 3307

Samples of the fibers were prepared as described in Section 5.1 and FSRM maps acquired in the same manner as described before in Section 6.2.1. The respective

fabrics were cut into pieces as small as possible and further dissected in water using two spatulas, the resulting liquid shaken and finally filtrated using an aluminum oxide filter (0.2 µm, Whatman®, Anodisc®, 25 mm Ø). The measurements shown here feature an acquisition time of 10 ms per pixel, equal to 100 FSRM spectra averaged.

Application of Statistical Evaluation Methods to Experimental Data

For FSRM maps shown in previous sections, univariate analysis methods were applied using one descriptor for the color-coding, namely the integral of a Raman band. For the fiber samples, clustering algorithms were employed. For these samples, the different methods were applied to further mimic a step in the evaluation of environmental samples contaminated with MP. For samples of known composition, the expected Raman bands can be used as descriptors to visualize the shape and/or concentration of the sample within the scanned area. However, in order to simulate an environmental sample, one has to assume to not know the sample's composition in advance. The advantage of FSRM over SRS microscopy lies in recording full Raman spectral information for each point in the scanned area, the expected Raman signals therefore do not need to be known prior to the measurement. However, the evaluation of the generated FSRM data needs to be adjusted if one does not have any prior knowledge about the constituents of a sample. An automated clustering algorithm like fuzzy c-means (FCM) enables partitioning spectra into a selected number of clusters. The spectra of each cluster can then be averaged, enabling an identification of the respective constituent. Another unknown parameter can be the number of different substances present in the scanned region. A principal component analysis (PCA) can help with this. By evaluating the amount of variance explained by each principal component calculated in PCA, the number of clusters to chose for further evaluation can be determined.

The sample evaluation will first be described in detail for a measurement of nylon fibers in water. A map depicting the Raman probe's transmission for each pixel position is depicted in Fig. 6.12(a). Recording the 200 x 200 µm map with 1 µm spacing and 1 ms acquisition time took approximately 7 mins. The dataset consists of 40 000 spectra. The transmission map shows a fiber placed horizontally in the scanned area lying in the focal plane. On the top left corner, an additional fiber is positioned outside of the focal plane, as the transmission in this region is low, indicated by the black color-coding. Furthermore, the focused fiber has lower transmission on its edges, most likely caused by scattering effects due to the round shape of the fiber. In these regions with low transmission of the Raman probe, high noise and, consequently, low SNR is expected for the respective Raman spectra. The diameter of the fiber derived from the transmission map is approximately 56 µm. This was verified by determining the

diameter of a single nylon thread extracted from the fabric to be 50 µm using a sliding caliper. The results lie within the same range. As the nylon fibers were not observed to disintegrate further during the sample preparation, this was expected.

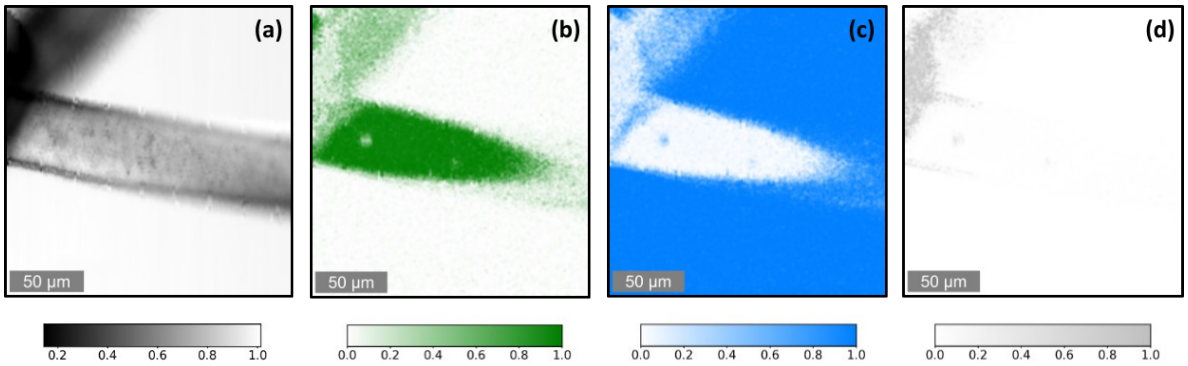

Figure 6.12: FSRM imaging of nylon fibers dispersed in water. (a) The average transmission of the Raman probe is color-coded with white denoting a transmission of 1 and darker shades denoting lower transmission. Membership gradients are color-coded for (b) the nylon cluster (green), (c) the water cluster (blue) and (d) the distortion cluster (grey). The degree of membership ranges between zero (white) and one (full saturation). The 200 x 200 µm maps with 1 µm spatial resolution and an acquisition time of 10 ms/pixel were recorded within approximately 7 minutes. Adapted from ref.[121].

FCM clustering of the spectral data was performed employing three clusters, one for each substance present in the sample (nylon and water) and an additional one to account for regions of high noise. The additional cluster termed "distortion" proved beneficial to the overall quality of most FCM images acquired. Therefore, it was applied for each FCM evaluation to keep consistency in all evaluations. The five descriptors relevant for nylon and water were applied as variables. In the false-color images shown in Fig. 6.12(b)-(d), the degree of membership to the clusters associated with nylon, water, and distortion are color-coded, with higher saturation of the color denoting a higher degree of membership. The FCM images reflect the shape of the nylon fiber expected from the transmission image: A horizontal fiber is distinguished in the middle of the image showing the nylon cluster in Fig. 6.12(b). In the top left corner of said image, the saturation of pixels is lower than in the middle, as this is the second fiber appearing to lie outside of the focal plane in the transmission image. This highlights the sectioning capabilities of the SRS process [133], which is primarily sensitive to material which is located at or near the focal plane (cf. Section 4.3, Fig. 4.10). As a result, the left portion of the nylon fiber appears within the focal region, while the right portion does not. This observation is further supported by the FCM cluster corresponding to water shown in Fig. 6.12(c) appearing to be the negative of the nylon cluster image, which is to be expected, as water surrounded the fiber. Finally, the image of the distortion cluster shown in Fig. 6.12(d) reveals a high degree of membership for spectra in the top left

corner of the scanned region. Here, high noise is expected due to the low transmission of the out-of-focus fiber. However, the nylon and water FCM images differ from the transmission image as the fiber appears to be only partially visible. Pixels on the left side of the fiber show a high saturation, whereas toward the right side of the image, the saturation decreases. The nylon fiber seems to be bent and thus partially be positioned outside of the focal plane, which explains the low degree of membership to the nylon cluster towards the right side of the fiber and the high degree of membership to the water cluster. The transmission image further supports this observation, as the edges of the fiber appear to become more blurry on the right side, suggesting that the particle is not completely within the focal plane. The diameter of the fiber determined using the FCM map is 51 µm and therefore slightly lower than the one determined by the transmission map. Due to the round shape, the edges of the fiber might have been positioned outside of the focal plane during the measurement, explaining the slightly lower diameter.

The spectra within each cluster can be averaged, as shown in Fig. 6.13. The averaged cluster spectra are also the basis for assigning the clusters. The averaged spectrum of the nylon cluster shown in Fig. 6.13(a) displays the same Raman bands as expected from the reference spectrum shown in Fig. 6.11. However, the Raman loss is lower than in the reference spectrum. This has multiple causes. One, the reference spectrum was recorded in a single position for which the conditions were optimized to achieve the highest signal possible. During a map scan, the topography of the fiber lead to different scattering and therefore different focusing conditions, which decreased the signal as focusing can affect the overlap of the Raman pump and probe. Furthermore, regions which are only partially in the focal plane or even outside of it were accounted for in the averaged cluster spectrum as well. These regions show lower signal levels or no signal at all, which decreases the average Raman signal of the cluster spectrum. This also increases the noise level of the averaged spectrum, as it includes spectra of regions with low transmission and high noise which do not feature a Raman band. The noise level is also higher compared to the reference spectrum as the number of averages per spectrum was lower for acquisition of an FSRM map. Moreover, the power of the Raman probe was reduced before the scan to avoid saturation of the detector. For initial alignments, the Raman pump and probe were focused within the fiber, the probe light maximized until almost saturation of the detector and the setup aligned for the highest Raman loss. From the transmission map, it is obvious that the transmission is higher outside of the fiber than inside. Before starting a map scan, the probe light needed to be adjusted to avoid saturation of the detector, resulting in higher noise observed in spectra of the fiber.

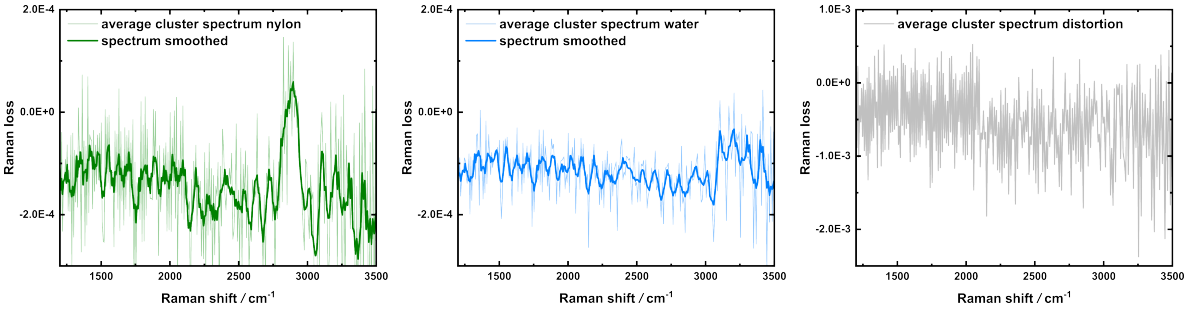

Figure 6.13: Averaged spectra of the FCM clusters of the Raman maps shown in Fig. 6.12. All spectra assigned to one cluster were averaged and these averaged spectra smoothed using a Savitzky Golay filter with a window size of 10 spectral pixels. Adapted from ref. [121].

The overall noise in the averaged spectra is further influenced by fixed pattern noise. This type of noise is caused by the readout mechanism of the detector [132, 172]. Each pixel is connected to the readout electronics via two distinct channels that alternately transfer the generated charge. These two channels differ slightly in their electronic characteristics, thus resulting in small differences in the signal during consecutive readout cycles. As the probe spectrum is detected alternating between the pump being on and off, the corresponding signals are read through different pathways. For long acquisition times or when averaging many individual spectra of a map, this effect cannot be sufficiently compensated for by subtracting the respective baseline, thus contributing a pattern to the overall noise level.

In addition to FCM clustering the FSRM data was also evaluated using PCA. The PCA was based on the same five variables as FCM. Ideally, the whole Raman spectrum would be used for this analysis. However, the software employed requires using pre-defined descriptors. As described in Section 5.3.2, the number of possible principal components is defined by the number of variables in the dataset. For the example of nylon, 5 principal components can therefore be extracted from the dataset of 40 000 objects. The scree plot in Figure 6.14 shows the ratio of explained variance of each principal component. Here, the elbow criterion can be applied to decide on the number of principal

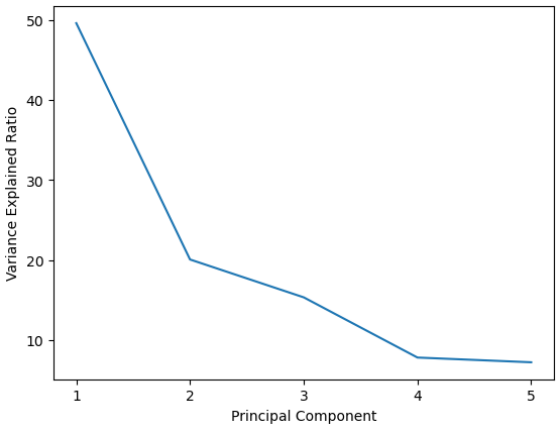

Figure 6.14: Scree plot of the PCA evaluation of the FSRM dataset of nylon fibers in water. In total, five descriptors were used for the PCA, therefore 5 principal components can be computed.

components to use for further evaluation. The slope of the plot appears to flatten out after principal component 4. Consequently, four components should be used to explain the variance in the dataset. However, the elbow criterion is very subjective, as one might also say that PC4 and PC5 should not be used for the evaluation, as explained variance is below 10 % for both.

The projection of the FSRM dataset onto the principal components is shown in Fig. 6.15. Each point in these plots represents one object, i.e. one spectrum. Each point can be selected and linked to a position in the FSRM map.

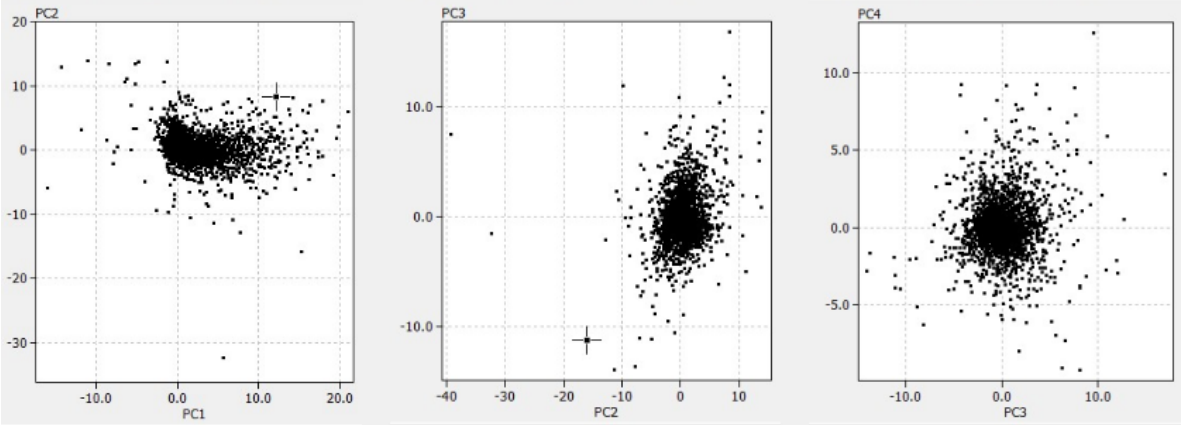

Figure 6.15: Projection of the datapoints in the FSRM dataset of nylon fibers in water onto the principal components. Each point is one object, i.e. one spectrum, of the FSRM dataset. The position within the shown graphs denotes the object's score for the principal components shown. The x-axis always represents the principal component of higher order. Thus, a bigger distance of points along the x-axis denotes a bigger variance between the points than along the y-axis.

The loadings of the descriptors for the different principal components are shown in Fig. 6.16. The descriptors are labeled according to the Raman active modes they represent. Each principal component is a linear combination of these descriptors. Using the loadings and the scores of each principal component for each object, which quantify how much the object projects onto the principal component, the original values of the employed descriptors could be reconstructed employing further mathematical evaluation. If PCA had been applied to every spectral wavenumber, the spectra could be retrieved from these linear combinations. It is important to note that neither the loadings nor the scores represent actual spectra; rather, they are linear combinations of spectral descriptors within the constraints of PCA, where the principal components are orthogonal. The results do not have direct physical meaning, and their interpretation will be carried out here within these limitations. Positive loadings can be described as indicating the contribution of a constituent's presence, while negative values reflect its absence.

All descriptors, except for the CH stretching Raman vibration observed for Nylon,

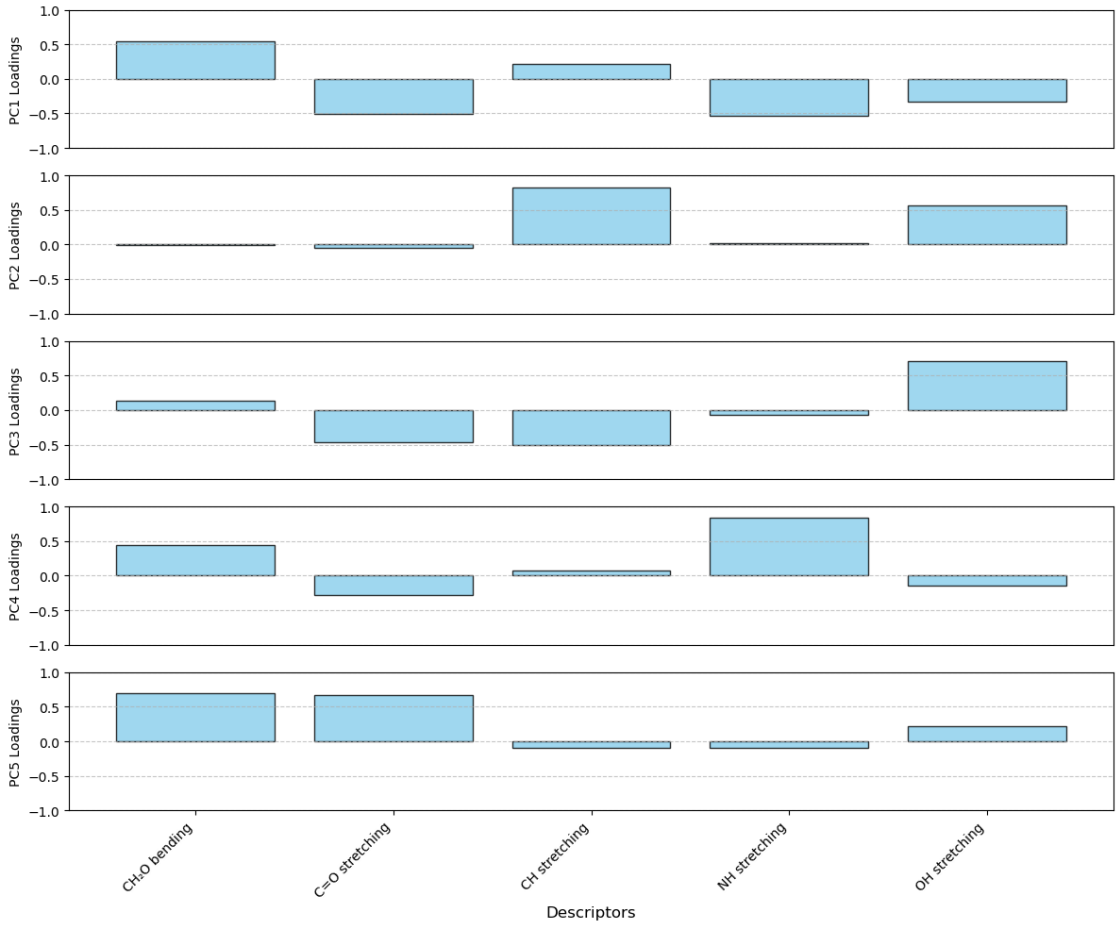

Figure 6.16: Loadings of the descriptors onto each principal component for the PCA evaluation of the FSRM dataset of nylon fibers in water.

appear to be strongly contributing to PC1, positively or negatively. For PC2 the CH stretching descriptor has the highest loading, suggesting that positions within the nylon fiber will be associated with a high score for PC2. The OH stretching descriptor has a high loading on PC3, indicating that regions with a high score for PC3 are most likely water. Again, it is pointed out here that a PC does not describe one spectrum but that it is a linear combination of variables which, in turn, is a factor in a linear combination of all PCs which can be used to retrieve the spectrum found in one object, i.e. pixel of the Raman map.

For each spectrum, the score of each principal component, as shown in Figure 6.15, can be color-coded. This is displayed in Figure 6.17 for the first four principal components. PC1 (Figure 6.17(a)) has the highest scores in regions that were found to display high noise by the FCM clustering. PC2 (Figure 6.17(b)) has high scores in regions which can be assigned to nylon. This is also in line with the highest loading descriptor being the one describing CH stretching. Similarly, PC3 (Figure 6.17(c)) displays the highest

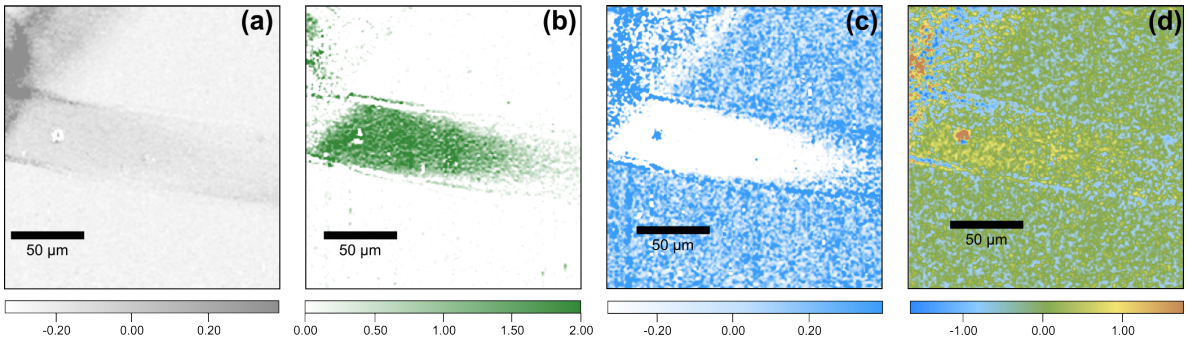

Figure 6.17: Map plots of the PCA scores for the evaluated FSRM measurement of nylon fibers in water for principal components (a) 1, (b) 2, (c) 3, and (d) 4.

scores in regions of the sample assigned to water, in line with the high loading of the OH stretching descriptor. For PC4 (Figure 6.17(d)), no pattern comparable to the FCM evaluation can be distinguished. This is in line with the low variance explained by this principal component. The highest loading descriptors also display low Raman signal, the principal component therefore likely describes a noise pattern observed for those spectral regions.

FCM clustering evaluations of selected fibers

FSRM images of all other types of fibers were recorded and evaluated in the same manner as described above for nylon. The results of the FCM clustering are summarized in Fig. 6.18. The transmission maps and Raman maps displaying the FCM clusters for the respective fibers each display one fiber within the focal plane in the scanned region. The averaged Raman spectra on the right side feature the same characteristic Raman bands as expected from the reference spectra. In the transmission map of the polyester fiber (Fig. 6.18(a)), an additional shape which shows low transmission can be found in the top left corner of the scanned region. Most likely, a second fiber was located there which was positioned above or below the focal plane. This additional particle is also visible in the corresponding Raman image, as particles in that region have a high degree of membership for the distortion cluster. Using the transmission map, the diameter of the polyester fiber can be determined to be 21 µm, whereas it is slightly smaller at 15 µm when determining it using the FCM cluster map. The same effects already discussed for the maps of nylon fibers can cause this difference. In the case of the fibers summarized in Fig. 6.18, the diameters of single threads could not be cross-checked using a sliding caliper. Unlike nylon, the threads of polyester, linen, and wool were wound together from several smaller fibers and the fibers disintegrated further during the sample preparation. Diameters determined before the process were therefore expected to be in a different range, rendering the determination irrelevant.

The size of the linen fiber in Fig. 6.18(b) is 23 µm for the transmission map and 17 µm for the FCM cluster map. The scanned sample region outside of the fiber, which is expected to consist only of water, also shows many pixels with a similarly high degree of membership to the distortion cluster (grey) as for the water cluster (light blue). As the algorithm assigns the clusters automatically, this can happen if the number of clusters chosen is higher than necessary. However, for the sake of consistency, all FSRM measurements were evaluated employing the additional cluster in the FCM algorithm.

The diameter of the wool fiber, shown in Fig. 6.18(c), can be determined as 40 µm using the transmission image and 28 µm using the FCM cluster image. Similar to the FCM cluster map of the linen fiber, the scanned region expected to belong mainly to the water cluster also features a comparably high degree of membership to the distortion cluster distributed evenly over said region.

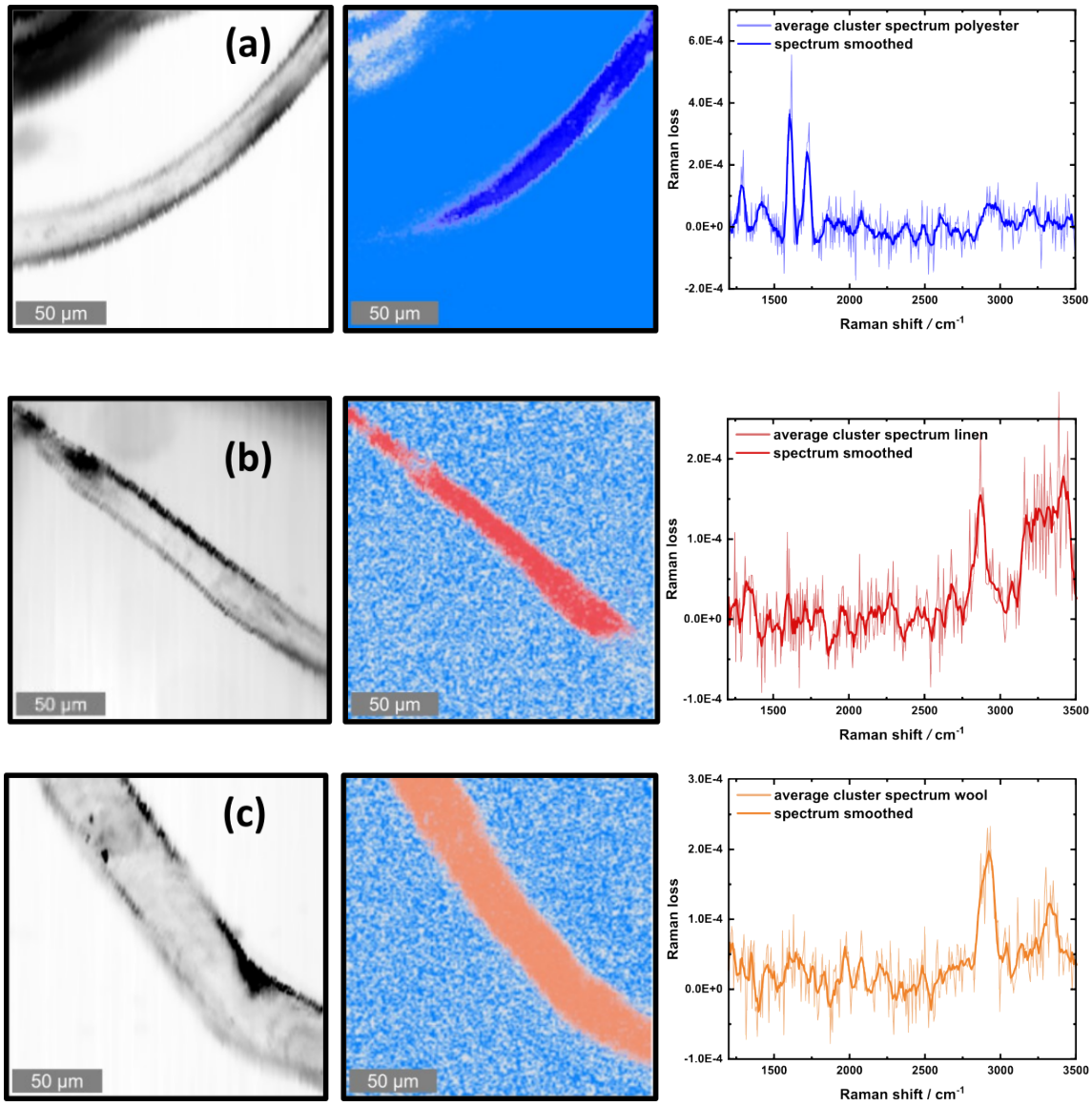

Figure 6.18: FSRM imaging of (a) polyester, (b) linen, and (c) wool fibers dispersed in water. Adapted from ref. [121]. The 200 x 200 µm maps with 1 µm spatial resolution and an acquisition time of 10 ms/pixel were recorded within approximately 7 minutes. On the left, the transmission of the Raman probe is color-coded, with darker shades denoting lower transmission. In the middle, Raman maps color-coded according to the degree of membership to the FCM clusters are shown. All three clusters – fiber, water (light blue), and distortion (grey) – are portrayed in one image. For all clusters, the degree of membership ranges between zero (white) and one (full saturation). On the right, the averaged cluster spectra for the clusters featuring the respective fibers are featured. The averaged spectra were smoothed using a Savitzky Golay filter with a window size of 10 spectral pixels.

PCA evaluation of polyester fibers

Now, the PCA evaluations of the FSRM measurements discussed above will be detailed. The PCA algorithm performed for the measurement of polyester fibers in water employed the five relevant descriptors for polyester and water. The corresponding scree plot, shown in Fig. 6.19, displays an elbow after PC3, suggesting that three principal components suffice for the description of most of the variance observed in the data. Investigation of the loadings of the descriptors shown in Fig. 6.20 suggests that scanned regions within polyester will display a high loading for PC1, as all descriptors belonging to Raman bands of polyester have similarly high positive loadings compared to the descriptor attributed to the OH stretching vibration of water. The water descriptor has the highest loading for PC2, so it is expected that pixels in the sample regions consisting of water will show the highest scores for PC2. In PC3, the values for the loadings of the polyester descriptors are also higher than that of water.

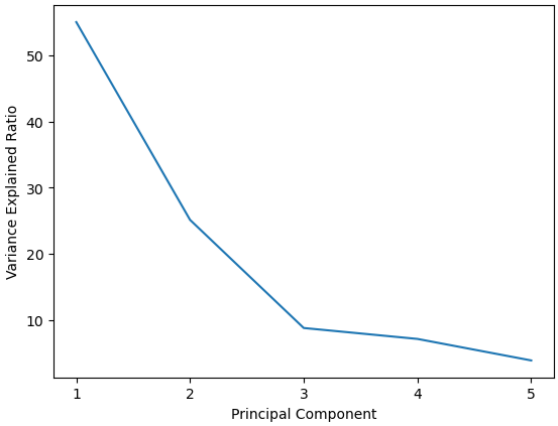

Figure 6.19: Scree plot of the PCA evaluation of the FSRM dataset of polyester fibers in water. In total, five descriptors were used for the PCA, therefore five principal components can be computed.

The corresponding scores of each spectrum for the first three principal components are displayed as color-coded maps in Fig. 6.21. The shape of the fiber matches that found by the FCM clustering algorithm. As expected, the pixels corresponding to the polyester fiber show the highest loadings for PC1 and PC2. Pixels in the sample region where an out-of-focus particle was detected in the transmission and FCM maps display negative scores for PC1, whereas it also displays positive scores similar to the pixels within the fiber for PC3. PC2 has the highest scores for the pixels in the water region of the scanned area.

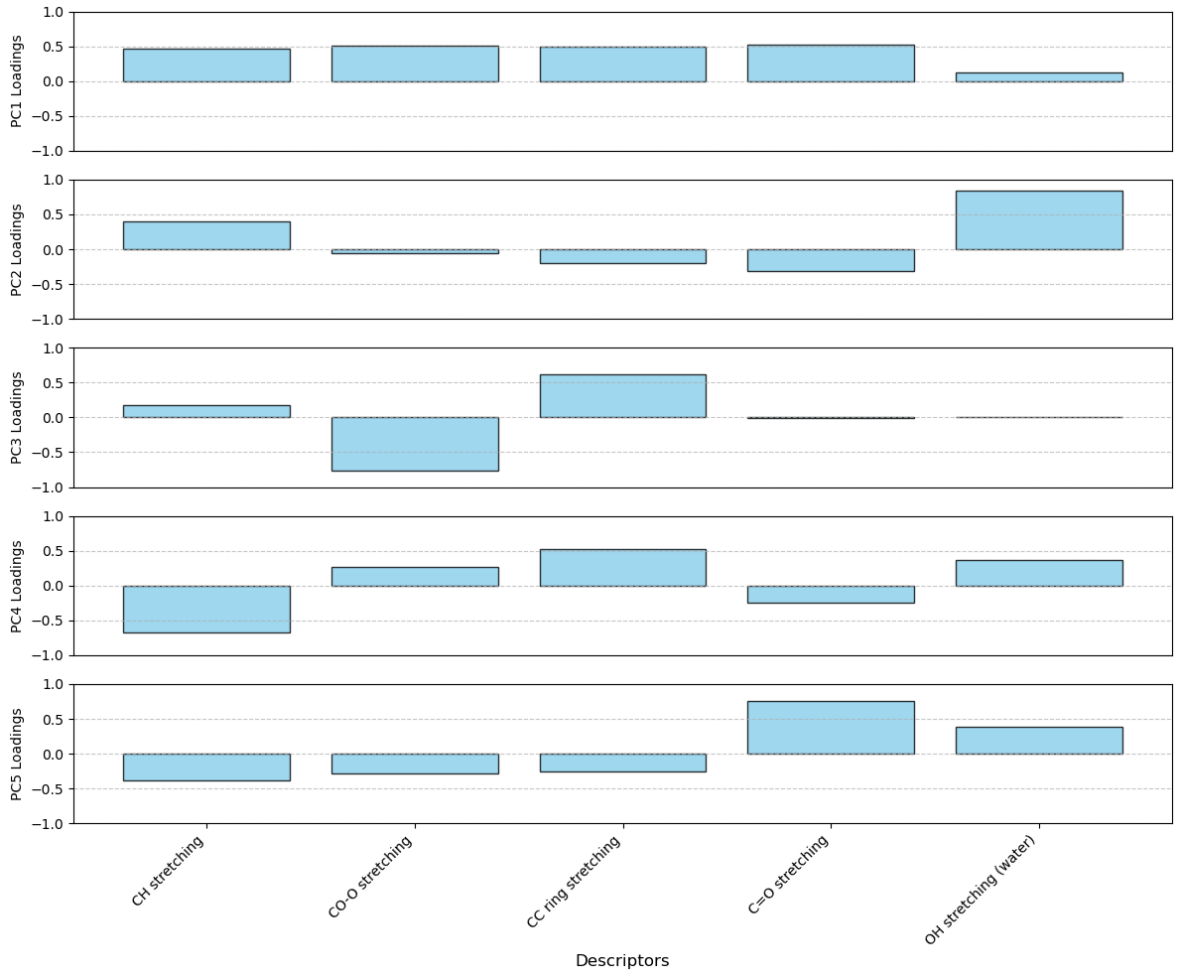

Figure 6.20: Loadings of the descriptors onto each principal component for the PCA evaluation of the FSRM dataset of polyester fibers in water.

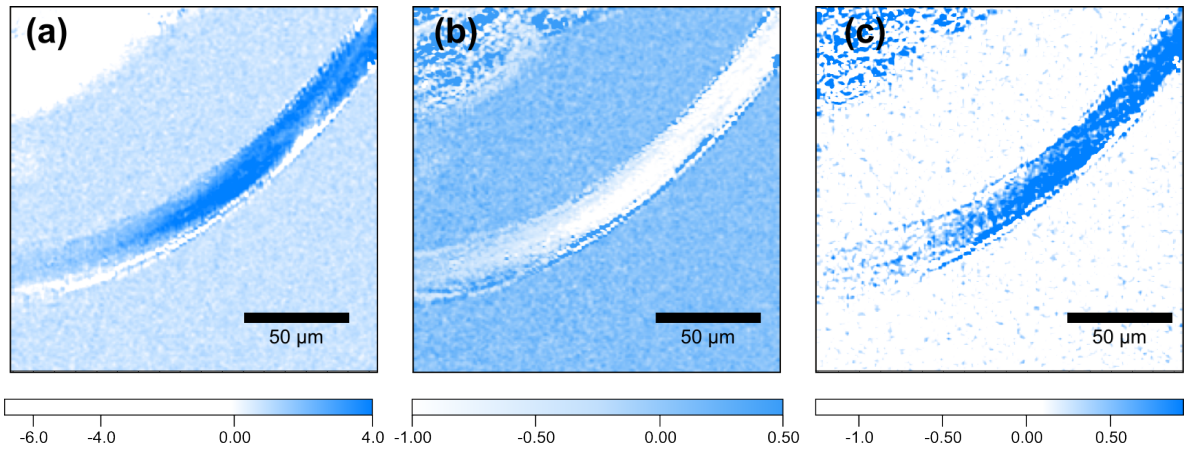

Figure 6.21: Map plots of the PCA scores for the evaluated FSRM measurement of polyester fibers in water for principal components (a) 1, (b) 2, and (c) 3.

PCA evaluation of linen fibers

For the evaluation of the linen measurement, only three descriptors were defined because only two Raman bands can be distinguished in the spectra of linen at the acquisition time of 10 ms/pixel, which was used for the FSRM map. Therefore, only the two descriptors for the Raman bands detected in linen and the one for water were employed in the PCA, resulting in 3 principal components being computed. The scree plot depicted in Fig. 6.22 is almost a straight line, indicating that all principal components should be used for further analysis.

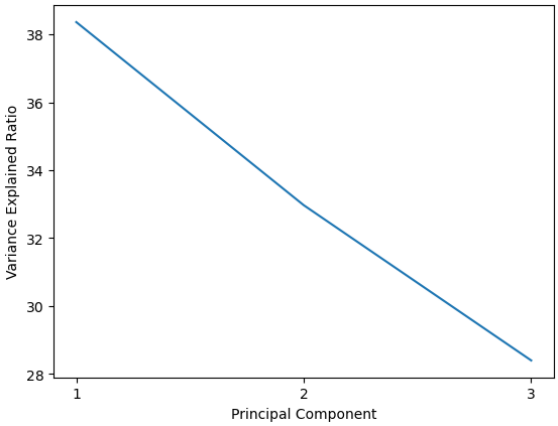

Figure 6.22: Scree plot of the PCA evaluation of the FSRM dataset of linen fibers in water. In total, three descriptors were used for the PCA, therefore three principal components can be computed.

From the loadings of the descriptors onto the principal components shown in Fig. 6.23, a trend can only be distinguished for PC2. Here, the CH stretching vibration observed in linen has the strongest loading. Neither PC1 nor PC2 show a particularly strong loading of the OH stretching band observed in water. The corresponding maps color-coding the PCA scores of each pixel in Fig. 6.24 show the same behavior. Only for PC2 (Fig. 6.24(b)), the shape of the linen fiber can be distinguished. The other two maps do not display a pattern which reflects the transmission or FCM cluster maps discussed earlier. This might be due to the low Raman signal of the glycosidic ring breathing. Even in spectra recorded with an acquisition time of 1 s, the band is only slightly above noise level. During the FSRM scan, for which the acquisition time was 10 times lower, the band is below noise level. The descriptor therefore reflects a noise pattern, resulting in a lower quality of the PCA in this case.

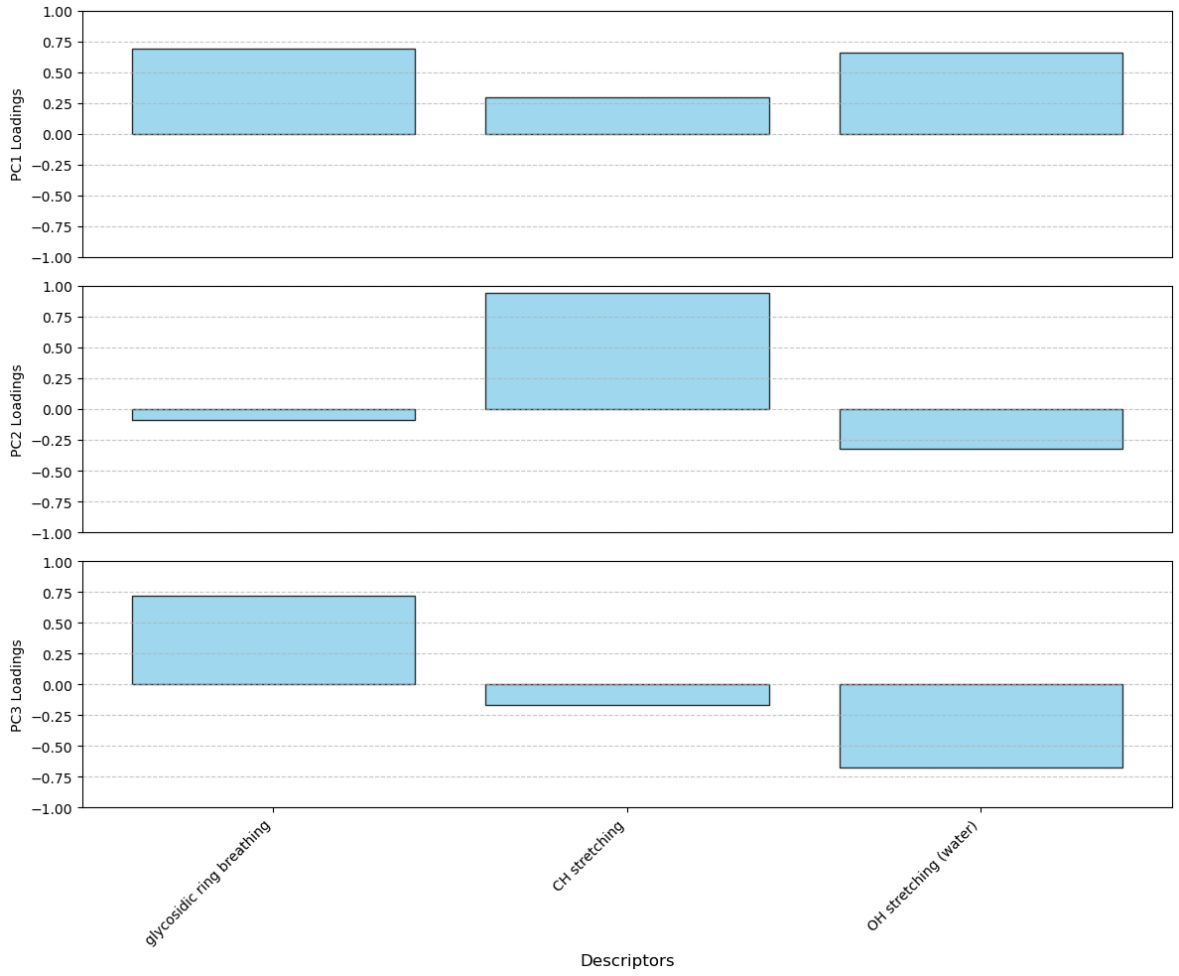

Figure 6.23: Loadings of the descriptors onto each principal component for the PCA evaluation of the FSRM dataset of linen fibers in water.

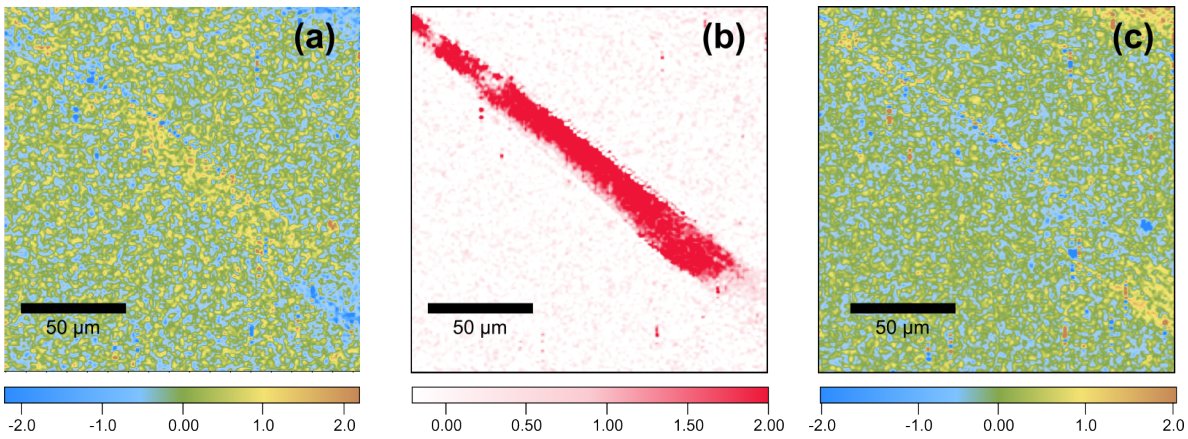

Figure 6.24: Map plots of the PCA scores for the evaluated FSRM measurement of linen fibers in water for principal components (a) 1, (b) 2, and (c) 3.

PCA evaluation of wool fibers

For wool, similarly as for linen, only two spectral descriptors were defined based on its Raman spectrum. Therefore, 3 descriptors were employed for the PCA, including the descriptor associated with the OH stretching vibration of water. The corresponding scree plot shown in Fig. 6.25 reveals that PC1 explains most of the variance in the data. The plot seems to level off after PC2 and the explained variance of PC3 is below 10%, suggesting that two principal components suffice for the reduction of dimensionality in the dataset. However, as only three principal components were computed, the further evaluation for all principal components will be shown here.

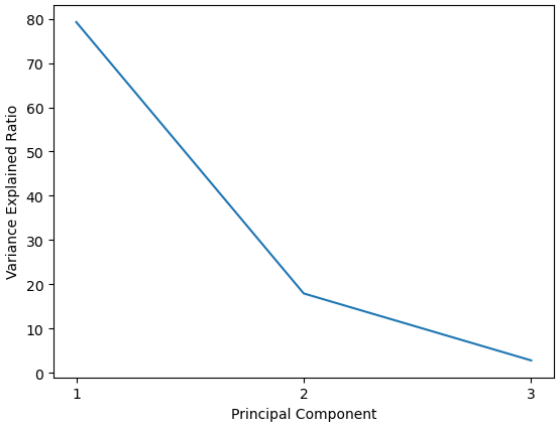

Figure 6.25: Scree plot of the PCA evaluation of the FSRM dataset of wool fibers in water. In total, three descriptors were used for the PCA, therefore three principal components can be computed.

From the loadings of the descriptors on PC1, as depicted in Fig. 6.26, it cannot be deduced which sample regions are most likely to have high scores for PC1. For PC2, both descriptors associated with Raman bands of wool show a higher loading relative to the descriptor associated with water. Therefore, pixels within the fiber are expected to have a high score for PC2. For PC3, in turn, the highest loading descriptor is the one associated with water, suggesting that pixels within the water region of the scanned area will show higher scores.

This is reflected in the maps color-coding the PCA scores shown in Fig. 6.27. The map for PC1 (Fig. 6.27(a)) shows that, for the sample regions where water is expected, pixels have positive PCA scores (yellow to red coloring), whereas in the regions where the wool fiber is expected, the pixels have negative scores (blue coloring). As the descriptor for the CO stretching vibration of wool loads positively onto PC1 and the descriptors describing the CH stretching and OH stretching Raman bands of wool and water both load negatively, it is likely that PC1 mostly describes variations in the noise pattern observed in water spectra of this dataset. The Raman band associated with CO stretching is only slightly above noise level for a spectrum recorded with an acquisition time of 1 s and, therefore, likely not observed in the data at hand. Specifically in the water region of the scanned area, this Raman band is not expected in general.

The map of the score for PC2 (Fig. 6.27(b)) displays the highest scores for pixels

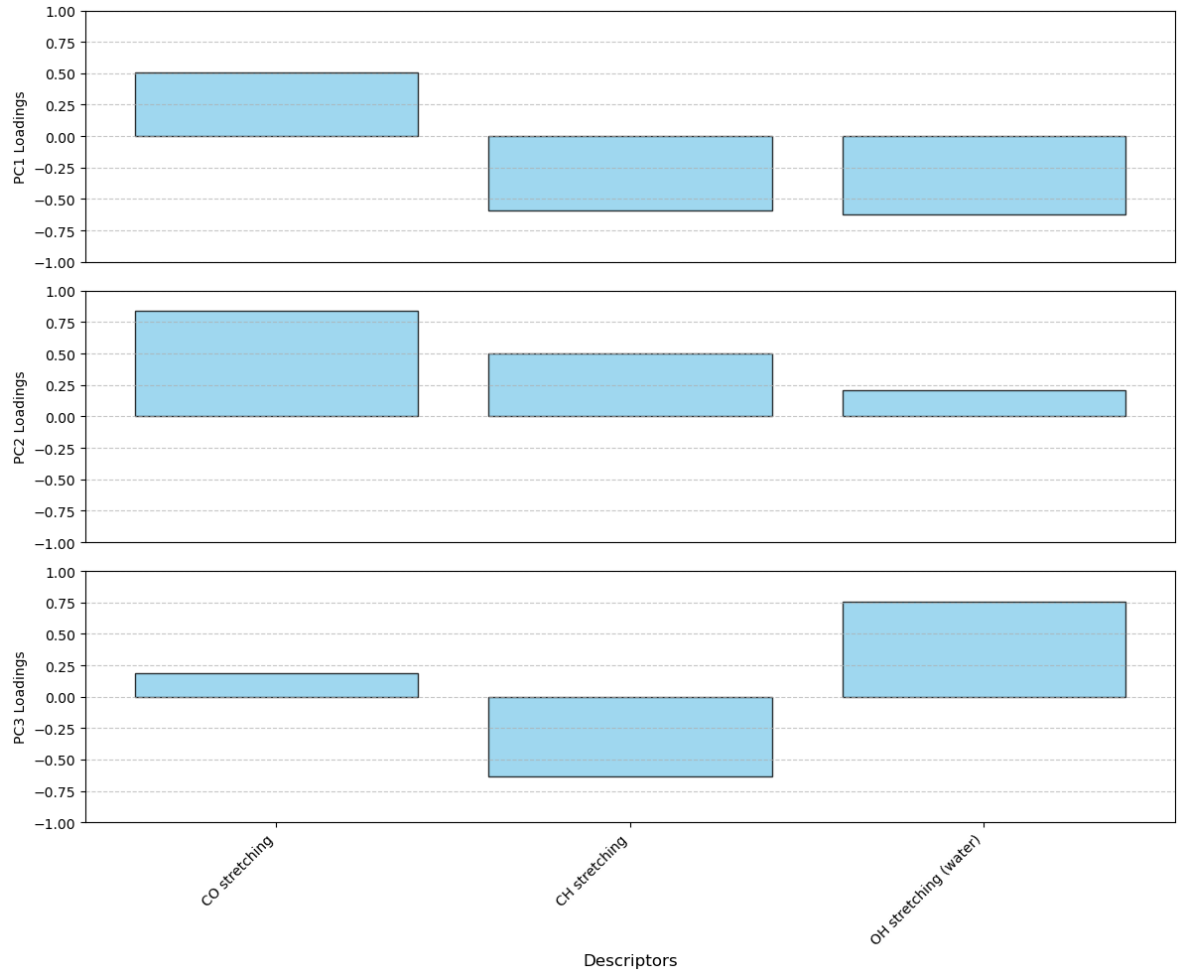

Figure 6.26: Loadings of the descriptors onto each principal component for the PCA evaluation of the FSRM dataset of wool fibers in water.

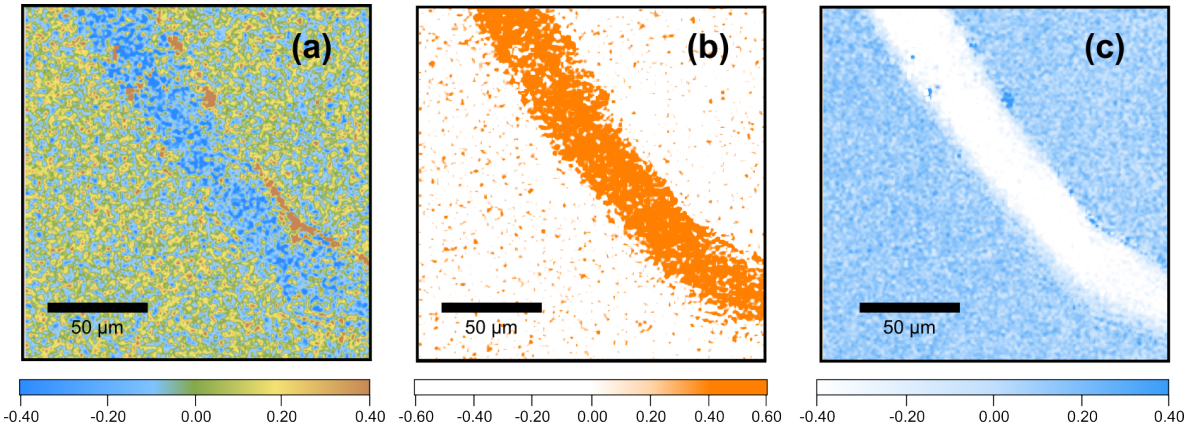

Figure 6.27: Map plots of the PCA scores for the evaluated FSRM measurement of wool fibers in water for principal components (a) 1, (b) 2, and (c) 3.

expected to belong to the wool fiber, whereas the "negative" of that image is observed for the map of PC1 scores (Fig. 6.27(c)), which shows the highest scores in the water

region of the scanned area.

Overall, evaluations of the FSRM measurements of single fibers using PCA mostly lead to similar results as expected from the FCM evaluations. However, the algorithm is expected to work better if more spectral descriptors were employed.

FSRM measurements of samples containing different types of fibers

FSRM maps of samples containing more than one type of fiber were recorded as well. Examples of such a mixture of two fibers are shown in Fig. 6.28. The maps show images of polyester and nylon fibers dispersed in water.

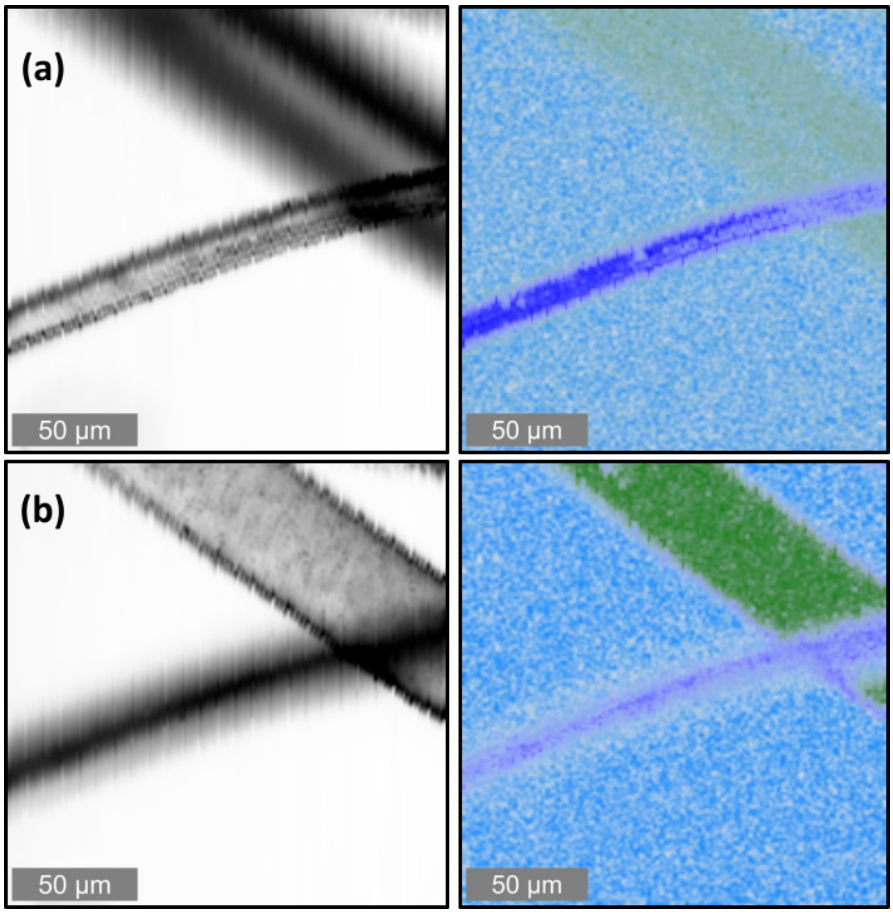

Figure 6.28: FSRM imaging of nylon and polyester fibers dispersed in water at different focal planes, (a) and (b). The 200 x 200 µm maps with 1 µm spatial resolution and an acquisition time of 10 ms/pixel were recorded within approximately 7 minutes. For both focal planes, the images of the Raman probe's transmission (left) and the false-color FCM cluster image (right) are shown. In the FCM images, the membership probabilities for the cluster corresponding to nylon (green), polyester (dark blue), water (light blue), and distortion (grey) are color-coded on a scale from 0 to 1, with 0 being white and 1 full saturation of the respective color. Adapted from ref. [121].

As previously shown, the nylon fibers used have a much larger diameter than the polyester ones. It can be seen in the maps that the two fibers are positioned on top of

each other, which resulted in no common focal plane for the measurement which yielded good signal for both fibers simultaneously. Measurements of the same sample region at two different focal planes are shown, as the transmission maps on the left side of Fig. 6.28 show that two fibers are visible but for the first focal plane (Fig. 6.28(a)), the smaller fiber (polyester) appears better defined than the larger one (nylon). The nylon fiber is therefore positioned partially or completely outside of the focal plane. This is also reflected in the corresponding false-color FCM cluster image on the right side. The regions within the polyester fiber display a darker hue than regions within the nylon fiber. As not all scanned regions of the nylon fiber lie within the focal plane, signal levels are generally lower and, as a result, the degree of membership of these spectra to the nylon cluster decreases. Additionally, the signal levels of the averaged cluster spectrum are low. FSRM images of the same sample region recorded on a different focal plane (Fig. 6.28(b)) lead to a slightly different result. Here, the larger nylon fiber appears better defined in the transmission map (left), as well as in the FCM map (right). This is another good demonstration of the sectioning capabilities of FSRM (cf. Section 4.3, Fig. 4.10). The two fibers can be distinguished by their respective cluster spectra shown in Fig. 6.29.

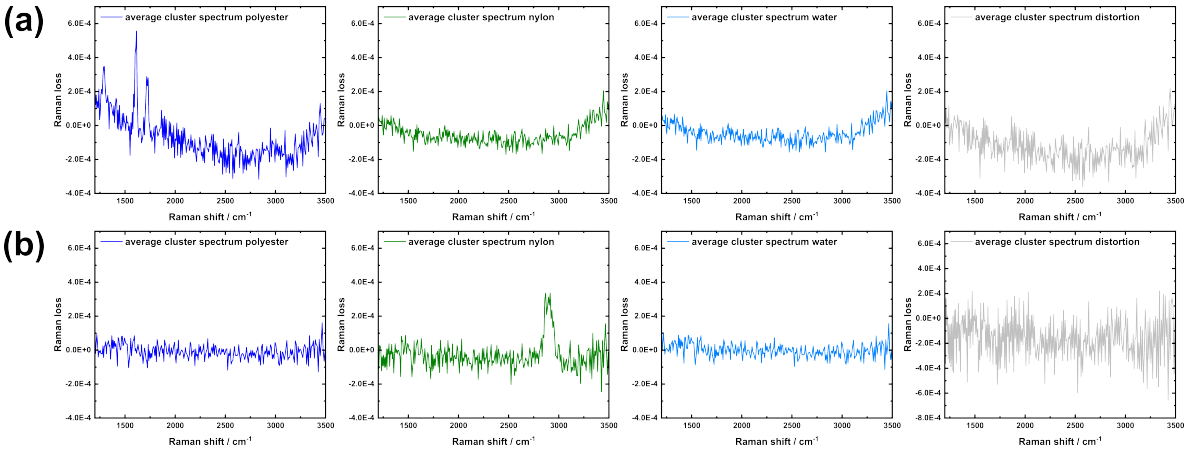

Figure 6.29: Averaged spectra of the FCM clusters of the Raman maps shown in Fig. 6.28 for the two focal planes (a) and (b). All spectra assigned to one cluster were averaged. Adapted from ref. [121].

As described above, for each focal plane, the spectrum of the respective fiber outside of the focal plane does not display noteworthy Raman signal in the expected wavenumber range. However, by acquiring two separate FSRM maps at different focal planes, the two fibers can be easily distinguished by their Raman spectra. Within *one* focal plane, a distinction is possible due to the size and shape of the fibers.

A PCA was also applied to the FSRM data of both focal planes. Nine descriptors were employed for the analysis. Therefore, nine principal components were computed. The scree plot shown in Fig. 6.30 shows that after the fifth principal component, the graph flattens out and the last four principal components only explain a small amount of variance in the data. Consequently, the first five principal components will be further investigated here.

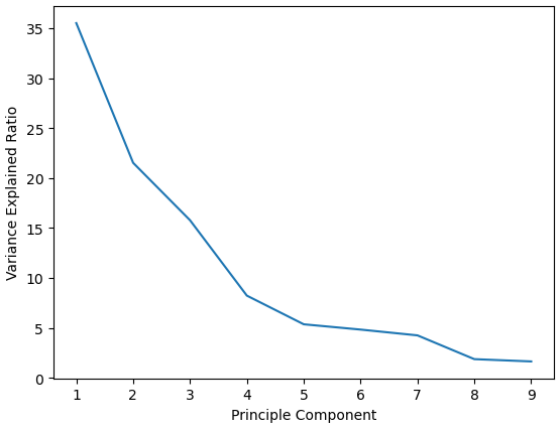

Figure 6.30: Scree plot of the PCA evaluation of the FSRM dataset of polyester and nylon in water, focal plane (a).

The loadings of the descriptors onto the respective principal components are shown in Fig. 6.31. From most of the loadings alone, no expected pattern can be deduced. PC2 is expected to have the highest scores in regions within the polyester fiber, as all descriptors associated with polyester spectra display positive loadings.

The respective plot of the score for PC2 shown in Fig. 6.32(b) confirms this. Pixels within the polyester fiber, as identified by the transmission and FCM clustering, have the highest scores. However, also the pixels within the water region of the scanned area have positive scores, albeit lower than for the polyester region. Pixels lying within the nylon fiber have a negative score. The other maps color-coding the principal component scores do not show relevant patterns which enable clearly discerning one of the substances the sample is comprised of. The score map for PC1 (Fig. 6.32(a)) displays a pattern similar to that of PC2. PC3 and PC5 (Fig. 6.32(c) and (e), respectively) appear to be "negative" images of the polyester fiber. The loadings of the respective descriptors describing nylon are, in fact, mostly negative. PC4 (Fig. 6.32(d)) might represent a noise pattern, as the scores are evenly high for regions within both fibers.

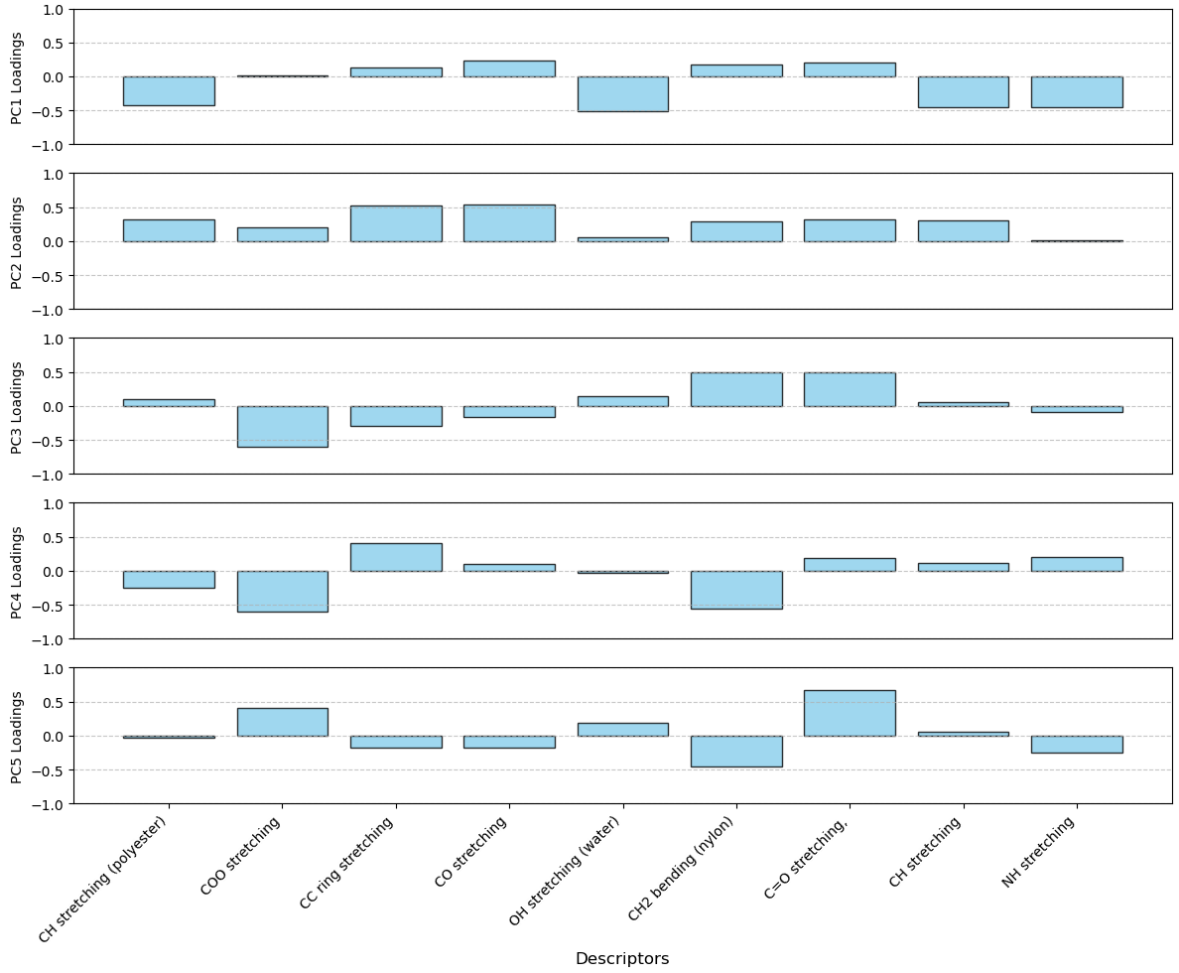

Figure 6.31: Loadings of the descriptors onto each principal component for the PCA evaluation of the FSRM dataset of polyester and nylon fibers in water, focal plane (a).

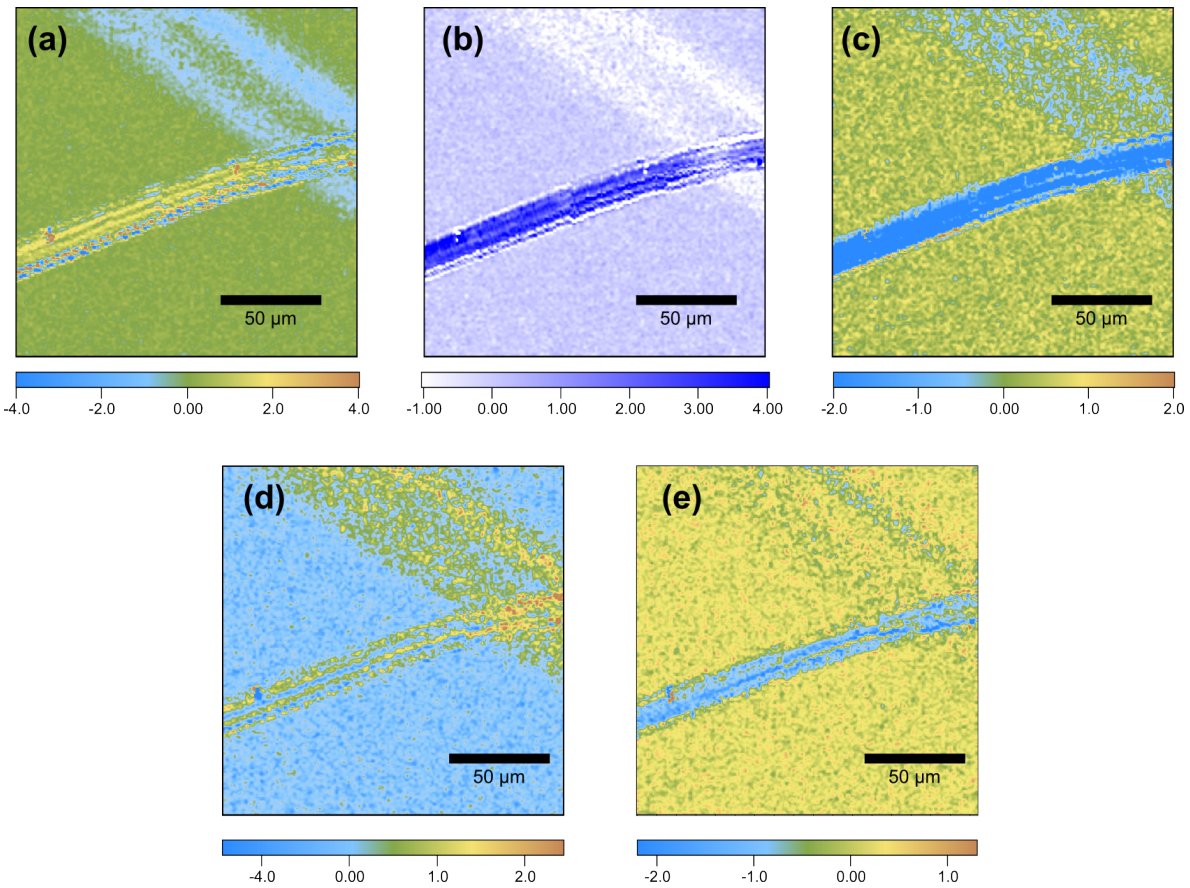

Figure 6.32: Map plots of the PCA scores for the evaluated FSRM measurement of polyester and nylon fibers in water, focal plane (a), for principal components (a) 1, (b) 2, (c) 3., (d) 4, and (e) 5.

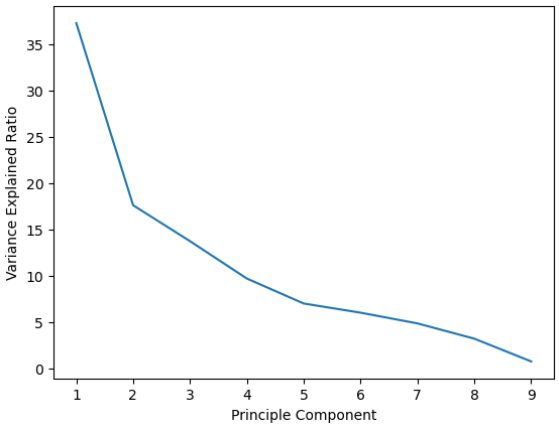

Figure 6.33: Scree plot of the PCA evaluation of the FSRM dataset of polyester and nylon in water, focal plane (b).

Similar to the PCA evaluation of the measurement of the first focal plane, the scree plot for the second focal plane shown in Fig. 6.33 becomes more level after the fifth principal component. Only five principal components are therefore considered for further evaluation.

The loadings of the applied descriptors for each principal component, as summarized in Fig. 6.34, also do not show clear patterns, which is similar to the evaluation of the first focal plane. PC2 shows a relatively high positive loading for the descriptor associated with CH stretching of the nylon and negative loading for the descriptors associated with CH stretching of polyester and OH stretching of water. Pixels within the area of the nylon fiber are therefore expected to display high PCA scores. For PC4, a relatively high loading of the CH_2 bending descriptor of Nylon is observed. However, polyester features the same bond and therefore a Raman active mode in the same region. PC4 might therefore display high scores in the polyester region of the sample. However, the COO stretching descriptor displays a negative loading, which would not be expected.

The color-coded maps showing the PCA scores for each pixel, shown in Fig. 6.34, show the same trends as can be deduced from the loadings. PC1 and PC3 (Fig 6.34(a) and (c)) do not show a distinct pattern. The scores of pixels within the nylon fiber are slightly higher than the surroundings. Along the edges of the fibers, the scores are negative. This might be attributed to higher noise due to scattering artifacts, as explained for the analysis using FCM. PC5 (Fig. 6.34(e)) displays a similar pattern but the scores within the nylon fiber are comparable to the surroundings. As expected from the loadings, scores for PC2 (Fig. 6.34(b)) are notably higher in the nylon fiber region than outside. The scores of PC4 (Fig. 6.34(d)) are higher within the polyester fiber region than in the water region, whereas the nylon fiber region displays negative scores.

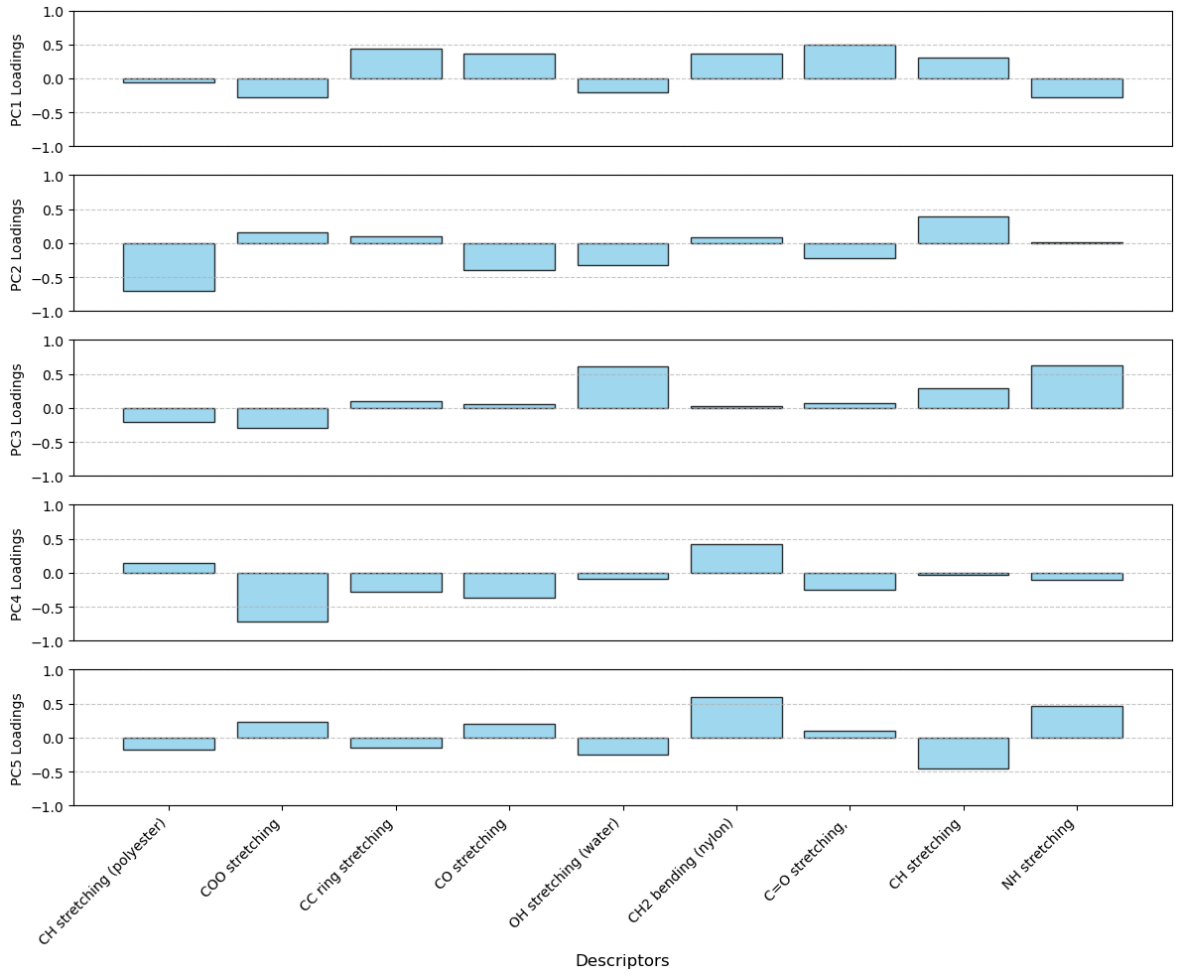

Figure 6.34: Loadings of the descriptors onto each principal component for the PCA evaluation of the FSRM dataset of polyester and nylon fibers in water, focal plane (b).

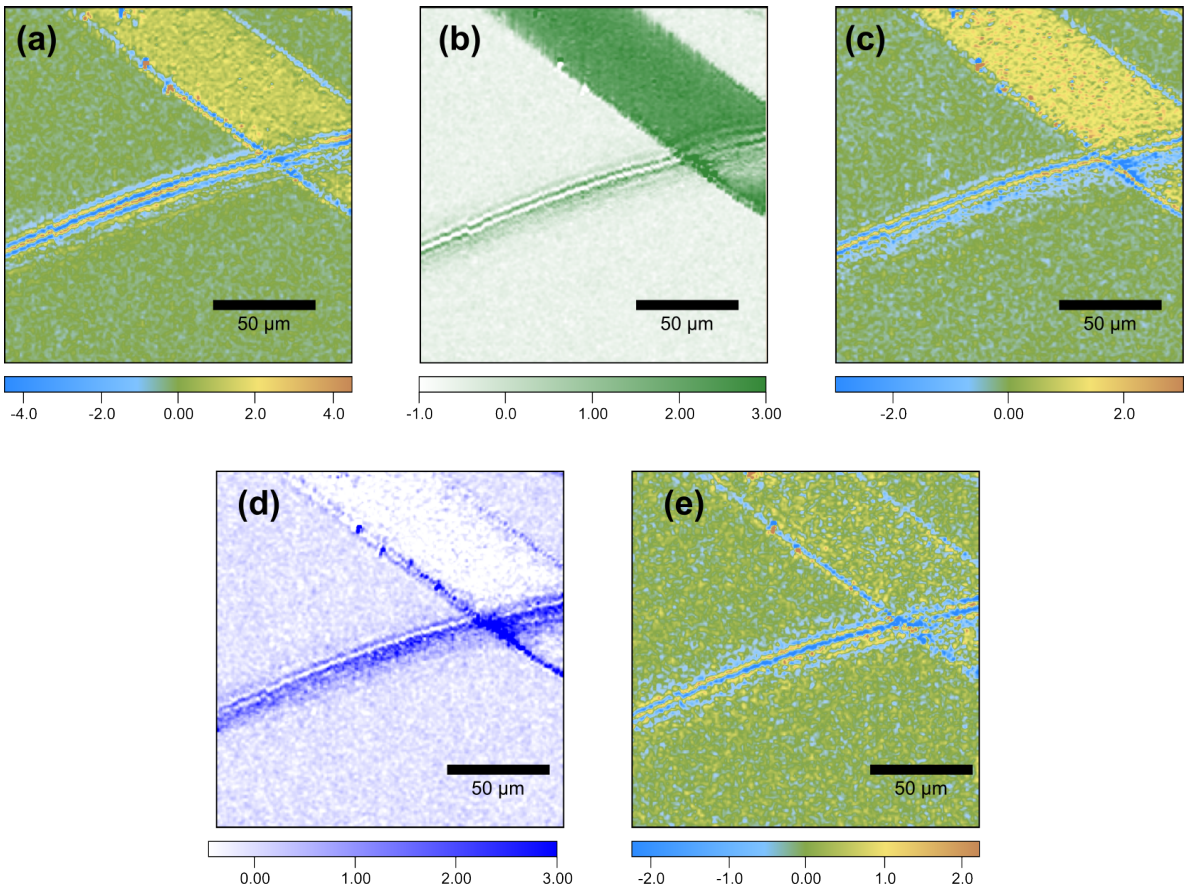

Figure 6.35: Map plots of the PCA scores for the evaluated FSRM measurement of polyester and nylon fibers in water, focal plane (b), for principal components (a) 1, (b) 2, (c) 3., (d) 4, and (e) 5.

Evaluations of an everyday sample: denim fabric

Denim, the fabric of which jeans pants are made, is very popular nowadays and regularly worn by many people. It is woven with blue as well as white threads. The sample at hand, which was taken from a used pair of jeans, was handled in the same manner as other samples described above. Separate spectra were recorded for reference in a single position of the fibers. According to the label, spectra of cotton and polyester were expected to be found. Like linen, cotton consists mainly of cellulose.

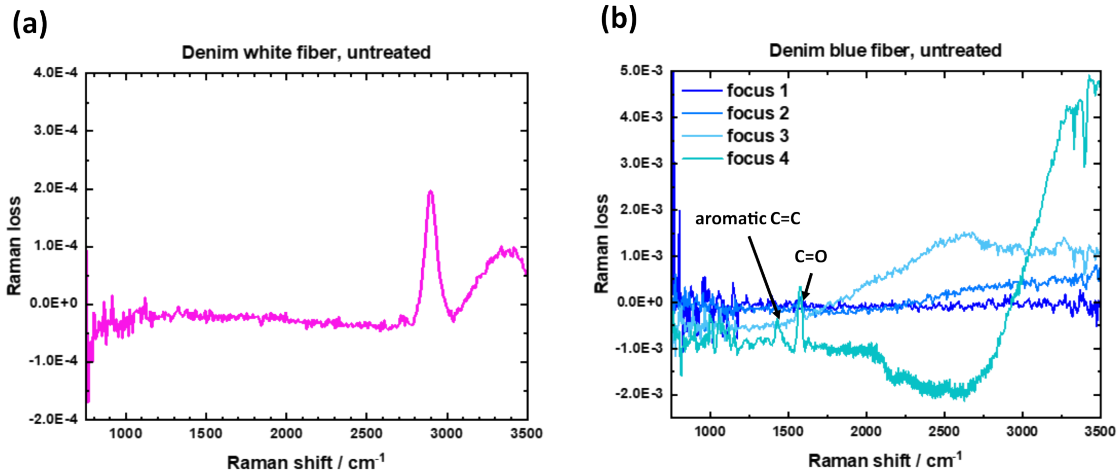

Figure 6.36: Spectra of untreated white (left) and blue (right) denim fibers. The acquisition time was 1 s/spectrum. For the blue fiber, different focusing conditions at the same sample position led to different baseline shifts, which can be attributed to non-linear effects other than stimulated Raman scattering. For focus condition 4, two Raman signals can be observed. Adapted from ref. [121].

The FSRM spectrum recorded in a position of a white fiber shown in Fig. 6.36(a) displays the same characteristic Raman bands as expected for cellulose, namely the CH stretching vibration centered at 2896 cm^{-1} and the broad band of OH stretching of water ranging from 3100 cm^{-1} to 3600 cm^{-1}, as the fiber is soaked with water. A clear spectrum of a blue fiber could not be recorded, as strong non-linear effects were observed, as shown in Fig. 6.36(b). Depending on the focusing conditions, the baseline was strongly distorted. Unlike for the alcoholic solvents examined in Section 6.1, not only a downward shift was observed but the distortions were unevenly distributed along the baseline and of a different shape for each focusing condition. As a blue dye absorbs in the red region of the visible spectrum, it is expected that the Raman probe is partially absorbed, resulting in distortions of the spectra.

For one focus condition, two Raman bands can be distinguished in the FSRM spectrum. The bands might be those associated with the C=C and C=O stretching vibrations of polyester, albeit being shifted to 1431 cm^{-1} and 1572 cm^{-1} compared to 1614 cm^{-1} and 1723 cm^{-1} expected from the reference spectra recorded. Such a shift can

be caused by the incorrect focusing conditions observed in the spectrum and higher scattering due to the dark material, resulting in the probe light not being coupled into the detector correctly. This might have shifted the overall FSRM spectrum obtained. However, as two bands can be discerned in an approximate wavenumber region where polyester is expected to display Raman bands, it can be concluded that the blue fibers consist mainly of polyester.

Pieces of fabric were then bleached with NaOCl. When the fabric was visually discolored, a sample was prepared like for other samples. No relevant baseline distortions were observed for the bleached fabric and spectra of both cotton and polyester could be recorded, as shown in Fig. 6.37.

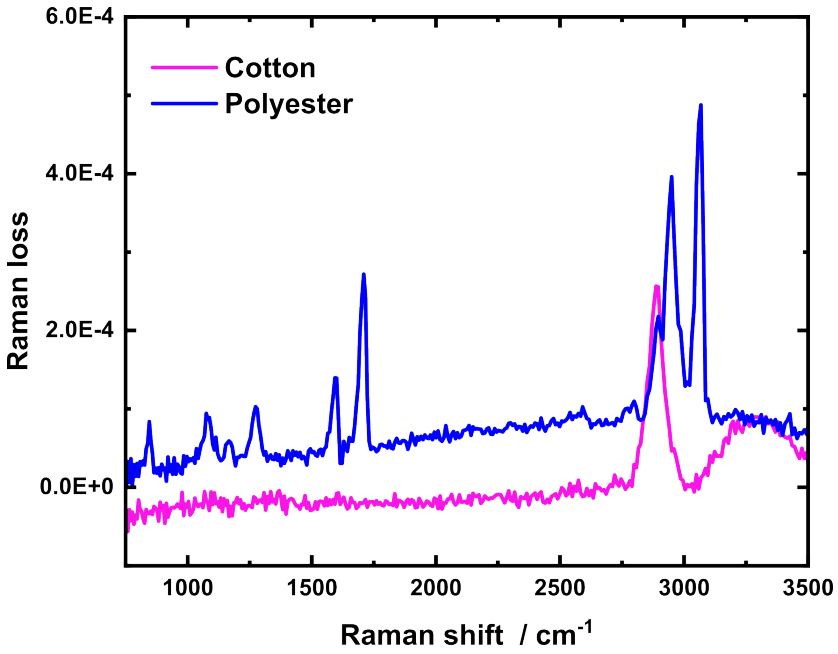

Figure 6.37: FSRM Raman spectra of bleached denim fibers. The spectra were recorded with an acquisition time of 1 s. Adapted from ref. [121].

Corresponding FSRM maps of two regions scanned within the same prepared sample of the bleached fibers, as shown in Fig. 6.38, further demonstrate that the two main components of the denim fabric, cotton and polyester, could be distinguished. This is of special interest as it shows that, for an everyday sample, natural and synthetic fibers can be differentiated.

The maps were evaluated using FCM clustering. For both scanned regions, the transmission image on the left displays two fibers, one of them within the focal plane and the other one outside. The FCM cluster images in the middle show one fiber consisting of polyester (Fig. 6.38(a)) or cotton (Fig. 6.38(b)), as determined by their respective averaged cluster spectra on the left.

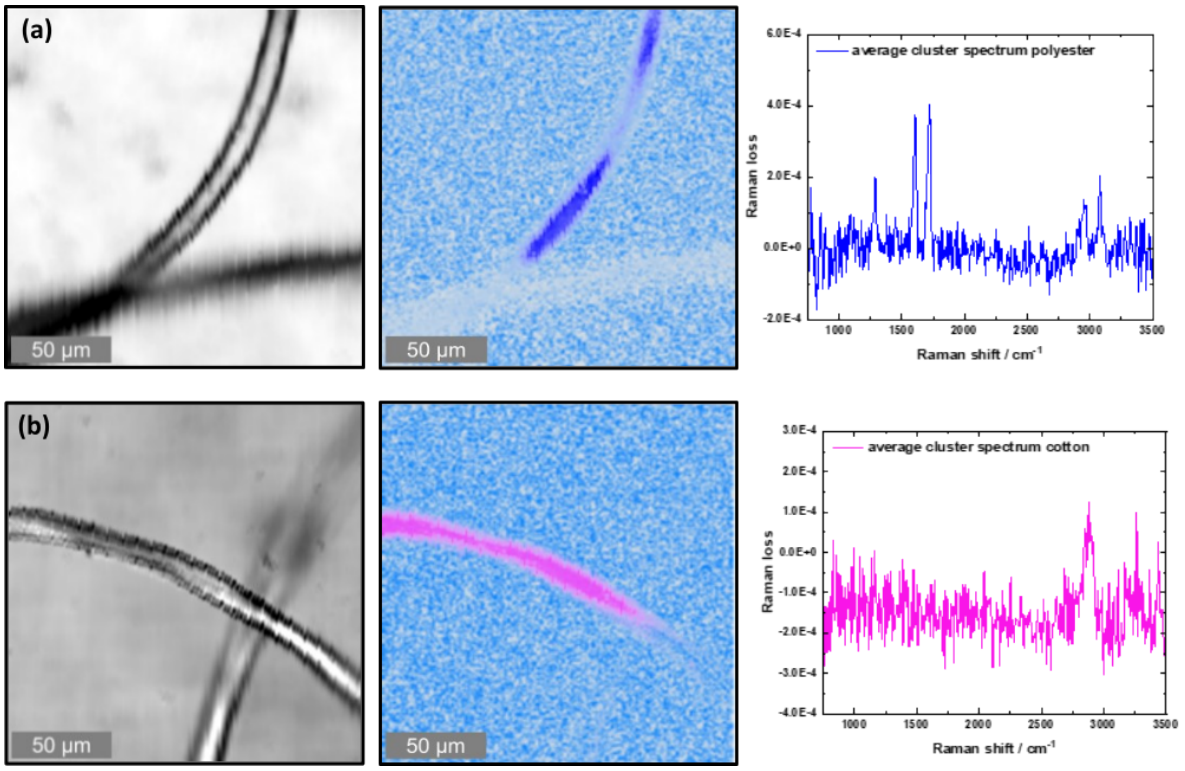

Figure 6.38: FSRM imaging of bleached denim fibers. Acquisition of the 200 x 200 µm maps with a spatial resolution of 1 µm and acquisition times of 10 ms/spectrum took approximately 7 minutes. Both measurements show different regions of the same sample, featuring a polyester (a) and cotton (b) fiber. The corresponding averaged Raman spectra are shown on the right side. Adapted from ref. [121].

7 Conclusion and Outlook

7.1 Summary of Findings

Since the invention of plastics, they have become ubiquitous and have significantly improved many aspects of daily life. However, their release into the environment presents numerous challenges, one of which is their degradation into microparticles, the focus of this thesis. These microplastics have been detected in nearly all environmental settings - land, air, and water - and pose threats to ecosystems. Trophic transfer is highly likely, as MPs have been found in food, beverages and ultimately human specimens. The potential health risks associated with these particles are difficult to assess. Due to their widespread presence, it is impossible to compare individuals regularly exposed to MP with those who are not. While animal studies suggest possible health risks and behavioral changes after prolonged exposure to MP, these experiments typically use concentrations higher than those encountered in daily life.

Monitoring the environmental distribution of MP is essential to understand its pathways and reducing their release into the environment. This will ultimately help reducing the risks of ingestion by humans and animals alike. However, the absence of standardized protocols for sample preparation and evaluation complicates the handling of environmental samples. Cross-contamination is highly likely, making it crucial to process samples in ideally plastic-free environments and include blank controls to check for contamination. Additionally, commonly used analytical methods in MP research often fail to reliably identify MP particles. For instance, visual identification, while rapid, frequently leads to misclassifications of synthetic and natural particles. Vibrational (micro-)spectroscopic techniques provide both qualitative and quantitative insights into MP composition, but both Raman and IR microscopy have their respective limitations. The main disadvantages of IR microscopy are its sensitivity to water and a low spatial resolution due to the diffraction limit of the light employed. On the other hand, Raman microscopy, which is relatively insensitive to water and offers the capability to detect smaller particles, is often challenging because of fluorescence signals superimposing with the Raman signals and it is slow due to low scattering cross sections, resulting in long measurement times. Non-linear Raman techniques aim to overcome the typical limitations of spontaneous Raman scattering. Microscopical techniques based on SRS have been introduced before, an inherently destruction- and label-free approach which enhances measurement times and typically does not suffer from strong fluorescent background. However, in classical approaches of SRS microscopy, one typically compromises either spatial or spectral coverage.

This thesis highlights the capabilities of femtosecond stimulated Raman microscopy (FSRM) in overcoming some of the key challenges in MP analysis. FSRM is a fast, broadband technique that enables the acquisition of full spectral information with complete spatial coverage in a region of interest (ROI), allowing measurement and evaluation without prior knowledge of a sample's components. The spectra recorded with FSRM were shown to closely resemble those obtained from spontaneous Raman spectroscopy. Spontaneous Raman spectra for several solvents displaying a wide range of Raman signals were converted to compare with spectra recorded with FSRM. The spectra match within the expected range in terms of relative signals. However, for methanol and other alcohols, broad Raman bands expected in the lower-wavenumber region could not be observed. Instead, a baseline-shift upon changing the focus was observed solely for these solvents. One further possible explanation which was not studied here can be the focusing conditions. In FSRS studies of methanol, the expected Raman bands could be observed [119]. In the system described, the Raman probe is focused to a spot size of around 60 µm [119]. In FSRM, the Raman probe is focused to be approx. 1 µm in diameter, which is a significantly smaller spot size. It should be tested if increasing the spot size might affect the spectrum observed. This effect as well as the potential impact of the chain length of the alcohol should be further evaluated in future studies.

FSRM was then applied to analyze primary MP particles, including standard particles and those extracted from consumer goods (facial scrubs). The lack of further available commercial samples containing primary MP limited the evaluation of MP in consumer goods by FSRM to two samples. Subsequently, FSRM was used to investigate microfibers, the most common shape of MP found in the environment. Fabric samples representing the most commonly produced textiles worldwide were analyzed using a preparation protocol that mimicked that for potential natural aqueous samples. Evaluation of FSRM data was performed using statistical methods such as fuzzy c-means clustering and principal component analysis, demonstrating their utility for future analysis of samples with unknown compositions. For future sample evaluations, PCA can be useful to determine the number of substances present in a scanned sample region for a sample of unknown composition. The evaluation of a pre-analysis with a PCA algorithm can then be followed by an algorithmic clustering of data employing FCM, which was shown here to yield both good images and averaged spectra of FSRM datasets. However, for evaluations of scanned regions with fibers positioned in different focal planes, PCA was not found to accomplish additional insights. PCA should be used as a tool to reduce data complexity but with the two main constituents of the sample not fully contained within one dataset, the evaluation appeared to add more complexity.

Finally, the feasibility of using FSRM to analyze an everyday material was demonstrated for denim extracted from jeans. The main components, cotton and polyester, were successfully distinguished, highlighting the ability to differentiate natural and synthetic materials in a sample. This emphasizes the potential of applying FSRM for the analysis of MP, as an adequate distinction has often been lacking in reports.

7.2 Comparison with Existing Techniques

In this thesis, FSRM was shown to be a suitable technique for MP analysis. Now, its performance will be compared with that of existing techniques. The current modalities of FSRM allow a full spectral coverage in a wavenumber range of 1250 - 3500 cm^{-1} with approximately 30 cm^{-1} spectral resolution when recording a Raman map at an acquisition time of 10 ms/pixel. Currently, Raman bands expected at wavenumbers below 1250 cm^{-1} cannot be adequately assessed because the noise observed exceeds that of the signal in this spectral region. This is caused by the smaller light flux of the Raman probe compared to its center, resulting in an increased noise level. FSRM maps shown here were recorded for an area of 200 x 200 µm with a step size of 1 µm, adding up to 40 000 total spectra. Recording the maps required approximately 7 min. The area which can be scanned at once can be extended by automatically scanning adjacent areas. A motor is implemented which can move the stage the sample is mounted on along the x-axis after an area was scanned. This motor was not applied in this thesis. For the parameters applied here and considering the total time required to record a map, the pixel acquisition time was 10.5 ms on average. The recorded Raman probe's light flux which is used to calculate the Raman spectra can also be utilized to compute its transmission through the sample. Transmission images resembling a conventional light microscope image can therefore be computed without needing to perform additional measurements. FSRM has a spatial resolution of approximately 1 µm and particles of approximately 10 µm or larger were characterized here. Smaller particles can be characterized but a precise determination of size is challenging because diffractive index mismatches between the surrounding matrix and the particles can affect the collected spectra [166].

Typical minimal particle sizes reported to be characterized employing Raman spectral maps with full spatial coverage of an ROI were reported around 5 µm [17, 29, 89]. Thus, the minimal size accessible by FSRM is comparable to existing Raman techniques. Furthermore, like other Raman imaging techniques, FSRM has a better spatial resolution than typical IR imaging techniques, which are inherently limited by the Abbe diffraction limit of the higher-wavelength IR radiation [127]. One drawback

of spontaneous Raman techniques compared to IR is laser-induced fluorescence, which can superimpose the Raman bands and render an evaluation challenging. FSRM, like other non-linear Raman approaches, is mostly unaffected by autofluorescence of samples, as the detected light has a higher energy than the exciting light here. A further advantage of FSRM is that low laser powers are employed, which prevents damage to samples [124] often reported for other Raman techniques [63]. However, as FSRM requires measurements in transmission, dark samples or samples which do not adequately transmit the probe light cannot be characterized.

Compared to IR microscopy, Raman approaches are slow because of typically low scattering cross sections. The measurement times of FSRM reported here will now be compared with other Raman approaches applied in studying MPs to showcase its potential to significantly increase measurement times for MP analytics. The total time required for a full scan of an area mostly depends on the acquisition time per pixel. As mentioned above, acquisition of one full spectrum, i.e. one pixel, in FSRM was 10 ms here. For spontaneous Raman microscopy, acquisition times were reported to typically be in the order of around 1 s [89], 100 times longer than shown here. Similar to FSRM, full spectral coverage is achieved. A short acquisition time of 20 ms was reported by Elert *et al.* [173], which is only twice the time reported here for FSRM. However, the reported time required for acquisition of single spectra shown was in the order of 10 s. It appears that scanning for imaging was carried out at faster acquisition times but full spectra for characterization were acquired with longer averaging. Even with acquisition times reported as short as 20 ms/pixel, a scan of a 200 x 190 µm area with 1 µm steps required 35 mins. The average acquisition time per pixel is therefore reduced to 55 ms/pixel by other limitations, for example the speed of movement of the scanning stage. Such factors do not significantly increase the acquisition time of FSRM in practice.

Different approaches for the application of conventional SRS in MP analytics have been reported before. For measurements reported by Laptenok *et al.* [108] and Genchi *et al.* [63], a sample region with an area of 1 cm^2 was scanned in steps of 2 µm within 40 mins, which is an average of 0.1 ms/pixel, equal to the lowest possible acquisition time in FSRM for full spectral coverage, which was not applied here because of insufficient Raman signal and displacement of fibers observed upon fast scanning. However, only a single Raman shift was addressed for the reported SRS microscopy. A full Raman spectrum in the wavenumber range 800 – 3200 cm^{-1} was recorded in a single position of interest after this pre-scan within 60 s by tuning the frequency difference of the two lasers applied. In comparison, a single FSRM spectrum acquired in one position was recorded here within only 1 s and displays adequate Raman signal in a broader spectral

range of 750 - 3500 cm^{-1}. In a different approach at SRS microscopy, Zada *et al.* [107] have fully scanned an area of 2 cm^2 with 3 µm steps for 6 selected Raman shifts. A total time of 4.5 h was reported, which equals an average acquisition time of 0.15 ms/pixel. Scans were successively performed for the separate Raman shifts to be addressed, so the time required to tune the different wavenumbers between the measurements became a limiting factor. Recording a single-wavenumber map was reported to only require 22.45 s, which equals an average acquisition time of 0.02 ms per pixel for single-wavenumber images. In FSRM, unlike the reported conventional methods, wavenumber tuning is not necessary and therefore does not increase time required for measurements.

7.3 Future Directions and Applications

7.3.1 Considerations for Microplastics Monitoring

In this thesis, FSRM was introduced as a new broadband technique for fast MP analysis. Nearly complete Raman spectral information is achieved for every position within a scanned ROI. A sample preparation protocol was developed which mimics the preparation of clean, aqueous samples contaminated by MP. A special emphasis was placed on microfibers, the dominant shape of MP particles observed in various environmental settings. Naturally, the application of FSRM should now be extended to real-world samples. As a potential next step, washing machine effluent water can be evaluated for MP contamination to extend the application of FSRM in microfiber analysis. Larger volumes of liquid will have to be filtered, as the sample size prepared here was typically small and highly concentrated. Contamination by other organic matter which needs to be extracted to enable filtration and analysis is expected to be low, so it is expected that the developed protocol can be extended to these samples. However, the detergents or conditioners commonly used in the home can block the filter [12], so the washing cycles will likely have to be performed without these ingredients or methods of extraction must be incorporated. To ensure a correct evaluation of samples, larger regions of a filter need to be measured, either a method to measure the full filter has to be implemented or an adequate random selection of regions to ensure a statistically correct evaluation, which can give insight on the number of particles on the filter. Approaches for selecting ROIs have been suggested to ensure they represent the relative particle distribution on the filter, measurements are reproducible, and that the number of MP particles can be appropriately extrapolated [174]. Some suggested approaches are visualized in Fig. 7.1.

For a filter with a diameter of 25 mm like the one used in this thesis, several ROIs of 2 x 2 mm should be recorded. With the current modalities of FSRM, a region of

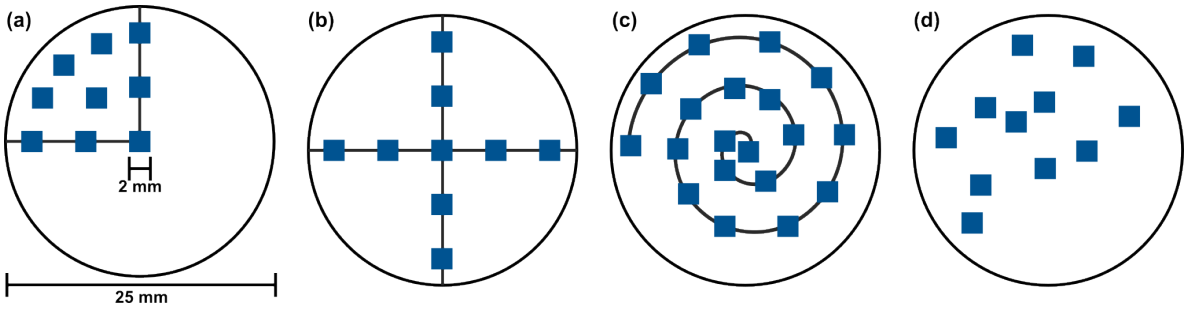

Figure 7.1: Suggested approaches for selecting ROIs for representative measurements of MP particles on filters of the size applied in this thesis. For the filters with a diameter of 25 mm, several 2 x 2 mm regions are suggested to be measured. Suggested positions are (a) distributed on a quarter of the filter, (b) along the cross section of two axis, (c) in a helical order, and (d) randomized selection based on distribution of particles. Adapted with permission from ref. [174].

0.2 x 2 mm can be measured at once. Technical adjustments are therefore necessary, for example a second motor can be added to the stage on which the sample stage is mounted to also automatically cover a larger range in the y-axis. Alternatively, several regions positioned directly next to each other can be scanned by manually changing the position. With the suggested approaches of measuring 9 ROIs distributed on one quarter of the filter (Fig. 7.1(a)) or along the cross section of the filter along two axis (Fig. 7.1(b)), 7.3% of the total filter area are scanned. Measuring ROIs in a helical pattern (Fig. 7.1(c)) achieves a coverage of 15.5% of the total filter area. A randomized selection of ROIs based on distribution of particles as shown here (Fig. 7.1(d)) covers 8.2% of the filter area. The most feasible options for FSRM analysis need to be determined in further studies and coupled with adequate statistical evaluation.

7.3.2 Enhancing Measurements and Data Processing

Enhancing the signal-to-noise ratio (SNR) of FSRM spectra would improve both the detection of weak Raman bands and the ability to differentiate between various components within recorded Raman maps. Increasing the SNR would allow for more spectral data to be utilized in analyses, leading to more accurate and reliable results. Several approaches to achieving a higher SNR will be discussed in the following.

The Raman pump pulse used in the measurements presented here was observed to have a spectral width of approximately 30 cm^{-1}, whereas a narrower width of 20 cm^{-1} was reported previously [131]. The Raman signal depends on the pump's spectral width, which should ideally be equal to the intrinsic linewidth of the Raman band. Therefore, the total signal observed in this study is lower than in earlier measurements. This reduction can partially be attributed to general deterioration in the fiber-based amplifier. At the fiber connections, some light intensity is lost. The connections are sensitive to

movement but frequently adjusted for system alignment. These adjustments degrade the fibers' quality over time, resulting in less light passing and a broadening of the passing light's spectrum. Moreover, it is possible that the grating which narrows the light was not aligned perfectly. While some components of the amplifier were replaced during this thesis, restoring the original spectral width was not possible. Further renewal of key amplifier components could help reduce the pump's spectral width and thereby enhance the Raman signal.

Another approach to improving the SNR focuses on reducing spectral noise in the lower-wavenumber region, particularly around 1000 cm^{-1} and below. The light flux of the Raman probe decreases in this region relative to its maximum observed in the Raman spectra at approximately 2100 cm^{-1}, resulting in an uneven distribution of noise across the spectrum. A more uniform distribution of light would result in a more balanced noise pattern in the Raman spectra. To address this, a test was performed where a continuously variable neutral density (ND) filter was introduced in front of the array detector to selectively attenuate probe light associated with higher-wavenumber Raman shifts. The ND filter offers a gradual increase in attenuation along its length and can be placed in front of the diode array detector. The probe light, which is spectrally dispersed by the polychromator, will therefore be attenuated stronger for light associated with higher Raman shifts. The first 10 mm of the filter are not coated. This enables increasing the overall light flux on the sample without saturation of the detector. The expected attenuation achieved by the filter was calculated and is shown in Fig. 7.2(a). Initial tests confirmed that the filter successfully reduced noise in the

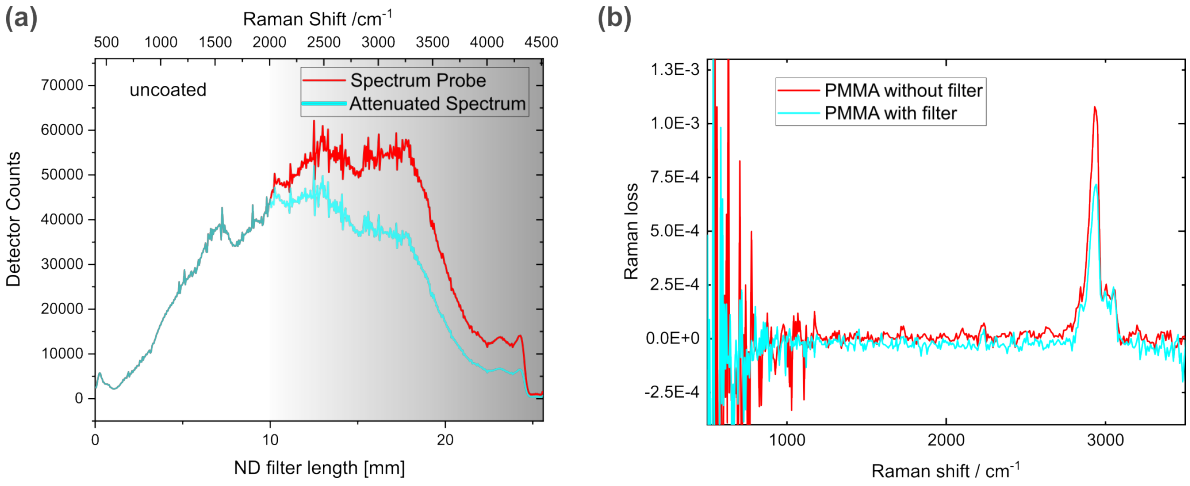

Figure 7.2: (a) Calculated attenuation of the Raman pump by a continuously variable ND filter and (b) comparison of spectra of PMMA recorded with (cyan) and without (red) an ND filter placed in front of the array detector to decrease the noise in the lower-wavenumber region. Spectra were acquired within 0.1 s, i.e. 1000 Raman spectra were averaged.

lower-wavenumber region, creating a more uniform signal distribution. A comparison of Raman spectra of PMMA with and without the filter is shown in Fig. 7.2(b). Here, no further alignment for signal quality was done between measurements, first without and then with the filter. This causes the observed decrease in the Raman signal. Notably, the noise in the lower-wavenumber region also visibly decreases, the result which was attempted to achieve. Although this approach was not further pursued during this thesis, the preliminary results indicate its potential effectiveness. Future studies should further explore the application of the ND filter to optimize spectral quality in the lower-wavenumber region.

The fixed pattern noise [172] caused by the detector's readout mechanism was recently investigated as part of a master's thesis [175]. The modulation of the Raman pump, as described in this thesis, is synchronized with the detector's readout rate of 20 kHz, meaning that each interval of the probe's spectra recorded either with or without the contribution of the pump was 50 µs. The readouts alternate between two electronic channels and, thus, the two intervals are detected via different electronic channels. The electronic differences result in slight discrepancies in the detection of each interval. When averaging only a small number of spectra, this effect can be reduced by subtracting the respective baseline. However, when more spectra are averaged, the fixed pattern noise cannot easily be accounted for. Changing the duration of the acquisition intervals addresses this issue and reduces the SNR. Specifically, modulating the pump beam at half the detector's readout-rate enables each interval to be detected for two readout cycles, consequently involving both electronic channels. This approach reduces the perceived noise for long averaging times [175].

Another potential approach to enhance spectral quality lies in post-processing. Machine learning can be a powerful tool for denoising spectra [176], potentially allowing for faster measurements while maintaining the spectral quality typically achieved with longer averaging times. Developing such an algorithm could be based on an existing generic neural network, reducing the number of spectra required for training [176]. Over time, numerous FSRM spectra have been recorded using various acquisition times. As demonstrated in Section 6.1, most Raman bands that were initially below noise level employing acquisition times typically used for FSRM maps become distinguishable in spectra averaged over 1 second. Machine learning can be employed to reconstruct these weaker signals, improving clarity of spectra without the need for long acquisition times. As the field advances, further exploration of possible applications of machine learning in FSRM could provide significant benefits, not only for denoising but also for the automated identification and characterization of unknown particles or quantitative evaluation of data.

References

[1] L. H. Baekeland, “Method of making insoluble products of phenol and formaldehyde.” US Patent 942 699.

[2] D. Crespy, M. Bozonnet, and M. Meier, “100 Years of Bakelite, the Material of a 1000 Uses”, Angewandte Chemie International Edition **47**, 3322 (2008).

[3] A. L. Andrady and M. A. Neal, “Applications and societal benefits of plastics”, Philosophical Transactions of the Royal Society B: Biological Sciences **364**, 1977 (2009).

[4] R. Geyer, J. R. Jambeck, and K. L. Law, “Production, use, and fate of all plastics ever made”, Science dvances **3**, e1700782 (2017).

[5] OECD, “Global Plastics Outlook: Policy Scenarios to 2060”, edited by S. Agrawala, E. Lanzi, and R. Dellink (2022).

[6] OECD, “Global Plastics Outlook: Economic Drivers, Environmental Impacts and Policy Options”, edited by S. Agrawala, M. Dubois, P. Börkey, and E. Lanzi (2022).

[7] Plastics Europe, “Plastics – the fast Facts 2024”, published online 2024, accessed: 20.02.2025, `https://plasticseurope.org/de/wp-content/uploads/sites/3/2024/11/PE_TheFacts_24_digital-1pager.pdf`.

[8] R. C. Thompson, C. J. Moore, F. S. vom Saal, and S. H. Swan, “Plastics, the environment and human health: current consensus and future trends”, Philosophical Transactions of the Royal Society B: Biological Sciences **364**, 2153 (2009).

[9] E. J. Carpenter and K. L. Smith, “Plastics on the Sargasso Sea Surface”, Science **175**, 1240 (1972).

[10] R. C. Thompson, Y. Olsen, R. P. Mitchell, A. Davis, S. J. Rowland, A. W. John, D. McGonigle, and A. E. Russell, “Lost at sea: where is all the plastic?”, Science **304**, 838 (2004).

[11] R. C. Thompson, W. Courtene-Jones, J. Boucher, S. Pahl, K. Raubenheimer, and A. A. Koelmans, “Twenty years of microplastics pollution research—what have we learned?”, Science **386**, eadl2746 (2024).

[12] M. A. Browne, P. Crump, S. J. Niven, E. Teuten, A. Tonkin, T. Galloway, and R. Thompson, “Accumulation of microplastic on shorelines woldwide: sources and sinks”, Environmental Science & Technology **45**, 9175 (2011).

[13] S. Allen, D. Allen, V. R. Phoenix, G. Le Roux, P. Durántez Jiménez, A. Simonneau, S. Binet, and D. Galop, "Atmospheric transport and deposition of microplastics in a remote mountain catchment", Nature Geoscience **12**, 339 (2019).

[14] M. Bergmann, S. Mützel, S. Primpke, M. B. Tekman, J. Trachsel, and G. Gerdts, "White and wonderful? Microplastics prevail in snow from the Alps to the Arctic", Science Advances **5**, eaax1157 (2019).

[15] I. Goßmann, D. Herzke, A. Held, J. Schulz, V. Nikiforov, C. Georgi, N. Evangeliou, S. Eckhardt, G. Gerdts, and O. Wurl, "Occurrence and backtracking of microplastic mass loads including tire wear particles in northern Atlantic air", Nature Communications **14**, 3707 (2023).

[16] G. Liebezeit and E. Liebezeit, "Synthetic particles as contaminants in German beers", Food Additives & Contaminants: Part A **31**, 1574 (2014).

[17] D. Schymanski, C. Goldbeck, H.-U. Humpf, and P. Fürst, "Analysis of microplastics in water by micro-Raman spectroscopy: Release of plastic particles from different packaging into mineral water", Water Research **129**, 154 (2018).

[18] C.-L. Bai, L.-Y. Liu, Y.-B. Hu, E. Y. Zeng, and Y. Guo, "Microplastics: A review of analytical methods, occurrence and characteristics in food, and potential toxicities to biota", Science of The Total Environment **806**, 150263 (2022).

[19] L. F. Amato-Lourenço, R. Carvalho-Oliveira, G. R. Júnior, L. dos Santos Galvão, R. A. Ando, and T. Mauad, "Presence of airborne microplastics in human lung tissue", Journal of Hazardous Materials **416**, 126124 (2021).

[20] A. Ragusa, A. Svelato, C. Santacroce, P. Catalano, V. Notarstefano, O. Carnevali, F. Papa, M. C. A. Rongioletti, F. Baiocco, and S. Draghi, "Plasticenta: First evidence of microplastics in human placenta", Environment nternational **146**, 106274 (2021).

[21] L. C. Jenner, J. M. Rotchell, R. T. Bennett, M. Cowen, V. Tentzeris, and L. R. Sadofsky, "Detection of microplastics in human lung tissue using μftir spectroscopy", Science of The Total Environment **831**, 154907 (2022).

[22] H. A. Leslie, M. J. van Velzen, S. H. Brandsma, D. Vethaak, J. J. Garcia-Vallejo, and M. H. Lamoree, "Discovery and quantification of plastic particle pollution in human blood", Environment International **163**, 107199 (2022).

[23] S. Liu, X. Liu, J. Guo, R. Yang, H. Wang, Y. Sun, B. Chen, and R. Dong, "The association between microplastics and microbiota in placentas and meconium: The first evidence in humans", Environmental Science & Technology **57**, 17774 (2022).

[24] A. Ragusa, V. Notarstefano, A. Svelato, A. Belloni, G. Gioacchini, C. Blondeel, E. Zucchelli, C. De Luca, S. D'Avino, A. Gulotta, O. Carnevali, and E. Giorgini, "Raman Microspectroscopy Detection and Characterisation of Microplastics in Human Breastmilk", Polymers **14**, 2700 (2022).

[25] A. B. Silva, A. S. Bastos, C. I. Justino, J. P. da Costa, A. C. Duarte, and T. A. Rocha-Santos, "Microplastics in the environment: Challenges in analytical chemistry-A review", Analytica Chimica Acta **1017**, 1 (2018).

[26] European Commission, "European Green Deal: Commission aims for zero pollution in air, water and soil", published online, accessed: 26.02.2025, `https://ec.europa.eu/commission/presscorner/detail/en/ip_21_2345` (2021).

[27] European Commission, "Commission regulation (eu) 2023/2055 of 25 September 2023 amending Annex xvii to Regulation (ec) No 1907/2006 of the European Parliament and of the Council concerning the Registration, Evaluation, Authorisation and Restriction of Chemicals (reach) as regards synthetic polymer microparticles", Official Journal of the European Union (2023).

[28] V. Hidalgo-Ruz, L. Gutow, R. C. Thompson, and M. Thiel, "Microplastics in the marine environment: a review of the methods used for identification and quantification", Environmental Science & Technology **46**, 3060 (2012).

[29] A. Käppler, D. Fischer, S. Oberbeckmann, G. Schernewski, M. Labrenz, K.-J. Eichhorn, and B. Voit, "Analysis of environmental microplastics by vibrational microspectroscopy: FTIR, Raman or both?", Analytical and Bioanalytical Chemistry **408**, 8377 (2016).

[30] Y. K. Müller, T. Wernicke, M. Pittroff, C. S. Witzig, F. R. Storck, J. Klinger, and N. Zumbülte, "Microplastic analysis—are we measuring the same? Results on the first global comparative study for microplastic analysis in a water sample", Analytical and Bioanalytical Chemistry **412**, 555 (2020).

[31] E. Ploetz, S. Laimgruber, S. Berner, W. Zinth, and P. Gilch, "Femtosecond stimulated Raman microscopy", Applied Physics B-Lasers and Optics **87**, 389 (2007).

[32] International Organization for Standardization, "ISO 24187: principles for the analysis of microplastics present in the environment", (Sept. 2023) `https://www.iso.org/obp/ui/#iso:std:iso:24187:ed-1:v1:en`.

[33] E. E. Burns and A. B. Boxall, “Microplastics in the aquatic environment: Evidence for or against adverse impacts and major knowledge gaps”, Journal of Environmental Toxicology and Chemistry **37**, 2776 (2018).

[34] P. Wu, J. Huang, Y. Zheng, Y. Yang, Y. Zhang, F. He, H. Chen, G. Quan, J. Yan, T. Li, and B. Gao, “Environmental occurrences, fate, and impacts of microplastics”, Ecotoxicology and Environmental Safety **184**, 109612 (2019).

[35] L. An, Q. Liu, Y. Deng, W. Wu, Y. Gao, and W. Ling, “Sources of Microplastic in the Environment”, in *Microplastics in terrestrial environments: emerging contaminants and major challenges*, edited by D. He and Y. Luo (Springer International Publishing, Cham, 2020), pp. 143–159.

[36] N. P. Ivleva, A. C. Wiesheu, and R. Niessner, “Microplastic in aquatic ecosystems”, Angewandte Chemie International Edition **56**, 1720 (2017).

[37] J. Boucher and D. Friot, “Primary microplastics in the oceans: a global evaluation of sources”, **10** (2017).

[38] C. Lorenz, L. Roscher, M. S. Meyer, L. Hildebrandt, J. Prume, M. G. Löder, S. Primpke, and G. Gerdts, “Spatial distribution of microplastics in sediments and surface waters of the southern North Sea”, Environmental Pollution **252**, 1719 (2019).

[39] B. He, M. Smith, P. Egodawatta, G. A. Ayoko, L. Rintoul, and A. Goonetilleke, “Dispersal and transport of microplastics in river sediments”, Environmental Pollution **279**, 116884 (2021).

[40] Textile Exchange, “Materials Market Report 2023”, published online, accessed: 19.08.2024, `https://textileexchange.org/app/uploads/2023/11/Materials-Market-Report-2023.pdf` (2023).

[41] C. M. Rochman, “Microplastics research—from sink to source”, Science **360**, 28 (2018).

[42] M. Eriksen, L. C. M. Lebreton, H. S. Carson, M. Thiel, C. J. Moore, J. C. Borerro, F. Galgani, P. G. Ryan, and J. Reisser, “Plastic Pollution in the World’s Oceans: More than 5 Trillion Plastic Pieces Weighing over 250,000 Tons Afloat at Sea”, PLOS One **9**, e111913 (2014).

[43] H. K. Imhof, N. P. Ivleva, J. Schmid, R. Niessner, and C. Laforsch, “Contamination of beach sediments of a subalpine lake with microplastic particles”, Current Biology **23**, R867 (2013).

[44] J. Dusaucy, D. Gateuille, Y. Perrette, and E. Naffrechoux, "Microplastic pollution of worldwide lakes", Environmental Pollution **284**, 117075 (2021).

[45] L. C. M. Lebreton, J. van der Zwet, J.-W. Damsteeg, B. Slat, A. Andrady, and J. Reisser, "River plastic emissions to the world's oceans", Nature Communications **8** (2017).

[46] T. Mani, A. Hauk, U. Walter, and P. Burkhardt-Holm, "Microplastics profile along the Rhine River", Scientific Reports **5** (2015).

[47] S. A. Carr, J. Liu, and A. G. Tesoro, "Transport and fate of microplastic particles in wastewater treatment plants", Water Research **91**, 174 (2016).

[48] K. A. V. Zubris and B. K. Richards, "Synthetic fibers as an indicator of land application of sludge", Environmental Pollution **138**, 201 (2005).

[49] S. Sridharan, M. Kumar, L. Singh, N. S. Bolan, and M. Saha, "Microplastics as an emerging source of particulate air pollution: A critical review", Journal of Hazardous Materials **418**, 126245 (2021).

[50] J. Brahney, M. Hallerud, E. Heim, M. Hahnenberger, and S. Sukumaran, "Plastic rain in protected areas of the United States", Science **368**, 1257 (2020).

[51] M. Klein and E. K. Fischer, "Microplastic abundance in atmospheric deposition within the Metropolitan area of Hamburg, Germany", Science of The Total Environment **685**, 96 (2019).

[52] F. Büks and M. Kaupenjohann, "Global concentrations of microplastics in soils – a review", SOIL **6**, 649 (2020).

[53] H. Ya, B. Jiang, Y. Xing, T. Zhang, M. Lv, and X. Wang, "Recent advances on ecological effects of microplastics on soil environment", Science of The Total Environment **798**, 149338 (2021).

[54] G. Dierkes, T. Lauschke, S. Becher, H. Schumacher, C. Földi, and T. Ternes, "Quantification of microplastics in environmental samples via pressurized liquid extraction and pyrolysis-gas chromatography", Analytical and Bioanalytical Chemistry **411**, 6959 (2019).

[55] G. Oliveri Conti, M. Ferrante, M. Banni, C. Favara, I. Nicolosi, A. Cristaldi, M. Fiore, and P. Zuccarello, "Micro- and nano-plastics in edible fruit and vegetables. The first diet risks assessment for the general population", Environmental Research **187**, 109677 (2020).

[56] G. Liebezeit and E. Liebezeit, "Non-pollen particulates in honey and sugar", Food Additives & Contaminants: Part A **30**, 2136 (2013).

[57] D. Yang, H. Shi, L. Li, J. Li, K. Jabeen, and P. Kolandhasamy, "Microplastic Pollution in Table Salts from China", Environmental Science & Technology **49**, 13622 (2015).

[58] B. De Witte, L. Devriese, K. Bekaert, S. Hoffman, G. Vandermeersch, K. Cooreman, and J. Robbens, "Quality assessment of the blue mussel (Mytilus edulis): Comparison between commercial and wild types", Marine Pollution Bulletin **85**, 146 (2014).

[59] A. Karami, A. Golieskardi, C. K. Choo, N. Romano, Y. B. Ho, and B. Salamatinia, "A high-performance protocol for extraction of microplastics in fish", Science of The Total Environment **578**, 485 (2017).

[60] L. I. Devriese, M. D. van der Meulen, T. Maes, K. Bekaert, I. Paul-Pont, L. Frère, J. Robbens, and A. D. Vethaak, "Microplastic contamination in brown shrimp (Crangon crangon, Linnaeus 1758) from coastal waters of the Southern North Sea and Channel area", Marine Pollution Bulletin **98**, 179 (2015).

[61] K. D. Cox, G. A. Covernton, H. L. Davies, J. F. Dower, F. Juanes, and S. E. Dudas, "Human Consumption of Microplastics", Environmental Science & Technology **53**, 7068 (2019).

[62] G. Suaria, A. Achtypi, V. Perold, J. R. Lee, A. Pierucci, T. G. Bornman, S. Aliani, and P. G. Ryan, "Microfibers in oceanic surface waters: A global characterization", Science Advances **6** (2020).

[63] L. Genchi, C. Martin, S. P. Laptenok, F. Baalkhuyur, C. M. Duarte, and C. Liberale, "When microplastics are not plastic: Chemical characterization of environmental microfibers using stimulated Raman microspectroscopy", Science of The Total Environment **892**, 164671 (2023).

[64] A. C. Wiesheu, P. M. Anger, T. Baumann, R. Niessner, and N. P. Ivleva, "Raman microspectroscopic analysis of fibers in beverages", Analytical Methods **8**, 5722 (2016).

[65] E. L. Teuten, J. M. Saquing, D. R. U. Knappe, M. A. Barlaz, S. Jonsson, A. Björn, S. J. Rowland, R. C. Thompson, T. S. Galloway, R. Yamashita, D. Ochi, Y. Watanuki, C. Moore, P. H. Viet, T. S. Tana, M. Prudente, R. Boonyatumanond, M. P. Zakaria, K. Akkhavong, Y. Ogata, H. Hirai, S. Iwasa, K. Mizukawa, Y. Hagino, A. Imamura, M. Saha, and H. Takada, "Transport and release of chemicals from plastics to the environment and to wildlife", Philosophical Transactions of the Royal Society B: Biological Sciences **364**, 2027 (2009).

[66] C. M. Boerger, G. L. Lattin, S. L. Moore, and C. J. Moore, "Plastic ingestion by planktivorous fishes in the North Pacific Central Gyre", Marine Pollution Bulletin **60**, 2275 (2010).

[67] E. Besseling, E. Foekema, J. Van Franeker, M. Leopold, S. Kühn, E. Bravo Rebolledo, E. Heße, L. Mielke, J. IJzer, P. Kamminga, and A. Koelmans, "Microplastic in a macro filter feeder: Humpback whale Megaptera novaeangliae", Marine Pollution Bulletin **95**, 248 (2015).

[68] M. D. Robards, J. F. Piatt, and K. D. Wohl, "Increasing frequency of plastic particles ingested by seabirds in the subarctic North Pacific", Marine Pollution Bulletin **30**, 151 (1995).

[69] S. L. Wright and F. J. Kelly, "Plastic and Human Health: A Micro Issue?", Environmental Science & Technology **51**, 6634 (2017).

[70] European Commission, "Commission Regulation (eu) 2024/3190 of 19 December 2024 on the use of bisphenol A (bpa) and other bisphenols and bisphenol derivatives with harmonised classification for specific hazardous properties in certain materials and articles intended to come into contact with food, amending Regulation (eu) No 10/2011 and repealing Regulation (eu) 2018/213", Official Journal of the European Union (2024).

[71] Z. Tian, H. Zhao, K. T. Peter, M. Gonzalez, J. Wetzel, C. Wu, X. Hu, J. Prat, E. Mudrock, R. Hettinger, A. E. Cortina, R. G. Biswas, F. V. C. Kock, R. Soong, A. Jenne, B. Du, F. Hou, H. He, R. Lundeen, A. Gilbreath, R. Sutton, N. L. Scholz, J. W. Davis, M. C. Dodd, A. Simpson, J. K. McIntyre, and E. P. Kolodziej, "A ubiquitous tire rubber–derived chemical induces acute mortality in coho salmon", Science **371**, 185 (2021).

[72] J. Wang, F. Wu, S. Dong, X. Wang, S. Ai, Z. Liu, and X. Wang, "Meta-analysis of the effects of microplastic on fish: Insights into growth, survival, reproduction, oxidative stress, and gut microbiota diversity", Water Research **267**, 122493 (2024).

[73] N. P. Ivleva, "Chemical Analysis of Microplastics and Nanoplastics: Challenges, Advanced Methods, and Perspectives", Chemical Reviews **121**, 11886 (2021).

[74] T. Horvatits, M. Tamminga, B. Liu, M. Sebode, A. Carambia, L. Fischer, K. Püschel, S. Huber, and E. K. Fischer, "Microplastics detected in cirrhotic liver tissue", eBioMedicine **82**, 104147 (2022).

[75] S. Massardo, D. Verzola, S. Alberti, C. Caboni, M. Santostefano, E. Eugenio Verrina, A. Angeletti, F. Lugani, G. M. Ghiggeri, M. Bruschi, G. Candiano, N. Rumeo, M. Gentile, P. Cravedi, S. La Maestra, G. Zaza, G. Stallone, P. Esposito, F. Viazzi, N. Mancianti, E. La Porta, and C. Artini, "Microraman spectroscopy detects the presence of microplastics in human urine and kidney tissue", Environment International **184**, 108444 (2024).

[76] L. Gaspar, S. Bartman, G. Coppotelli, and J. M. Ross, "Acute Exposure to Microplastics Induced Changes in Behavior and Inflammation in Young and Old Mice", International Journal of Molecular Sciences **24** (2023).

[77] H. Huang, J. Hou, M. Li, F. Wei, Y. Liao, and B. Xi, "Microplastics in the bloodstream can induce cerebral thrombosis by causing cell obstruction and lead to neurobehavioral abnormalities", Science Advances **11** (2025).

[78] G. Renner, T. C. Schmidt, and J. Schram, "Analytical methodologies for monitoring micro(nano)plastics: Which are fit for purpose?", Current Opinion in Environmental Science & Health **1**, 55 (2018).

[79] R. N. Thompson, C. A. Nau, and C. H. Lawrence, "Identification of Vehicle Tire Rubber in Roadway Dust", American Industrial Hygiene Association Journal **27**, 488 (1966).

[80] J. W. De Leeuw, E. W. B. De Leer, J. S. S. Damste, and P. J. W. Schuyl, "Screening of anthropogenic compounds in polluted sediments and soils by flash evaporation/pyrolysis gas chromatography-mass spectrometry", Analytical Chemistry **58**, 1852 (1986).

[81] Y. Lin, X. Huang, Q. Liu, Z. Lin, and G. Jiang, "Thermal fragmentation enhanced identification and quantification of polystyrene micro/nanoplastics in complex media", Talanta **208**, 120478 (2020).

[82] D. A. Cooper and P. L. Corcoran, "Effects of mechanical and chemical processes on the degradation of plastic beach debris on the island of Kauai, Hawaii", Marine Pollution Bulletin **60**, 650 (2010).

[83] S. Dehghani, F. Moore, and R. Akhbarizadeh, "Microplastic pollution in deposited urban dust, Tehran metropolis, Iran", Environmental Science and Pollution Research **24**, 20360 (2017).

[84] S. Primpke, S. H. Christiansen, W. Cowger, H. De Frond, A. Deshpande, M. Fischer, E. B. Holland, M. Meyns, B. A. O'Donnell, B. E. Ossmann, M. Pittroff, G. Sarau, B. M. Scholz-Böttcher, and K. J. Wiggin, "Critical Assessment of Analytical Methods for the Harmonized and Cost-Efficient Analysis of Microplastics", Applied Spectroscopy **74**, 1012 (2020).

[85] R. Lenz, K. Enders, C. A. Stedmon, D. M. Mackenzie, and T. G. Nielsen, "A critical assessment of visual identification of marine microplastic using Raman spectroscopy for analysis improvement", Marine Pollution Bulletin **100**, 82 (2015).

[86] J. D. Rodriguez, B. J. Westenberger, L. F. Buhse, and J. F. Kauffman, "Quantitative Evaluation of the Sensitivity of Library-Based Raman Spectral Correlation Methods", Analytical Chemistry **83**, 4061 (2011).

[87] A. Käppler, F. Windrich, M. G. Löder, M. Malanin, D. Fischer, M. Labrenz, K.-J. Eichhorn, and B. Voit, "Identification of microplastics by FTIR and Raman microscopy: a novel silicon filter substrate opens the important spectral range below 1300 cm1 for FTIR transmission measurements", Analytical and Bioanalytical Chemistry **407**, 6791 (2016).

[88] M. Bertasa, E. Possenti, A. Botteon, C. Conti, A. Sansonetti, R. Fontana, J. Striova, and D. Sali, "Close to the diffraction limit in high resolution ATR FTIR mapping: demonstration on micrometric multi-layered art systems", The Analyst **142**, 4801 (2017).

[89] C. F. Araujo, M. M. Nolasco, A. M. Ribeiro, and P. J. Ribeiro-Claro, "Identification of microplastics using Raman spectroscopy: latest developments and future prospects", Water Research **142**, 426 (2018).

[90] Z. Li, M. J. Deen, S. Kumar, and P. R. Selvaganapathy, "Raman Spectroscopy for In-Line Water Quality Monitoring—Instrumentation and Potential", Sensors **14**, 17275 (2014).

[91] A. Karami, A. Golieskardi, C. Keong Choo, V. Larat, T. S. Galloway, and B. Salamatinia, "The presence of microplastics in commercial salts from different countries", Scientific Reports **7** (2017).

[92] P. M. Anger, E. von der Esch, T. Baumann, M. Elsner, R. Niessner, and N. P. Ivleva, "Raman microspectroscopy as a tool for microplastic particle analysis", TrAC Trends in Analytical Chemistry **109**, 214 (2018).

[93] X. Gao, X. Li, and W. Min, "Absolute Stimulated Raman Cross Sections of Molecules", The Journal of Physical Chemistry Letters **14**, 5701 (2023).

[94] D. Li, Y. Shi, L. Yang, L. Xiao, D. K. Kehoe, Y. K. Gun'ko, J. J. Boland, and J. J. Wang, "Microplastic release from the degradation of polypropylene feeding bottles during infant formula preparation", Nature Food **1**, 746 (2020).

[95] L. Frère, I. Paul-Pont, J. Moreau, P. Soudant, C. Lambert, A. Huvet, and E. Rinnert, "A semi-automated Raman micro-spectroscopy method for morphological and chemical characterizations of microplastic litter", Marine Pollution Bulletin **113**, 461 (2016).

[96] M. D. Duncan, J. Reintjes, and T. J. Manuccia, "Scanning coherent anti-Stokes Raman microscope", Optics Letters **7**, 350 (1982).

[97] A. Zumbusch, G. R. Holtom, and X. S. Xie, "Three-Dimensional Vibrational Imaging by Coherent Anti-Stokes Raman Scattering", Physical Review Letters **82**, 4142 (1999).

[98] C. W. Freudiger, W. Min, B. G. Saar, S. Lu, G. R. Holtom, C. He, J. C. Tsai, J. X. Kang, and X. S. Xie, "Label-free biomedical imaging with high sensitivity by stimulated Raman scattering microscopy", Science **322**, 1857 (2008).

[99] H. Rigneault, J.-X. Cheng, W. Min, Y. Ozeki, and D. Polli, "Chapter 1 - Coherent Raman scattering processes", in *Stimulated raman scattering microscopy* (Elsevier, 2022), pp. 3–20.

[100] J.-X. Cheng, "Coherent Anti-Stokes Raman Scattering Microscopy", Applied Spectroscopy **61**, 197A (2007).

[101] M. Cole, P. Lindeque, E. Fileman, C. Halsband, R. Goodhead, J. Moger, and T. S. Galloway, "Microplastic ingestion by zooplankton", Environmental Science & Technology **47**, 6646 (2013).

[102] A. J. R. Watts, C. Lewis, R. M. Goodhead, S. J. Beckett, J. Moger, C. R. Tyler, and T. S. Galloway, "Uptake and Retention of Microplastics by the Shore Crab Carcinus maenas", Environmental Science & Technology **48**, 8823 (2014).

[103] A. J. R. Watts, M. A. Urbina, R. Goodhead, J. Moger, C. Lewis, and T. S. Galloway, "Effect of Microplastic on the Gills of the Shore Crab Carcinus maenas", Environmental Science & Technology **50**, 5364 (2016).

[104] D. S. Choi, S. Lim, J.-S. Park, C.-H. Kim, H. Rhee, and M. Cho, "Label-Free Live-Cell Imaging of Internalized Microplastics and Cytoplasmic Organelles with Multicolor cars Microscopy", Environmental Science & Technology **56**, 3045 (2022).

[105] C.-S. Liao, P. Wang, C. Y. Huang, P. Lin, G. Eakins, R. T. Bentley, R. Liang, and J.-X. Cheng, "In Vivo and in Situ Spectroscopic Imaging by a Handheld Stimulated Raman Scattering Microscope", ACS Photonics **5**, 947 (2017).

[106] C. Zhang, K.-C. Huang, B. Rajwa, J. Li, S. Yang, H. Lin, C. sheng Liao, G. Eakins, S. Kuang, V. Patsekin, J. P. Robinson, and J.-X. Cheng, "Stimulated Raman scattering flow cytometry for label-free single-particle analysis", Optica **4**, 103 (2017).

[107] L. Zada, H. A. Leslie, A. D. Vethaak, G. H. Tinnevelt, J. J. Jansen, J. F. de Boer, and F. Ariese, "Fast microplastics identification with stimulated Raman scattering microscopy", Journal of Raman Spectroscopy **49**, 1136 (2018).

[108] S. P. Laptenok, C. Martin, L. Genchi, C. M. Duarte, and C. Liberale, "Stimulated Raman microspectroscopy as a new method to classify microfibers from environmental samples", Environmental Pollution **267**, 115640 (2020).

[109] A. Smekal, "Zur Quantentheorie der Dispersion", Die Naturwissenschaften **11**, 873 (1923).

[110] C. V. Raman and K. S. Krishnan, "A New Type of Secondary Radiation", Nature **121**, 501 (1928).

[111] D. A. Long, "The Raman effect: A unified treatment of the theory of Raman scattering by molecules" (John Wiley Sons, Ltd, 2002).

[112] M. G. Albrecht and J. A. Creighton, "Anomalously intense Raman spectra of pyridine at a silver electrode", Journal of the American Chemical Society **99**, 5215 (1977).

[113] D. L. Jeanmaire and R. P. Van Duyne, "Surface raman spectroelectrochemistry: Part I. heterocyclic, aromatic, and aliphatic amines adsorbed on the anodized silver electrode", Journal of Electroanalytical Chemistry and Interfacial Electrochemistry **84**, 1 (1977).

[114] M. S. Anderson, "Locally enhanced Raman spectroscopy with an atomic force microscope", Applied Physics Letters **76**, 3130 (2000).

[115] N. Hayazawa, Y. Inouye, Z. Sekkat, and S. Kawata, "Metallized tip amplification of near-field Raman scattering", Optics Communications **183**, 333 (2000).

[116] R. M. Stöckle, Y. D. Suh, V. Deckert, and R. Zenobi, "Nanoscale chemical analysis by tip-enhanced Raman spectroscopy", Chemical Physics Letters **318**, 131 (2000).

[117] G. Eckhardt, R. W. Hellwarth, F. J. McClung, S. E. Schwarz, D. Weiner, and E. J. Woodbury, "Stimulated Raman Scattering From Organic Liquids", Physical Review Letters **9**, 455 (1962).

[118] R. W. Boyd, "Nonlinear optics", 3rd ed. (Academic Press, Amsterdam ; Boston, 2008), p. 635.

[119] D. W. McCamant, P. Kukura, and R. A. Mathies, "Femtosecond broadband stimulated Raman: A new approach for high-performance vibrational spectroscopy", Applied Spectroscopy **57**, 1317 (2003).

[120] P. Kukura, D. W. McCamant, and R. A. Mathies, "Femtosecond Stimulated Raman Spectroscopy", Annual Review of Physical Chemistry **58**, 461 (2007).

[121] C. Borbeck, F. van Riel Neto, R. Bernst, and P. Gilch, "Microfiber analysis via femtosecond stimulated Raman microscopy (FSRM)", Microplastics and Nanoplastics **5**, 14 (2025).

[122] M. Yoshizawa and M. Kurosawa, "Femtosecond time-resolved Raman spectroscopy using stimulated Raman scattering", Physical Review A **61**, 013808 (1999).

[123] Y. Li, B. Shen, S. Li, Y. Zhao, J. Qu, and L. Liu, "Review of Stimulated Raman Scattering Microscopy Techniques and Applications in the Biosciences", Advanced Biology **5**, 2000184 (2020).

[124] M. Lipkin, J. Nixdorf, and P. Gilch, "Optimized amplitude modulation in femtosecond stimulated Raman microscopy", Optics Letters **45**, 4204 (2020).

[125] W. Min and X. Gao, "Raman scattering and vacuum fluctuation: An Einstein-coefficient-like equation for Raman cross sections", The Journal of Chemical Physics **159**, 194103 (2023).

[126] B. Marx, "Eine MHz-Lichtquelle für die Femtosekunden-Stimulierte Raman-Mikroskopie", Inaugural dissertation, Mathematisch-Naturwissenschaftliche Fakultät, HHU Düsseldorf (2013).

[127] D. Meschede, "Optics, light and lasers : the practical approach to modern aspects of photonics and laser physics" (Wiley-VCH, 2004).

[128] Thorlabs, "GE photodiode FDG03 - specifications sheet", published online, `https://thin01mstroc282prod.dxcloud.episerver.net/globalassets/items/f/fd/fdg/fdg03-cal/13846-s01.pdf?v=0116113131?v=2026-01-16-11-31-31` (2018).

[129] B. Schrader, W. Meier, and I. für Spektrochemie und Angewandte Spektroskopie, "Raman/IR Atlas organischer Verbindungen: Raman/IR atlas of organic compounds", Teil 1 (Verlag Chemie, 1974).

[130] F. Munhoz, S. Brustlein, R. Hostein, P. Berto, S. Brasselet, and H. Rigneault, "Polarization resolved stimulated raman scattering: probing depolarization ratios of liquids", Journal of Raman Spectroscopy **43**, 419 (2011).

[131] L. Czerwinski, J. Nixdorf, G. Di Florio, and P. Gilch, "Broadband stimulated Raman microscopy with 0.1 ms pixel acquisition time", Optics Letters **41**, 3021 (2016).

[132] J. Nixdorf, "Charakterisierung von Polymeren mittels Femtosekunden-stimulierter Raman-Mikroskopie", Mathematisch-Naturwissenschaftliche Fakultät, HHU Düsseldorf (2019).

[133] R. C. Prince, R. R. Frontiera, and E. O. Potma, "Stimulated Raman scattering: from bulk to nano", Chemical Reviews **117**, 5070 (2017).

[134] L. Fuxen, "Raman-Mikroskopie an Mikroplastik in Kosmetik-Produkten", Bachelor's thesis, Mathematisch-Naturwissenschaftliche Fakultät, HHU Düsseldorf (2022).

[135] A. Bottone, J. Boily, A. Shchukarev, P. L. Andersson, and J. Klaminder, "Sodium hypochlorite as an oxidizing agent for removal of soil organic matter before microplastics analyses", Journal of Environmental Quality **51**, 112 (2021).

[136] R. Palanisamy, V. Rengarajan, G. Sozhen, and K. Narasimham, "Electrolytic production of sodium hypochlorite for bleaching", Indian Pulp & Paper Technical Association **5**, 45 (1993).

[137] J. C. Bezdek, R. Ehrlich, and W. Full, "FCM: the fuzzy c-means clustering algorithm", Computers & Geosciences **10**, 191 (1984).

[138] M. Hedegaard, C. Matthäus, S. Hassing, C. Krafft, M. Diem, and J. Popp, "Spectral unmixing and clustering algorithms for assessment of single cells by Raman microscopic imaging", Theoretical Chemistry Accounts **130**, 1249 (2011).

[139] K. Pearson, "On lines and planes of closest fit to systems of points in space", The London, Edinburgh, and Dublin Philosophical Magazine and Journal of Science **2**, 559 (1901).

[140] H. Hotelling, "Analysis of a complex of statistical variables into principal components.", Journal of Educational Psychology **24**, 417 (1933).

[141] S. Wold, K. Esbensen, and P. Geladi, "Principal component analysis", Chemometrics and Intelligent Laboratory Systems **2**, 37 (1987).

[142] R. Bro and A. K. Smilde, "Principal component analysis", Analytical Methods **6**, 2812 (2014).

[143] R. Xu and D. Wunsch, "Survey of Clustering Algorithms", IEEE Transactions on Neural Networks **16**, 645 (2005).

[144] J. MacQueen, "Some methods for classification and analysis of multivariate observations", in *Proc. Fifth Berkeley Sympos. Math. Statist. and Probability (Berkeley, Calif., 1965/66), Vol. I: Statistics* (Univ. California Press, Berkeley, CA, 1967), pp. 281–297.

[145] D. Xu and Y. Tian, "A Comprehensive Survey of Clustering Algorithms", Annals of Data Science **2**, 165 (2015).

[146] S. Ghosh and S. Kumar, "Comparative Analysis of K-Means and Fuzzy C-Means Algorithms", International Journal of Advanced Computer Science and Applications **4**, 35 (2013).

[147] L. Zadeh, "Fuzzy sets", Information and Control **8**, 338 (1965).

[148] A. Büchter, "Elementare Stochastik: Eine Einführung in die Mathematik der Daten und des Zufalls", Mathematik für das Lehramt (Springer, Berlin u.a., 2005).

[149] K. Watanabe, A. F. Palonpon, N. I. Smith, L.-d. Chiu, A. Kasai, H. Hashimoto, S. Kawata, and K. Fujita, "Structured line illumination Raman microscopy", Nature Communications **6**, 10095 (2015).

[150] K. Tabata, H. Kawagoe, J. N. Taylor, K. Mochizuki, T. Kubo, J.-E. Clement, Y. Kumamoto, Y. Harada, A. Nakamura, K. Fujita, and T. Komatsuzaki, "On-the-fly Raman microscopy guaranteeing the accuracy of discrimination", Proceedings of the National Academy of Sciences **121**, e2304866121 (2024).

[151] J. Nixdorf, G. Di Florio, L. Brockers, C. Borbeck, H. E. Hermes, S. U. Egelhaaf, and P. Gilch, "Uptake of methanol by poly (methyl methacrylate): an old problem addressed by a novel Raman technique", Macromolecules **52**, 4997 (2019).

[152] D. Bertoldo Menezes, A. Reyer, A. Benisek, E. Dachs, C. Pruner, and M. Musso, "Raman spectroscopic insights into the glass transition of poly(methyl methacrylate)", Physical Chemistry Chemical Physics **23**, 1649 (2021).

[153] J. C. Deàk, L. K. Iwaki, and D. D. Dlott, "Vibrational Energy Redistribution in Polyatomic Liquids: Ultrafast IR-Raman spectroscopy of acetonitrile", The Journal of Physical Chemistry A **102**, 8193 (1998).

[154] D. Li, N. Zhai, S. Xu, M. Zhang, C. Sun, and H. Li, "Study the effect of Li+ on the ν2/ν3+ν4 Fermi resonance of acetonitrile by Raman Spectroscopy", Spectrochimica Acta Part A: Molecular and Biomolecular Spectroscopy **206**, 314 (2019).

[155] J. Green, "Vibrational spectra of benzene derivatives—ii", Spectrochimica Acta **17**, 607 (1961).

[156] H. F. Hameka and J. O. Jensen, "Theoretical studies of the methyl rotational barrier in toluene", Journal of Molecular Structure: THEOCHEM **362**, 325 (1996).

[157] E. L. Hommel and H. C. Allen, "The air–liquid interface of benzene, toluene, m-xylene, and mesitylene: a sum frequency, Raman, and infrared spectroscopic study", The Analyst **128**, 750 (2003).

[158] J. F. Mammone, S. K. Sharma, and M. Nicol, "Raman spectra of methanol and ethanol at pressures up to 100 kbar", The Journal of Physical Chemistry **84**, 3130 (1980).

[159] S. Yoon, D. W. McCamant, P. Kukura, R. A. Mathies, D. Zhang, and S.-Y. Lee, "Dependence of line shapes in femtosecond broadband stimulated Raman spectroscopy on pump-probe time delay", The Journal of Chemical Physics **122**, 024505 (2004).

[160] W. Konijnendijk and J. Stevels, "The structure of borosilicate glasses studied by Raman scattering", Journal of Non-Crystalline Solids **20**, 193 (1976).

[161] S. Lim, B. Chon, H. Rhee, and M. Cho, "Spectral modulation of stimulated Raman scattering signal: Beyond weak Raman pump limit", Journal of Raman Spectroscopy **49**, 607 (2018).

[162] T. Würthwein, N. M. Lüpken, N. Irwin, and C. Fallnich, "Mitigating cross-phase modulation artifacts in femtosecond stimulated Raman scattering", Journal of Raman Spectroscopy **51**, 2265 (2020).

[163] P. P. Ho and R. R. Alfano, "Optical Kerr effect in liquids", Physical Review A **20**, 2170 (1979).

[164] P. Berto, E. R. Andresen, and H. Rigneault, "Background-Free Stimulated Raman Spectroscopy and Microscopy", Physical Review Letters **112**, 053905 (2014).

[165] F. Crisafi, V. Kumar, T. Scopigno, M. Marangoni, G. Cerullo, and D. Polli, "In-line balanced detection stimulated Raman scattering microscopy", Scientific Reports **7**, 10745 (2017).

[166] J. van der Kolk, A. C. Lesina, and L. Ramunno, "Effects of refractive index mismatch on SRS and CARS microscopy", Optics Express **24**, 25752 (2016).

[167] D. M. Carey and G. M. Korenowski, "Measurement of the Raman spectrum of liquid water", The Journal of Chemical Physics **108**, 2669 (1998).

[168] L.-L. Cho, "Identification of textile fiber by Raman microspectroscopy", Forensic Science Journal **6**, 55 (2007).

[169] D. Puchowicz and M. Cieslak, "Raman Spectroscopy in the Analysis of Textile Structures", edited by C. S. Pathak and S. Kumar, Recent Developments in Atomic Force Microscopy and Raman Spectroscopy for Materials Characterization (IntechOpen, 2022), p. 157.

[170] N. K. Howell, G. Arteaga, S. Nakai, and E. C. Li-Chan, "Raman spectral analysis in the C H stretching region of proteins and amino acids for investigation of hydrophobic interactions", Journal of Agricultural and Food Chemistry **47**, 924 (1999).

[171] E. Rebollar, S. Pérez, M. Hernández, C. Domingo, M. Martín, T. A. Ezquerra, J. P. García-Ruiz, and M. Castillejo, "Physicochemical modifications accompanying UV laser induced surface structures on poly (ethylene terephthalate) and their effect on adhesion of mesenchymal cells", Physical Chemistry Chemical Physics **16**, 17551 (2014).

[172] L. Song and H. Huang, "Fixed Pattern Noise Removal Based on a Semi-Calibration Method", IEEE Transactions on Pattern Analysis and Machine Intelligence **45**, 11842 (2023).

[173] A. M. Elert, R. Becker, E. Duemichen, P. Eisentraut, J. Falkenhagen, H. Sturm, and U. Braun, "Comparison of different methods for MP detection: what can we learn from them, and why asking the right question before measurements matters?", Environmental Pollution **231**, 1256 (2017).

[174] S. Huppertsberg and T. P. Knepper, "Instrumental analysis of microplastics—benefits and challenges", Analytical and Bioanalytical Chemistry **410**, 6343 (2018).

[175] R. Bernst, "Optimized Signal Acquisition in FSRM", Master's thesis, Mathematisch-Naturwissenschaftliche Fakultät, HHU Düsseldorf (2025).

[176] S. Wu, Y. Zhang, C. He, Z. Luo, Z. Chen, and J. Ye, “Self-Supervised Learning for Generic Raman Spectrum Denoising”, Analytical Chemistry **96**, 17476 (2024).

List of Figures

Index of Abbreviations

ABS	acrylonitrile butadiene styrene
AOM	acousto-optic modulator
ATR	attenuated total reflection
BPA	bisphenol A
CARS	coherent anti-Stokes Raman scattering
cw	continuous wave
EDX	energy dispersive X-ray spectroscopy
FCM	fuzz c-means
FSRM	femtosecond stimulated Raman microscopy
FSRS	femtosecond Raman spectroscopy
FT	Fourier transform
FWHM	full width at half maximum
GC/MS	Gas chromatography–mass spectrometry
HDPE	high-density polyethylene
HQI	hit quality index
ICP-MS	inductively coupled plasma mass spectrometry
IR	Infrared
LDPE	low-density polyethylene
LLDPE	linear low-density polyethylene
MALDI-ToF	matrix-assisted laser desorption/ionization time-of-flight mass spectrometry
MDPE	medium-density polyethylene
MP	microplastic

ND	neutral density
PAH	polycyclic aromatic hydrocarbons
PC	principal component
PCA	principal component analysis
PCB	polychlorinated biphenyl
PE	polyethylene
PET	poly(ethylene terephthalate)
PMMA	poly(methyl methacrylate)
POPs	persistent organic pollutants
PP	Polypropylene
PS	polystyrene
PUR	polyurethane
PVC	polyvinyl chloride
Py	pyrolysis
ROI	region of interest
SEM	scanning electron microscopy
SERS	surface-enhanced Raman spectroscopy
SNR	signal-to-noise ratio
SRG	stimulated Raman gain
SRL	stimulated Raman loss
SRS	stimulated Raman scattering/spectroscopy
TERS	tip-enhanced Raman spectroscopy
Ti:Sa	titanium:sapphire
WDM	wavelength division multiplexer

WWTP	waste water treatment plant
XPM	cross-phase modulation

Respective Contributions

Some parts of this work have already been published. This concerns the measurements and FCM analysis of microfibers in Section 6.2.3, which were described in ref. [121]. I am the first author of this publication. The experiments were planned and conducted by me. The samples were prepared under my guidance and supervision by Roman Bernst as part of his bachelor thesis. The FCM evaluations of the measurements as published in ref. [121], which were adapted in this work, were planned and coordinated by me and carried out by Roman Bernst with my consultation. The manuscript was written by me, corrected by Peter Gilch, and proofread by the other authors, Francisco van Riel Neto and Roman Bernst. All illustrations were composed by me.

Mixtures of polymer Standards (PMMA and PS) and of a facial scrub particle in Clearasil were prepared for measurement under my supervision by Leonard Röhrken as part of his bachelor thesis. The measurements and evaluations were conducted by me. The illustrations shown here were composed by me.

Declaration of Authorship

I hereby declare that I have authored the thesis entitled

"Microplastics analyzed by Femtosecond Stimulated Raman Microscopy (FSRM)"

No other person's work has been used without due acknowledgement in this thesis. Where I have quoted from or adapted the work of others, the source is always given. This includes the sources of graphs and data.

Düsseldorf, Friday 20th March, 2026

Place, Date	Carolin Borbeck